Rept no R77-922578-13 ✓

①

Laser Propagation Experiments - Aerosol and Stagnation Zone Effects

Final Technical Report

June 19, 1977

M.C. Fowler
J.R. Dunphy
D.C. Smith

533,052
①

For Period Covering
October 19, 1976 to April 19, 1977

Sponsored by
Advanced Research Projects Agency
ARPA Order No. 2439
Contract No. N00173-76-C-0157 new

UNITED TECHNOLOGIES
RESEARCH CENTER
UNITED TECHNOLOGIES

EAST HARTFORD, CONNECTICUT 06108

77-08-214-1

UNITED TECHNOLOGIES RESEARCH CENTER

East Hartford, Connecticut 06108

14 UTRC/R77-922578-13

6

Laser Propagation Experiments
Aerosol and Stagnation Zone Effects.

D D C
JAN 6 1978
F

11 Final technical rept. 19 Oct 76-19 Apr 77,

10 M. C. Fowler J. R. Dunphy, David C. Smith

APPROVED FOR PUBLIC RELEASE
DISTRIBUTION UNLIMITED

15 N00173-76-C-0157, ARPA Order-2439

11

DATE Aug[redacted] [redacted]77

NO. OF PAGES ______ 12 117p.

COPY NO. ______

409 528

R77-922578-13

Laser Propagation Experiments

Aerosol and Stagnation Zone Effects

TABLE OF CONTENTS - SECTION A

FIGURES

TABLE OF CONTENTS - SECTION B

AEROSOL EFFECTS ON CO_2 LASER PROPAGATION

Page No.

R77-922578-13

Laser Propagation Experiments - Aerosol and Stagnation Zone Effects

ARPA Order No.:	2439
Program Code:	6E20
Contractor:	United Technologies Research Center
Effective Date of Contract	April 19, 1976
Contract Expiration Date:	June 19, 1977
Amount of Contract:	$200,000
Contract Number:	N00173-76-C-0157
Principal Investigator:	Dr. David C. Smith
Scientific Officer:	Dr. P. B. Ulrich (Code 5565) 4555 Overlook Avenue, S.W. Washington, D. C. 20375
Short Title:	Laser Propagation Experiments

SUMMARY

This final technical report describes the result of two programs concerned with high power laser propagation through the atmosphere that are particularly important to the Navy high energy laser program. The first study deals with an experimental laboratory simulation of moving stagnation zones a problem which can be quite serious for the Navy application. The second study is the propagation and non-linear interaction of a high intensity laser with water droplets or fog, again in a laboratory simulation experiment under realistic conditions. The experimental results are given in terms of non-dimensional parameters which can be interpreted in terms of real outside atmospheric conditions. In addition, the results are modeled by simplified analytic expressions which should find wide use in systems analysis of Navy scenarios.

The stagnation zone, a region of the propagation path with no net motion between the laser beam and the air can occur in a number of Navy scenarios. It is particularly serious because in such a region the absorption of laser beam energy causes more severe heating and thus stronger thermal blooming than would result if there were relative motion. Under Navy sponsorship in a program preceding this one, we studied the problem of a fixed stagnation zone, because of its simplicity and experimental tractability. We determined that the initial distortion increased in severity but that the distortion (and thus intensity on target) reached a quasi-steady state value. An analytic model was found which predicted quite accurately the experimental results. In more realistic situations, the stagnation zone is not stationary but has an axial motion, due normally to changes in the laser beam slew rate. The motion of the stagnation zone can influence the thermal distortion and the influence of stagnation zone motion is the subject of the present contract. Details of the experiment and analytic modeling are contained in Section A. Basically what we found was, under realistic conditions, the thermal distortion caused by a moving stagnation zone followed the quasi-steady state distortion. Thus the transient behavior of the intensity on target is described by the steady state solutions of the stationery zones which is modeled analytically. Thus the potentially complicated problem is reduced to a more simple form which can be handled analytically. One other aspect of this problem remains to be investigated and this is the effect of a noncoplanar engagement geometry where the problem is no longer confined to a two dimensional phase but includes a second component of slew due to a difference in altitude between the target and the laser source.

The second area of this final report discusses the results of the experimental program to examine the interaction of high intensity laser radiation with fog with particular emphasis on the non-linear thermal blooming of the laser beam caused by the water droplet absorption. The program was primarily experimental, utilizing an 8 kW CW CO_2 laser, a 10 meter long cell, seeded with micron size water drops, and associated diagnostic equipment.

At intensities of a kW/cm^2 and scaled Navy scenario conditions, it was found that the laser interaction led to vaporization of the droplets. This vaporization had two positive effects. 1) it reduced the linear loss of laser beam energy due to partial elimination of the fog and 2) the thermal distortion is significantly less than that predicted by the unperturbed conditions. (Previous to this study thermal blooming predictions were based only on initial conditions). The contribution of hydrosol absorption to thermal blooming was modeled by an analytic expression where the vaporization of particules acted as a saturable absorber. Insufficient data was obtained under the present funding to verify all aspects of the hydrosol induced blooming. The details of the experimental procedure and results are contained in Section B of this report.

CW THERMAL BLOOMING IN A MOVING STAGNATION ZONE

SECTION AI

INTRODUCTION

This report describes an experimental investigation of thermal blooming occuring in stagnation zones, volumes of medium in which there occurs no net flow transverse to the laser axis, which move axially between the target and the laser. The study focusses first on the expansion of the data base for laser beam intensity degradation by stationary stagnation zones over a range of beam focussing ratios and attenuation and then uses this data base for comparison with data taken with moving stagnation zones. This report is divided into five sections: Section II describes the apparatus and some of the experimental results, Section III reviews the theory used for understanding the effect of a stagnation zone on laser beam propagation and proposes a modification on the earlier form of this theory, Section IV presents the experimental results and Section V the conclusions, principally that thermal blooming in a stagnation zone, stationary or moving, is characterized by a single thermal blooming parameter with the temporal variation of the on-target intensity in the moving zone case being determined by the time dependence of this parameter.

SECTION AII

EXPERIMENTAL APPARATUS AND INSTRUMENTION

A. INTRODUCTION

The apparatus used in the experiments was described only in general terms in Ref. 1 and several of its properties are treated in more detail in this section.

B. APPARATUS KINEMATICS

The apparatus is shown schematically in Fig. A1. The absorption cell is mounted on a plate which is driven by an electric motor-gearbox assembly at speed $\dot{x}_o$. As shown, the top of the cell is free to rotate about the pivot point at its base and is coupled to a second motor-gearbox assembly which in turn is attached to the same plate on which the cell is mounted. This second motor drives the top of the cell at a time varying speed, $\dot{x}_\ell + \ddot{x}_\ell t$, in direction opposite to $\dot{x}_o$. The way in which $\dot{x}_\ell$ and $\ddot{x}_\ell$ are controlled is described in Ref. 1 as is the way in which the speed of the cell top is monitored. For the situation shown in Fig. 1, the position y_o of a stagnation zone center is given in terms of the cell length, ℓ by(1)

$$Y_0 = (-\dot{X}_0/\dot{X}_\ell)\ (1+\ddot{X}_\ell t/\dot{X}_\ell)^{-1}. \qquad \text{A-II-1}$$

C. LASER OPTICAL TRAIN

The optical train used for conditioning the laser beam in these experiments is now described in somewhat more detail than was done in Ref. 1. The laser used in these experiments was a water cooled electric discharge CO_2 laser approximately two meters long equipped with a 10 m radius of curvature totally reflecting end mirror and a 65 percent reflecting germanium flat decoupling mirror. Zinc selenide or sodium chloride flats at Brewster's angle were used intracavity to vacuum seal the laser discharge. To control the oscillation mode of the laser, an adjustable iris was positioned at the output window and the iris diameter was decreased to suppress oscillation at modes other than TEM_{oo}. Care had to be taken to avoid excessive closure of this iris as it was found that doing so apertured the gaussian shaped output intensity spatial distribution of the laser and resulted in Fresnel diffraction and spreading of the output. The largest output power used in the experiments performed was 30 watts. Losses in the optical train were found to increase slightly with time so that, for 30 watts laser output, 18 watts were typically incident on the absorption cell in experiments performed early in the study, with this power decreasing to 16 watts in the later experiments. An adjustable telescope, consisting of two germanium lenses of +6.8 cm and +13 cm focal length, was used to focus the laser output onto the detector. These lenses are shown in Fig. A1 to be in the "beam expander" sequence with the shorter focal length lens positioned first in the beam. With this configuration a value of about 4.5 could be attained for the degree of focus, F, defined as the ratio of beam diameter at the cell entrance to the diameter at the cell exit. With the lenses interchanged, the value of F attained was 1.2. The laser was turned on and off in these experiments by withdrawing and inserting a knife edge shutter at the beam waist in the telescope, the point were the beam diameter is the smallest in the entire optical train. The time elapsed in withdrawing the knife edge from the beam waist was determined by monitoring the laser power at the detector, with the pivoting mirror stationary, as a function of time while the knife edge was withdrawn. The turn-on time, defined as the time elapsed for the detected signal to reach a fraction equal to $(1-e^{-1})$ of its full value, was measured to be 0.8 msec when the telescope was in the beam expander mode. This "time" is of course determined by the speed of the knife edge and the diameter of the beam at the waist, the latter being equal to the product of the focal length of the first telescope lens and the laser beam divergence angle. Accordingly, the turn on time in the case where the longer focal length lens is the first telescope lens is seen to be 1.6 msec. It is important that the turn on time be small compared to the time characteristic for CW thermal blooming, defined as the time elapsed for the peak intensity at the detector to equal e^{-1} of its unperturbed value. For the most extreme experimental conditions encountered (16 W laser power, ten atmospheres CO_2, F = 4.8) the blooming time is calculated, from a formula given in the appendix, for the apparatus to be a 8.8 msec and therefore large compared to the turn on time so that the finite magnitude of the latter will not affect the experimental results. At the lower, F = 1.2, focussing ratio, the blooming time is 75 msec, and the same conclusion holds.

The focussing ratio, F, as will be seen, is of importance to the parameters which characterize thermal blooming severity. For a beam of gaussian spatial intensity distribution the beam radius is defined as the displacement from beam center at which the intensity is e^{-1} of its value at center, which in turn can be expressed in terms of the beam diameter, d* and the total beam power P by the ratio $P/(\pi/4 d^{*2})$. Alternately, the value of d* is the diameter within which a fraction equal to $(1-e^{-1})$ of P is contained. The value of F is calculated by first measuring the value of d* at the exit of the telescope and at the detector onto which the telescope focus the beam and using the relationship which expresses the dependence of d* at distances z from the detector:

$$d^*(z) = (d^*(0)^2 + z^2 d^*(L)^2 L^{-2})^{1/2}, \qquad \text{A-II-2}$$

where L, the distance from the detector to the telescope, is the focal length of the latter.

The quantity $d^*(L)$ is obtained by installing an adjustable iris at the output lens of the telescope and measuring $P(d)$, the power at the detector when the iris diameter is d. The relevant plot of this experimental data is $\ln(1-P(d)/P)$ vs d^2, and $d^*(L)$ is the value of d for which the ordinate has a value of minus one. One such plot is shown in Fig. A2 from which it is seen that the value of $d^*(L)$ is 1.1 cm.

The value of $d^*(0)$ is obtained using the pivoting mirror shown in Fig. A1 in conjunction with the detector, liquid Nitrogen cooled gold doped germanium equipped with a 0.02 cm pinhole aperture, which samples the beam intensity as it is swept across the latter by the mirror. The mirror is mounted in a general scanning G300PD motor driven by a Tektronix AF501 Band Pass Filter run as an oscillator. The beam turned by the mirror follows an oscillatory path and is sweeped across the detector aperture at a speed, $2\pi\nu\theta_m d$, determined by the displacement of the aperture from the mirror, d, the oscillator frequency, ν, and the maximum angular deflection of the mirror, θ_m. The detector output, terminated by a 10 kΩ resistor (resulting RC response time is 1 μsec) is amplified by a second AF501 Band Pass Filter and displayed on an oscilloscope. One such oscillogram is presented in Fig. A3. The value of $d^*(0)$ is given by the product of the sweep speed, 850 cm/sec, and the time interval for which the measured intensity exceeds e^{-1} of its maximum value. For the sweep shown in Fig. A3, the value of $d^*(0)$ is seen to be 0.095 cm, five times larger than the pinhole and which, when combined with $d^*(L)$ the positions of the entrance (124 cm) and exit (20 cm) windows in Eq. 2 (A-II-2) gives a value of 4.8 for the degree of focus.

D. GAS HANDLING

One of the quantities to which thermal blooming is sensitive is the product of the linear attenuation coefficient, α, and ℓ, the length of the range or, in laboratory experiments, the gas cell. Therefore, two different gas mixtures were employed in the present experiments. For $\alpha\ell$ values up to 0.2 a mixture of nitrogen and propylene was used while for a value of 0.45, pure CO_2 was used. For either mixture the total gas pressure was ten atmospheres absolute to minimize the role of conduction relative to convection in determining the thermal blooming properties in the experiment.(2)

E. DATA COLLECTION

In a stationary medium, the effect of thermal blooming is to spread the laser power symmetrically about the beam axis, but putting the medium in motion causes the spreading to be symmetric only about the plane passing through the beam axis and parallel to the medium velocity, with the maximum intensity in this plane not always coinciding with the unperturbed beam axis. Since the quantity of interest in the present study was the behavior of this maximum intensity, the data records consisted of sweeping the beam across the detector aperture in the plane described above at a frequency of 166 Hz and observing the variation of the maximum intensity in this plane with $\dot{x}_o$, $\dot{x}_\ell$ and $\ddot{x}_\ell$ for various combinations of F, $\alpha\ell$, and P.

Figure A4 presents the data records of two experimental runs. Each record consists of two traces. The top trace in each case is the laser detector output as a function of time. This output appears as a series of spikes, each of which represents a sweep of the beam across the detector face as described above. The bottom trace represents the output of a GE H13B1 Photon Coupled Interrupter Module, essentially a compact light source and detector, which measures the amount of light at a fixed point through the photograph of a grid of alternating zones of high and low opacity. This grid, as indicated in Fig. A1, is fixed to a point displaced 74 cm from the cell pivot so that x is determined by noting the elapsed time between two maxima in the bottom trace and combining this with the known distance, 0.055 cm between opacity minima on the film and the knowledge of the position of the film relative to the cell pivot. In Fig. A4a $\ddot{x}_\ell$ is observed to be zero and $\dot{x}_\ell$ has a value of 5.4 cm/sec. In contrast, the Fig. A4b indicates a value of 5.7 cm/sec for $\dot{x}_\ell$ and 27 cm/sec^2 for $\ddot{x}_\ell$. For both experiments $\dot{x}_o$ had a value of -4.0 cm/sec so that Fig. A4a represents thermal blooming in a stationary stagnation zone situated at 75 cm above the entrance window and in Fig. A4b the stagnation zone, situated initially 69 cm above the entrance, moves toward the entrance window as given by Eq. A-II-1. It is seen that the laser intensity for these two runs shows a different temporal development, becoming constant at a relatively low value in Fig. A4a but passing through a minimum and increasing markedly in Fig. A4b. The reasons for this temporal development will be discussed in later sections.

Generally, the quantity of interest for comparison with analytic models of thermal blooming is not the measured intensity but rather the intensity normalized by that which would be incident to the detector in the absence of thermal blooming or the intensity as indicated, for an empty cell, by the maximum in the trace in Fig. A3 corrected only for the linear attenuation due to molecular absorption, $e^{-\alpha\ell}$. When $\alpha\ell$ is small as in Fig. 4, the thermal blooming time is large enough and the intensity of the bloomed beam large enough to permit both the temporally varying intensity, I(t), and the normalizing intensity, I(0) to be read from the same oscillogram. For larger $\alpha\ell$ values it was found that I(0) was an elusive quantity to measure. One reason for this was that the thermal blooming time, on the order of 8.8 msec was comparable to the uncertainty in the zero time point in the oscillogram due to the fact that the oscilloscope was triggered by the first beam sweep across the detector which could lag behind the true beam turn-on at the knife wedge shutter by half the pivot mirror sweep period or 6 msec. In addition, for large $\alpha\ell$ the intensity of the bloomed beam was so small as to require additional amplification at the oscilloscope to facilitate its measurement in which case I(0) was off scale on the oscillogram. In this situation empty cell intensity traces such as that shown in Fig. A3 were taken as calibration points and I(0) was then the product of this intensity and $e^{-\alpha \ell}$ and could be rendered useful to normalizing the data on an oscillogram merely by multiplication by the additional amplification factor used in obtaining the oscillogram.

SECTION AIII

ANALYTICAL MODELS FOR THERMAL BLOOMING BY STAGNATION ZONES

A. INTRODUCTION

As past studies have shown (3), thermal blooming is a phenomenon which degrades laser propagation and is influenced by a number of factors which include beam power, P, the degree of focusing, F, the linear attenuation over the range $\alpha\ell$, and medium properties such as density, ρ, heat capacity, c_p, and refractive index temperature coefficient, μ_T. It has been found helpful to devise models for thermal blooming under the varying conditions of interest to derive thermal blooming parameters which include in a single quantity the properties listed above along with properties peculiar to the condition of interest.(3) For the stationary stagnation zone problem, this was done by Berger (2,5) who modeled the stagnation zone as a fixed thin thermal lens of constant properties which distorted the on-target intensity by shifting the focal point of the beam. In this section, a modified form of Berger's treatment is introduced to provide an alternate parameter for characterizing thermal blooming in the presence of a stagnation zone.

Berger's thin thermal lens, treatment strictly holds for stagnation zones only for those cases in which the properties and position of the lens are constant in time. In an attempt to obtain a treatment of stagnation zone thermal blooming which includes non-steady state effects, a second model, also has been developed and is described in Appendix AI.

B. STEADY STATE THIN THERMAL LENS MODEL OF STAGNATION ZONE THERMAL BLOOMING

As stated originally by Berger(4) the effect of a stagnation zone on laser beam propagation can be seen by considering a thin thermal lens of negative focal length to be positioned in the beam at the stagnation zone. The focal length of this lens is given in terms of the medium properties, the beam radius, $a(z')$, at z', the location of the stagnation zone in the range, the on-time of the laser, t, and the thickness of the lens, δz, a quantity to be dealt with further at a later point:

$$f = \pi \rho c_p a(z')^4/(\mu_T \alpha P t \,\partial z). \qquad \text{(A-III-1)}$$

The unperturbed laser beam, propagating in the z direction, is considered to have a radius a_o at its origin, to converge to a focus a distance R' beyond z', and the effect of the thin lens is to increase the distance to a value R_e whose magnitude is given by the thin lens law:

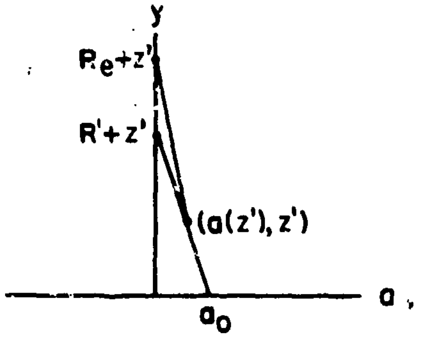

where $R_e = R'f/(R'+f)$.

Of interest is the intensity at a point z_f between z' and R'+z' where

$$I(z_f) = P/\pi a'(z_f)^2), \qquad \text{(A-III-2)}$$

and a'(z) denotes the z dependence of the perturbed beam radius:

$$a'(z) = a_0 (R'/R_e)(R_e + z' - z)/(R' + z'). \qquad \text{(A-III-3)}$$

The variation $I(z_f)$ with the position and properties of the lens is readily expressed by '

$$\frac{dI(z_f)}{I(z_f)} = \frac{-2}{a'(z_f)} \left[\left(\frac{\partial a(z_f)}{\partial R'} \right)_{z', R_e} dR' + \left(\frac{\partial a'(z_f)}{\partial z'} \right)_{R, R_e} dz' + \left(\frac{\partial a'(z_f)}{\partial R_e} \right)_{z', R} dR_e \right] \qquad \text{(A-III-4)}$$

where the first two terms in brackets relate to lens position while the third relates to lens properties. In principle, solution to the moving stagnation zone problem is given by the solution of Eq. (A-III-4). In practice it is convenient first to fix the position of the lens and consider the stationary stagnation zone problem. In this case, Eq. (A-III-4) is readily integrated to give

$$I_r = \frac{I(z_f,t)}{I(z_f,0)} \cong \left(1 - \frac{a(z')(z_f - z')}{a(z_f)^f}\right)^{-2}. \qquad \text{(A-III-5)}$$

At this point in his development, Berger(5) points out that there comes a time after which the increase in engergy, Pt, deposited at the stagnation zone to cause the lens' focal length to decrease is balanced by the decrease in δz due to convective cleanout of heated medium by motion of the latter normal to the beam axis at points other than the stagnation zone center. Once this steady state is reached, Berger postulates that δz is replaced by the quantity $4a(z')/w$, where w is both the angular velocity of the medium about the stagnation zone and also the slew rate of the target about the laser. Making use of the analysis of the apparatus in Ref. 1 and including the factor $e^{-\alpha z'}$ which accounts for the attenuation of the laser beam power in the path preceding the stagnation zone, Eq. A-III-5 can be written in terms of the apparatus parameters:

$$I_{rss} \equiv \frac{I_{ss}(z_f)}{I(z_f,0)} = (1 + N_Q)^{-2}, \qquad \text{(A-III-6)}$$

where

$$N_Q = \frac{4(-\mu_T)\alpha P \ell^2 F^3 (\dot{x}_\ell + \dot{x}_0) e^{-\alpha \ell (-\dot{x}_0/\dot{x}_\ell)}}{\pi \rho c_p a_0^3 (F\dot{x}_\ell + (F-1)\dot{x}_0)^2}. \qquad \text{(A-III-7)}$$

In practice, I_{rss} was found not to follow strictly Eq. (A-III-6) but instead to be characterized by the thermal blooming parameter N_Q according to (5)

$$I_{rss} = (1 + 0.85\, N_Q + 0.09\, N_Q^2)^{-1}. \qquad \text{(A-III-8)}$$

The credibility of this model for stagnation zone thermal blooming was enhanced further by the finding (5) that, in addition to being a useful parameter for characterizing the thermal blooming data, N_Q correctly predicts the scaling of thermal blooming severity with the focusing ratio, F, this scaling being linear in F in the limit of large F.

Central to Berger's treatment is the statement that $t\delta z$ equaling $4a(z')/w$ expresses the steady state situation that convective cleanout of heated medium at the ends of the range places the limit to the strength of the lens; an alternative treatment is the statement that $t\delta z$ simply be on the order of a_o/w or $a(z_f)/w$ after the establishment of the steady state. The replacement of $t\delta z$ by $a(z_f)/w$ results in a thermal blooming distortion parameter which is independent of F at large F, in variance with Fleck's analytical results.(7) In contrast, replacing $t\delta z$ with a_o/w gives

$$N_L = \frac{(-\mu_T)\,\alpha P \ell^2 F^4 \dot{x}_\ell (\dot{x}_\ell + \dot{x}_0) e^{-\alpha\ell(-\dot{x}_0/\dot{x}_\ell)}}{\pi \rho c_p \; a_0^3 \; (F\dot{x}_\ell + (F-1)\dot{x}_0)^3}. \qquad \text{(A-III-9)}$$

as the relevant blooming parameter in the expression

$$I_{rss} = (1 + N_L)^{-2}. \qquad \text{(A-III-10)}$$

It is found that Eq. (A-III-10), like Eq. (A-III-6), is not strictly adhered to but instead an expression, similar to (A-III-8) is developed involving N_L to express the stationary stagnation zone data.

At this point is is interesting to consider some properties of Eq. (A-III-9). Of particular interest is the severity of thermal blooming and its dependence on stagnation zone position and degree of focus. This question is simplified by considering the function

$$\chi(\dot{x}_\ell, \dot{x}_0, F) = \frac{F^4 \dot{x}_\ell (\dot{x}_\ell + \dot{x}_0) e^{-\alpha\ell(-\dot{x}_0/\dot{x}_\ell)}}{(F\dot{x}_\ell + (F-1)\dot{x}_0)^3} \qquad \text{(A-III-11)}$$

which contains all the kinematic and focusing dependence of N_L. This function is plotted vs $\dot{x}_\ell$ in Fig. A5 for the indicated values of $\dot{x}_o$ and $\alpha\ell$, the value of the latter being characteristic for a one meter cell containing ten atmospheres of CO_2. It is seen that the effect of increasing F is to cause χ to exhibit a sharper and higher maximum. At large $\dot{x}_\ell$, when the stagnation zone is close to the laser, the value of N_L is seen to tend to be linear in F. Conversely, for a stagnation zone positioned progressively closer to the source, the value of I_{rss} is expected to exhibit a minimum with a relatively sharp recovery for larger values of F and a shallower minimum for smaller F values. As seen in Fig. A4b the value of I_r does indeed exhibit a minimum followed by a marked recovery as the stagnation zone moves toward the source, suggesting that for the gas mixture and zone velocity considered, the instantaneous value of I_r is given by I_{rss} corresponding to the instantaneous value of N_L. As is the case for N_Q it is not expected that the measured value of I_{rss} to be given in terms of N_L exactly as in Eq. (A-III-6) but that I_{rss} show a functional dependence on the many quantities of importance to blooming in the presence of a stagnation zone through the single parameter N_L.

SECTION AIV

EXPERIMENTAL RESULTS

A. INTRODUCTION

The results of the measurements of I_r for propagation through a stagnation zone are presented in this section. In the first subsection, properties of stationary stagnation zones are investigated, specifically the dependence of I_r on linear attenuation over the range and degree of focus, and the experimental results, along with those of Berger(5)(6) and analytical results by several workers as presented by Berger(5) are shown as functions of N_Q and N_L. In the second subsection, thermal blooming in a moving stagnation zone is examined., again as a function of attenuation, degree of focus and laser power. The prinicple conclusion is that for the zone velocities considered, the time dependence of I_r is determined by the time dependence of N_L or N_Q and the sensitivity of I_r in the stationary zone case on these parameters.

B. STATIONARY STAGNATION ZONES

As was discovered by Berger(4) and as is indicated in Fig. A4a, the value of I_r for a beam propagating through a stationary zone experiences a transient decay before assuming a constant value whose magnitude is determined by the properties of the propagating medium, the laser beam and the kinematics determining the stagnation zone position in the range. Data obtained from oscillograms as that in Fig. A4a is shown in Fig. A6 which illustrates the dependence of I_r on kinematics for the indicated values of focusing degree and attenuation over the range. Qualitatively, the value of I_r is seen to behave in a manner consistant with that shown for $X(\dot{x}_\ell, \dot{x}_o, 5)$ in Fig. A5, exhibiting a sharp drop as the net wind speed at the exit window increases through zero, a minimum soon thereafter and gradual increase at still larger net wind speeds. This behavior gives rise to the expectation that N_L as well as N_Q is a suitable parameter characterizing thermal blooming in a stagnation zone.

The value of I_r is plotted as a function of N_Q in Fig. A7. Also included is experimental data taken by Berger(5) and analytical results obtained by Ulrich and Wallace and Fleck, as presented by Berger(5), and Fleck(7). The data taken in the present study is seen to be self consistant for a fixed value of F. For Berger's data the value of N_Q was calculated from Eq. 16 in Ref. 5 assuming a linear taper in the laser beam radius with range position. In addition Berger's function R(x) was set equal to unity independent of zone position.

In comparing Berger's data with the present, it is recalled that in some of his experiments, Berger used a detector fixed at the cell exit so as to sample the intensity only on the axis of the unperturbed beam(2) while in others he used a rotating mirror to sweep the beam across the detector with the cell positioned horizontally thereby giving rise to bouyancy generated gas flow(4) transverse to the beam axis. Thus, in the former experiments, Berger measured a property, the "on-axis" intensity, different than that measured in the latter and in the present experiment, the "maximum intensity". As calculated by Fleck(7) the latter is expected to exceed the former by as much as a factor of two. However, it is seen that the scatter in the experimental results obscures this difference except for the tendency in Bergers data to lie slightly but consistently lower than the present at a given value of the distortion parameter.

In Fig. A8 the dependence of I_r on N_L is presented. The only discernable difference between the presentations in Figs. A7 and A8 is the tendency of the data to be somewhat more tightly clustered about the fitted curve when plotted in terms of N_L. Agreement with the analytical results is good using either N_Q or N_L. For comparison, I_r is plotted against N_L', obtained using $a(y_f)$ in the steady state expression for $t\partial z$, in Fig. A9. Presented in terms of N_L', tight clustering about the fitted curve is again observed particularly for the low F value data. However, agreement with Fleck's calculations for large F is very poor, indicating that N_L' exhibits incorrect sensitivity to degree of focus.

The stationary stagnation zone data presented here was taken to expand the data base used in studying moving stagnation zones. In the next subsection, moving stagnation zone data is examined and compared to the stationary zone data presented above.

C. MOVING STAGNATION ZONES

As seen in Fig. A4b the value of I_r for the moving stagnation zone case may exhibit significantly more temporal variation than does its value in the stationary zone case.

The data of Fig. A4b, representing one of several data runs taken at the indicated $\alpha\ell$ and F values with varying values of y_o and $\Delta_{\dot{x}}$, ($\Delta_{\dot{x}} \equiv \ddot{x}_\ell/\dot{x}_o$), is shown in its reduced form in Fig. A10 along with information obtained from steady state data. The data point denoted by a cross is the measured value taken on the same day, of the steady state I_r in a stationary zone experiment with the same $\dot{x}_\ell$ and $\dot{x}_o$ as occurred at the instant of time indicated in the moving zone experiment. The coincidence between this point and the moving zone data indicates that I_r for a moving zone characterized by temporally varying $\dot{x}_\ell$ and $\dot{x}_o$ is determined at any instant by the steady state value of

I_r corresponding to the values of $\dot{x}_\ell$ and $\dot{x}_o$ at that instant. The solid line indicates the value of I_r calculated from the curve drawn through the data in Fig. A8. The agreement between this curve and the data is particularly good with the curve tracing the temporal variation of I_r as well as its magnitude very well.

A data run, taken for a F value of 1.2 is shown in Fig. A11. As predicted in Fig. A5 the variation of I_r with zone position is less pronounced for the more weakly focussed case. Also shown are the steady state value of I_r predicted by the expression for N_L, which also indicates the smaller degree of temporal variation expected at lower F values.

The results shown in Figs. A10 and A11 are seen to be restricted to values of I_r above about 0.3 with a corresponding restriction on the range of the relevant thermal blooming parameters studied. To expand this range, measurements were taken with the apparatus kinematics essentially fixed and with the value of P varied between 5.6 and 16 W and $\alpha\ell$ between 0.21 and 0.45, and the data from these runs is shown as oscillograms in Fig. A12 and in the steady state parameter plot in Figs. A13.

Inspection of the data shown in Fig. A12 reveals that an increase in the product α and P from .011 to 0.72 W/cm does not affect the ability of the medium to respond to the presence of the laser beam and the kinematics of the encounter. The relatively small temporal variation of the peak intensity as observed in Fig. A12a is due to the fact that the departure of I_r from unity is relatively small under these conditions. The data in Fig. A12 is reduced and plotted in Fig. A13 as a function of N_L. In this plot only I_r values occuring after the initial transient are plotted. This data is compared in each figure with the steady state data of Fig. A3. In each comparison the moving zone data is seen to correlate with the previously existing steady state data within the experimental reproducability exhibited by the latter. As a result the conclusion is drawn that, for the encounter kinematics considered in the measurement, I_r, once having reached a value corresponding to the steady state value I_{rss} associated with the thermal blooming parameter N_L (or N_Q), will change in accordance with the sensitivity of I_{rss} to the time varying value of N_L. It is important to emphasize that I_r is determined by N_L only after a steady state condition is reached. For example, the data in Fig. A12 correspond to a situation in which a stagnation zone passes into the range from behind the target. This occurs at roughly 0.1 sec in the oscillograms shown. Prior to that time, no stagnation zone is present and I_r is given quite accurately in terms of Gebhardt and Smith's thermal blooming parameter N.(3) The data shown in Fig. A13 were all taken at times equal to or greater than 0.25 sec, leaving a time interval of 0.15 sec in which N_L overestimated, by as great as an order of magnitude, the severity of thermal blooming. This interval is seen from Fig. A12 to be independent of the responsivity of the medium, which is proportional to αP, and this indicates that the time required to set up the steady state condition is established by the kinematics of the cell as expressed by some relationship between $t\partial z$ and the ratio of the beam radius at some point in the range to w.

D. STEADY STATE PARAMETERS

In the preceeding paragraphs three distinct stagnation zone parameters, designated N_L', N_Q, and N_L, have been used in analyzing the data. Each parameter arises from a different approximation for the relationship at steady state between $t\partial z$ and the ratio between the beam radius at some point in the range to w. In the case of N_L' the beam radius was that associated with the end of the range, a_f, ($a_f \equiv a(z_f)$), where, in a focused beam, the radius is smallest and the contribution to thermal blooming is largest. Although intuitively a_f would thus seem to be the critical radius in determining the onset of the steady state, it was seen that N_L' becomes less effective in describing steady state thermal blooming by a stagnation zone as the degree of focus increased. In contrast, N_L is derived using a_o as the critical beam radius, and N_Q uses a_s, ($a_s \equiv (a(z'))$. Both N_L and N_Q were seen to exhibit the correct dependence on the degree of focus with the data exhibiting a slightly tighter fit to an analytic function when expressed in terms of N_L.

It is interesting at this point to try to decide which of the two parameters N_L or N_Q more accurately describes the physics involved in stagnation zone thermal blooming. In deriving N_Q, Berger(5) described the onset of steady state situation with the equation

$$w(z_2 - z_1)t_{ss} = 2(a(z_1) + a(z_2)) \qquad \text{(A-IV-1)}$$

where z_1 and z_2 are the boundaries of the "thin" thermal lens. Assuming a linear taper for the focused laser beam the right hand side of Eq. (AIV-1) is equal to $4a_s$ and a plot of the experimentally observed value of t_{ss}, the time elapsed at the onset of the steady state, as a function of $4a_s/z_fW$ would be expected to be a straight line whose slope is the ratio $z_f/(z_2-z_1)$. Figure 14 presents such a plot using Bergers data.(5) Berger took his data parametric in w at fixed z', and the data points denoted with a cross represent the run at each z' for which w was largest. It is seen that these points fall closest to the straight line for which $z_f/(z_2-z_1)$ equals 5. When the slew rate is large, transverse convection is most likely to dominate the distribution of absorbed laser energy in the medium and t_{ss} will most likely reflect the rate at which the slew generated transverse flow removes heated medium from the beam path. At slower slew rates other energy disposal channels such as bouyant convection increase in importance, and t_{ss} is expected to fall below the value expected for the slew dominated case. As seen in the figure, it would seem that Berger's value of 5 for $z_f/(z_2-z_1)$ is a reasonable lower brand for the slew dominated case. The N_Q model requires that the quantity $t_{ss}\ z_f w/a_s$ be independent of z' and have a value of about 20. However, when plotted against z'/z_f, as in Fig. 15, this quantity is seen to show a systematic variation, increasing linearly with z'/z_f as a_s decreases. On the other hand, when plotted against z'/z_f as in Fig. 16 for the data of largest slew rate, the quantity $t_{ss}\ z_f w/a_o$ is essentially constant with a value of about 10 as an upper bound, a value consistant with the data shown in Fig. 17 which presents t_{ss} vs $4\ a_o/z_f w$. These results infer that the value of t_{ss} is determined by a_o rather than by a_s and is given by

$$t_{ss} = 4a_0/wfz_f \qquad \text{(A-IV-2)}$$

where the value of f is roughly 2/5. In addition it would seem that N_L rather than N_Q is the relevant parameter in describing laser beam propagation through stagnation zones.

SECTION AV

SUMMARY

In this study measurements have been made of the reduction in peak on-target intensity due to thermal blooming in stagnation zones. Measurements were carried out for both stationary and moving stagnation zones. The work involving stationary zones served to expand the data base, initiated by Berger, to include a wider range of values of F, $\alpha \ell$ and P. It was found that the stationary zone data was expressable in terms of a single thermal blooming parameter, N_L, which is a slight modification on Berger's parameter N_Q. The measurements with moving zones indicated that the measured intensity tends to track the stationary zone value as given in terms of N_L with the observed temporal dependence in the intensity being determined by the temporal dependence of N_L.

One area yet to be addressed in this study of moving stagnation zones relates to the question of just how fast are the zones studied moving and how fast are the zones typically encountered in the naval scenario expected to move. The quantity relevant to this question is obtained from considering the position of the stagnation zone within the range as a function of time which for the laboratory apparatus is given by Eq. (AII-1). Routine calculations reveal that dy_o/dt is largest for time zero and when the zone is just entering the range,

$$\left.\frac{dy_o}{dt}\right)_{maximum} = \frac{\dot{x}_\ell}{-\dot{x}_o} . \tag{AV-1}$$

For the naval scenario considered in Ref. 1, this value of $\dot{y}_o(\max)$ can be calculated to be 0.4 $\sec^{-1}$. For the data in Fig. A12 this quantity is nine $\sec^{-1}$, indicating that the zones studied are moving quite rapidly as viewed in the context of the naval scenario. Thus, the conclusions reached concerning the stagnation zones studied in these experiments are applicable to those encountered in the naval scenario.

In final summary, combining the results of the present measurements with previous experimental and analytical results leads to the following conclusions: For a stationary stagnation zone, the intensity experiences an initial transient, after the laser is turned on, before reaching a steady state value. The time elapsed before the latter is reached is given approximately by 10 $a_o/z_f w$ where a_o is the beam radius at the laser, z_f is the laser-to-target distance, and w is the laser beam slew rate. The steady state intensity, normalized to its value in the absence of thermal blooming effects, is given by

$$I_f = \left(1 + 3.0 N_L + 0.37 N_L^2\right)^{-1} \qquad \text{(A-V-II)}$$

where N_L, the stagnation zone thermal blooming parameter is given by

$$N_L = \frac{-\mu_T \alpha P e^{-\alpha z'} Z_f (1 - Z'/Z_f) a_o}{\pi \rho C_p \omega a(z')^3 a_f} \qquad \text{(A-V-III)}$$

where the symbols used stand for the following physical quantities:

μ_T ≡ medium's refractive index temperature coefficient
α ≡ medium's absorption coefficient
P ≡ laser beam power
z' ≡ distance of stagnation zone from the laser
a(z) ≡ laser beam radius = $a_o - (a_o - a_f)\, z/z_f$
a_f ≡ beam radius at target
ρ ≡ medium's mass density
c_p ≡ medium's specific heat
a_o/a_f ≡ degree of focus.

For a moving stagnation zone, the time dependence of z' and therefore of N_L is determined by the background wind speed and w, and it was found that the above expression for N_L was obeyed for both stationary stagnation zones and zones moving at least to ten times more rapidly than those expected in a typical naval scenario.

APPENDIX

TIME DEPENDENT MODEL FOR STAGNATION ZONE THERMAL BLOOMING

A. INTRODUCTION

In section A-III and Ref. 5, models were described which account for thermal blooming in the presence of a stagnation zone only after the cessation of the transient intensity decay leading to a steady state. The problem of thermal blooming in the presence of a moving stagnation zone is inherently time dependent, and the development of a model accounting for this time dependence is desirable.

B. TIME DEPENDENT MODEL

In principle this need is filled by a solution to Eq. (A-III-4) which was solved for the stationary zone by making certain assumptions about the thermal lens thickness δz. For a moving zone such a treatment is complicated by the fact that the boundaries defining δz are moving in a complicated manner, and although this motion can be accounted for in a numerical solution to Eq. (A-III-4), it was desired to reduce the problem if possible to a simple one parameter expression analogous to Eq. (A-III-8) with the elapse of time included. This goal was achieved by a synthesis of a solution (3) of the thermal blooming equation,

$$\bar{\nabla} \cdot \left(I/\mu\left(\int \bar{\nabla}\mu \, ds + \mu \hat{s}\right)\right) = -\alpha I, \qquad \text{(A-A-1)}$$

and some results of the thin thermal lens analysis of thermal blooming. Briefly, using certain assumptions concerning the variation of I along the propagation path, Eq. (A-A-1) is solved(3) for situations in which the absorbed power density αI is balanced by a single energy loss channel for the following loss channels: 1) medium heating, 2) thermal conductivity, 3) transverse convection. For each channel operating alone, the solution of Eq. (A-A-1) can be expressed in the form

$$I_r = e^{\psi} \qquad \text{(A-A-2)}$$

where Ψ is the product of ℓ^2/a_o^2, the fractional change, relative to ambient $\mu_T \Delta T/\mu$ of the index of refraction on the laser beam axis, a factor, $f(\alpha\ell)$, a factor $g_c(F)$ and, for the case of convection, a factor Φ which is a function of ϕ, the ratio of the wind velocity at ℓ to that at the laser, v_o. These quantities are listed in the table below.

Loss Channel	ΔT	$f(\alpha \ell)$	$g_c(F)$	$\Phi(\phi)$
Medium Heating	$\frac{\alpha P t}{\pi \rho c_p a_0^2}$	$\frac{2(e^{-\alpha \ell}-1+\alpha \ell)}{\alpha^2 \ell^2}$	$\frac{F(F+2)}{3}$	
Thermal Conduction	$\frac{\alpha P}{4\pi k}$		$\frac{2F(F \ln F-(F-1))}{(F-1)^2}$	
Transverse Convection	$\frac{\alpha P}{2\pi^{1/2}\rho c_p a_0 v_0}$		$\frac{2F^2((F-1)-\ln F)}{(F-1)^2}$	$\frac{2(\phi \ln \phi-(\phi-1))}{(\phi-1)^2}$

When all three loss channels are included in the energy balance equation,

$$\frac{4k\Delta T}{a^2} + \frac{\rho c_p \Delta T}{t} + \frac{\rho c_p V \Delta T}{a} = \frac{\alpha P}{\pi a^2}, \tag{A-A-3}$$

the value of ΔT can be expressed as follows:

$$\Delta T = \frac{\alpha P}{\pi \rho c_p a^2}\left(\frac{1}{t} + \frac{4k}{a^2 \rho c_p} + \frac{V}{a}\right)^{-1}, \tag{A-A-4}$$

and it is seen that ΔT has a form similar to that for the medium heating case with t replaced by t*, a "reduced time" given by the quantity in brackets in Eq. (A-A-4).

As a parallel to Eq. (A-A-4), it is postulated that the general expression for Ψ in the stagnation zone problem is

$$\psi^* = \frac{\mu_T \alpha P \ell^2 f(\alpha \ell) g_{MH}(F)}{\pi \mu \rho c_p a_0^4}\left(\frac{1}{t} + \frac{4k g_{MH}(F)}{a_m^2 \rho c_p g_{cond}(F)} + \frac{V g_{MH}(F)}{\pi^{1/2} a_m g_{conv}(F)}\right)^{-1}, \tag{A-A-5}$$

where the factor $(-\mu_T \alpha P \ell^2 f(\alpha \ell) g_{MH}(F)/(\pi \mu \rho c_p a_o^4))^{-1}$ is the transient thermal blooming time as referred to in Section A-II. It is seen that $\Phi(\phi)$ is set equal to 2, its value for a stagnation zone at the target in Eq. (A-A-5). This is done because in the presence of a stagnation zone at any other point within the range the transverse medium velocity vanishes at the zone center and the integral defining the value of $\Phi(\phi)$ has no meaning. It is also seen that within the parentheses the beam radius is denoted by a_m; it is concerning this variable that the second postulate of the model is made. From Eq. (A-III-5) it is possible to determine z_m, the value of z' at which the placement of a negative lens of arbitrary focal length, f, has the greatest perturbative effect on I_r. This is conveniently done by determining the value of z' corresponding to the maximum in the second term within the brackets in Eq. (A-III-5) and it is found that

$$z_m' = \frac{2F-3}{2F-2} \; . \qquad \text{(A-A-6)}$$

It is now postulated that for F greater than 1.5, a_m be set equal to $a(z_m)$, for F smaller than 1.5 a_m be set equal to a_o; in addition, the value of v is set equal to its value that at z_m. Specifically, v is the product of w and the distance between z' and z_m. In terms of the apparatus dimensions and kinematics,

$$v = \left| \dot{x}_0 + z_m \ell^{-1} (\dot{x}_\ell + \ddot{x}_\ell t) \right| \qquad \text{(A-A-7)}$$

The dependence of $g_{mH}(F)t^*$ on $\dot{x}_\ell$ and F is shown in Fig. A1A. In this figure the value of t is taken to be infinite so that t* is composed only of the convective and conductive terms. As was the case for the thermal lens model, the effect of increasing F from 1.2 to 5.0 is to cause an increased $\dot{x}_\ell$ dependence of Ψ^*. Unlike the results shown in Fig. A-5 for $\chi(\dot{x}_1, -4, F)$, further increase in F results in a flatter $\dot{x}_\ell$ profile. The cause of this is the assumption of constant a_o in the curves shown which results in smaller a_m with increasing F and thus an increasing role of conduction rather than convection in determining t* at the larger F values. Conduction was not included in the thermal lens model, and its inclusion in the present analysis points out its applicability to situations other than stagnation zone thermal blooming as shown by the extension of the curves to values of $\dot{x}_\ell$ smaller than [illegible] cm/sec for which the value of N_L or N_q is undefined. Indeed in the absence of a stagnation zone and conduction and transient effects, the expression for Ψ^* is seen to be quite similar to the parameter $N^{(3)}$ used to characterize thermal blooming in the presence of a transverse wind.

As was the case for N_L, the important results of this model is the development of a single parameter Ψ^* to characterize thermal blooming.

C. EXPERIMENTAL RESULTS

The sensitivity of Ir to Ψ^* is shown in Fig. A2A for both the present experiments, Berger's experiments(5) and the analytical results of Ulrich(5), Wallace(5), and Fleck(5,7). It is seen that all the experimental results correlate fairly well with Ψ^* and with each other but that the analytical results for larger F values fall away from the lower F results, indicating that Ψ^* does not contain the correct dependence on F. The moving zone results, shown in Fig. A-3-A, indicate that the time dependence of I_r is determined by that of Ψ^* as was the case for the parameters N_Q and N_L.

The fact that Ψ^* exhibits incorrect sensitivity to F can be altered by simply replanning a_m with a_o in Eq. (A-A-5). However consistancy requires that doing so forces z_m in Eq. (A-A-7) to be replaced by zero, thereby rendering v and therefore Ψ^* time independent in the limit of large values of t, also losing for Ψ^* its sensitivity to $\dot{x}_\ell$ and therefore stagnation zone position.

In summary, the model described produces a thermal blooming parameter Ψ^* which correctly traces the temporal evolution of I_r in the presence of moving or stationary stagnation zones except for large values of F. To give the correct dependence on F it would seem that the third term in parenthesis in Eq. (A-A-5) must be divided by F.

REFERENCES FOR SECTION A

1. M. C. Fowler, J. R. Dunphy, and D. C. Smith, Laser Propagation Experiments-Aerosol and Stagnation Zone Effects, United Technologies Research Center Report R76-922578-6, October 1976.

2. P. J. Berger, F. G. Gebhardt, and D. C. Smith, Thermal Blooming Due to a Stagnation Zone in a Slewed Beam, UARL Report 921724-12, October 1974.

3. D. C. Smith, High Power Laser Propagation: Thermal Blooming, United Technologies Research Center, Report UTRC76-164, December 1976.

4. R. T. Brown, P. J. Berger, F. G. Gebhardt and D. C. Smith, Influence of Dead Zones and Transonic Slewing on Thermal Blooming, UARL Report N921724-7, February 1974.

5. P. J. Berger, Thermal Blooming of a Slewed Laser Beam Containing a Stagnation Zone: Analytical Model for the Quasi Steady State, United Technologies Research Center, Report UTRC75-39, 1975.

6. P. J. Berger, unpublished experimental results.

7. J. A. Fleck, Jr., J. R. Morris, and M. J. Feit, Time Dependent Propagation of High Energy Laser Beams Through the Atmosphere, Lawrence Livermore Laboratory, Report UARL-51826, June 1975.

8. F. G. Gebhardt and D. C. Smith, Investigation of Self Induced Thermal Effects of CO_2 Laser Radiation Propagating in Absorbing Gases, UARL Report K921004-4, April 1971.

APPARATUS FOR MOVING STAGNATION ZONE EXPERIMENT

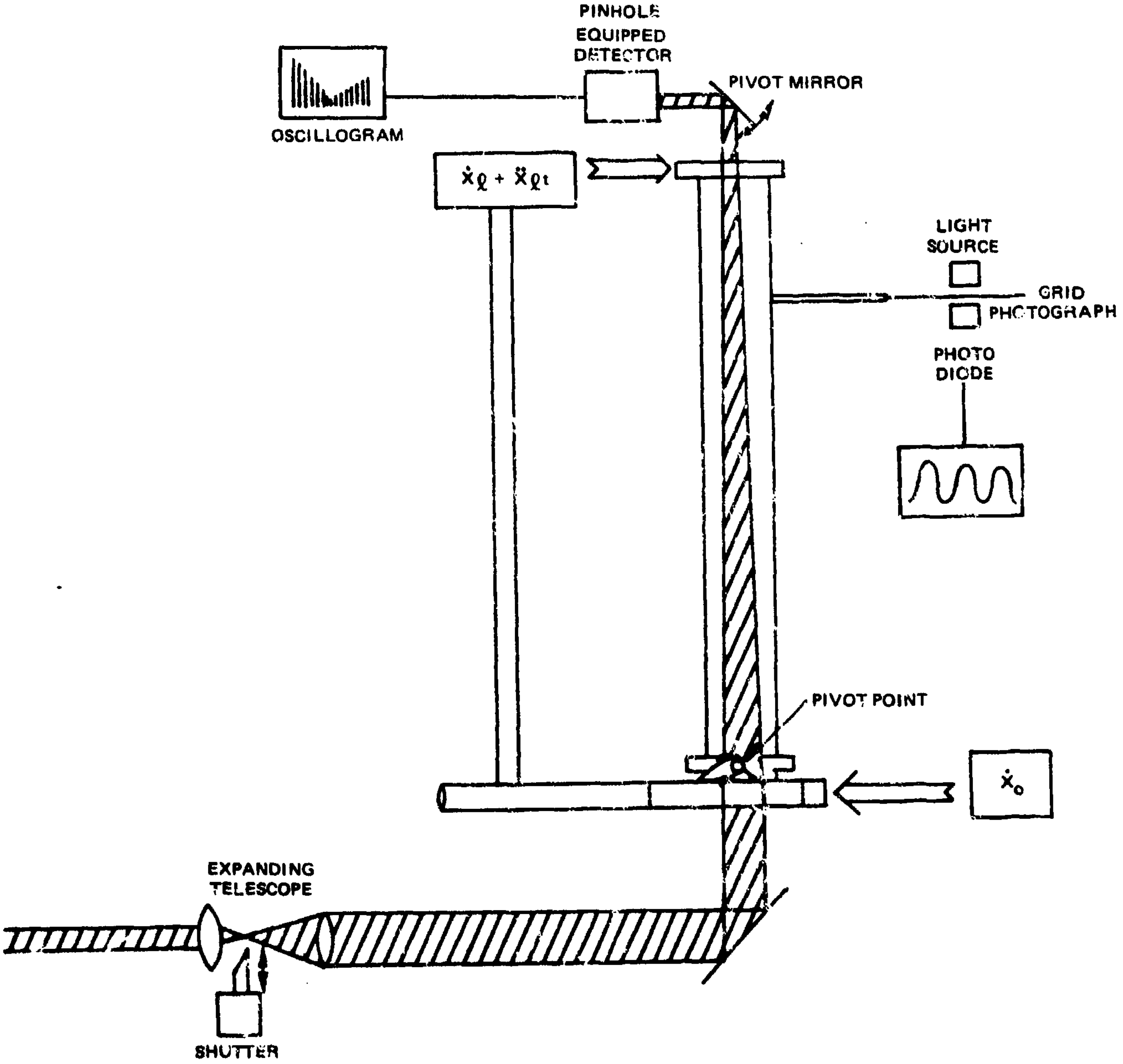

76–10–100–3

DETERMINATION OF BEAM DIAMETER AT FOCUSING TELESCOPE

ℓn(1–P(d)/P) VS d^2

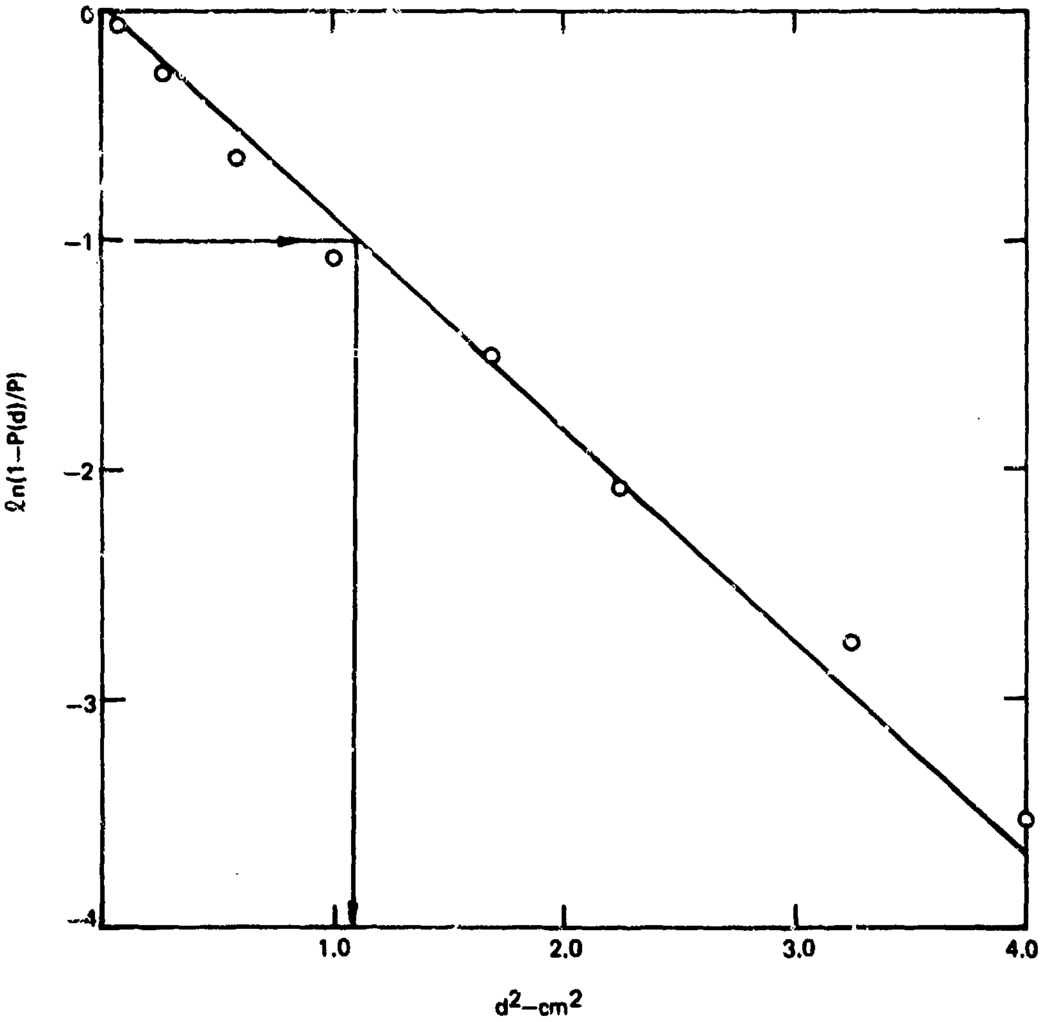

DETERMINATION OF BEAM DIAMETER AT DETECTOR

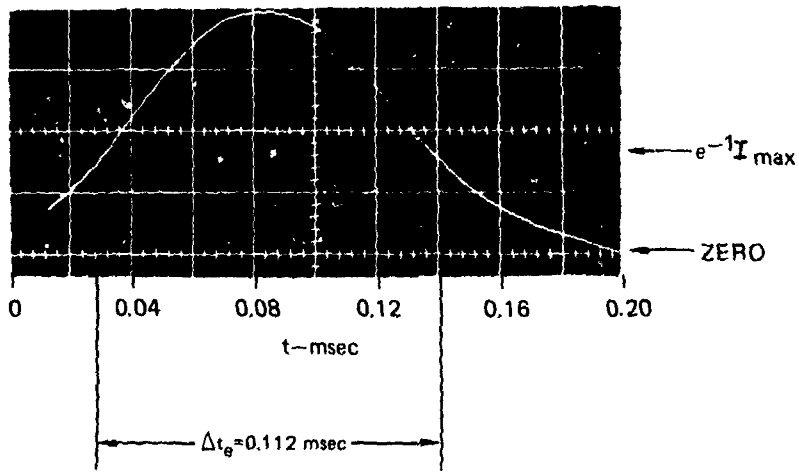

$d^*(0) = V\Delta t_e$

$V = 850$ cm/sec

$d^*(0) = 0.095$ cm

STAGNATION ZONE DATA RECORDS—PEAK INTENSITY VS TIME

$a\ell = 0.15$

P=18W

$\dot{x}_0 = -4.0$ cm/sec

F=4.0

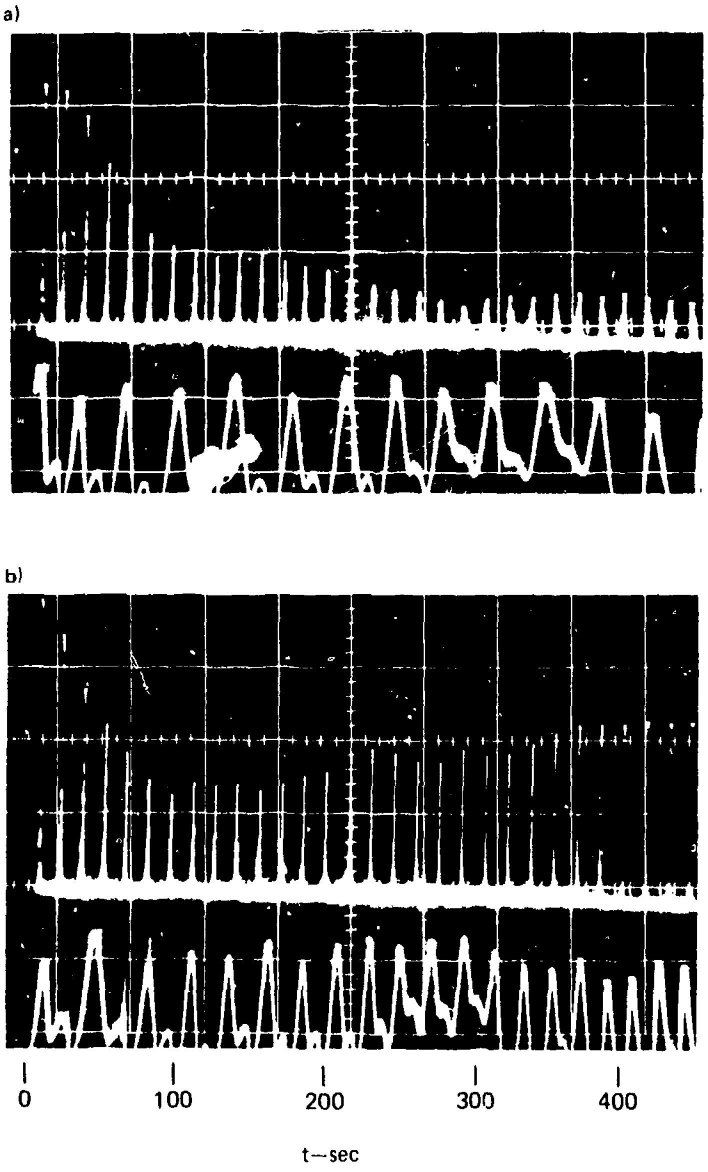

a) $\dot{x}_\ell = 5.3$ cm/sec

$\ddot{x}_\ell = 0.0$ cm/sec^2

$\gamma_0 = 0.75$

b) $\dot{x}_\ell = 5.8$ cm/sec

$\ddot{x}_\ell = 27$ cm/sec^2

$\gamma_0 = \frac{0.69}{(1+4.7t)}$

KINEMATIC DEPENDENCE OF N_L

$\dot{x}_o = -4.0$ cm/sec

$a\ell = 0.45$

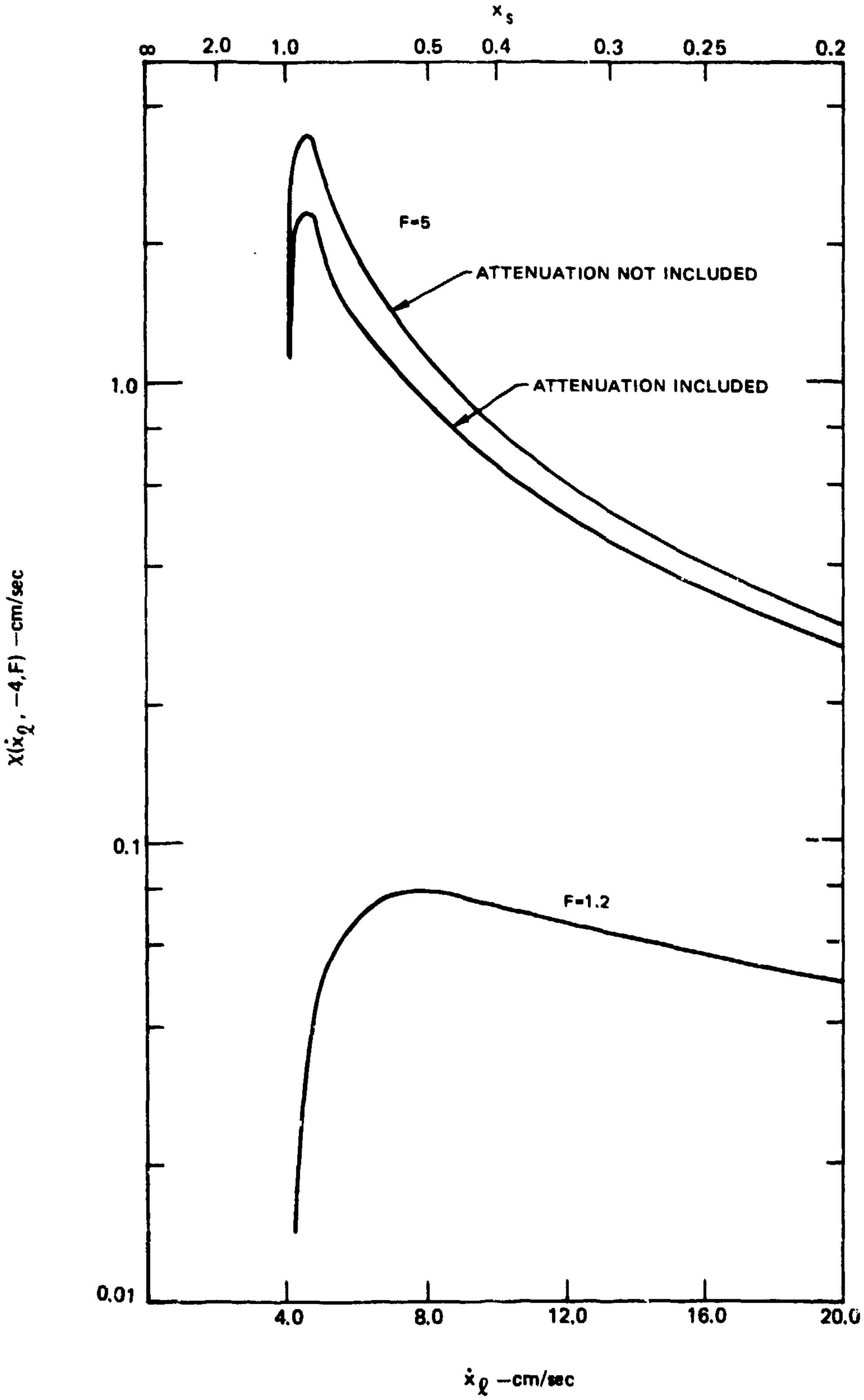

FIG. A–6

STAGNATION ZONE EFFECT ON DELIVERED INTENSITY

EXPERIMENTAL RESULTS
STATIONARY ZONE

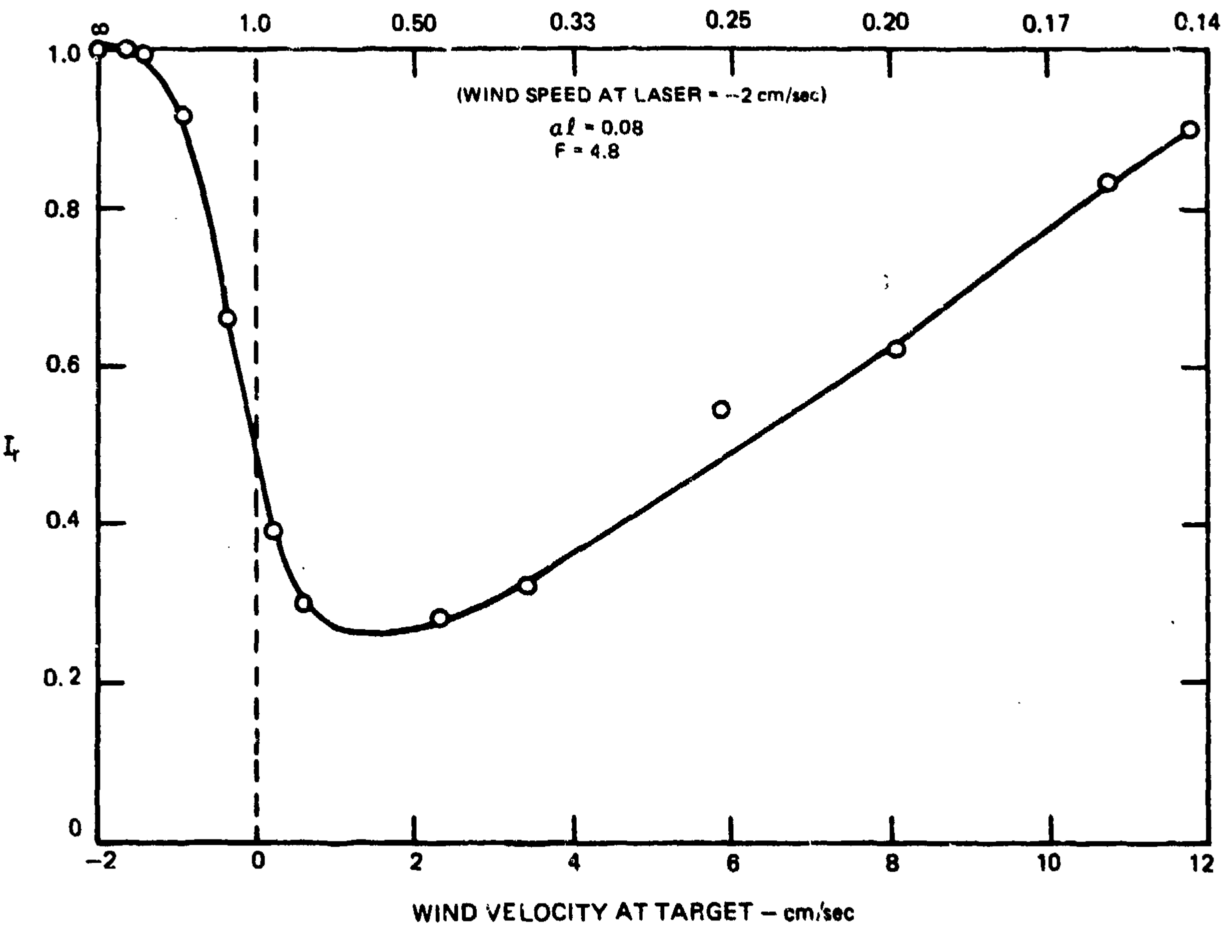

77–02–53–2

STATIONARY STAGNATION ZONE RESULTS VS $N_Q/4$

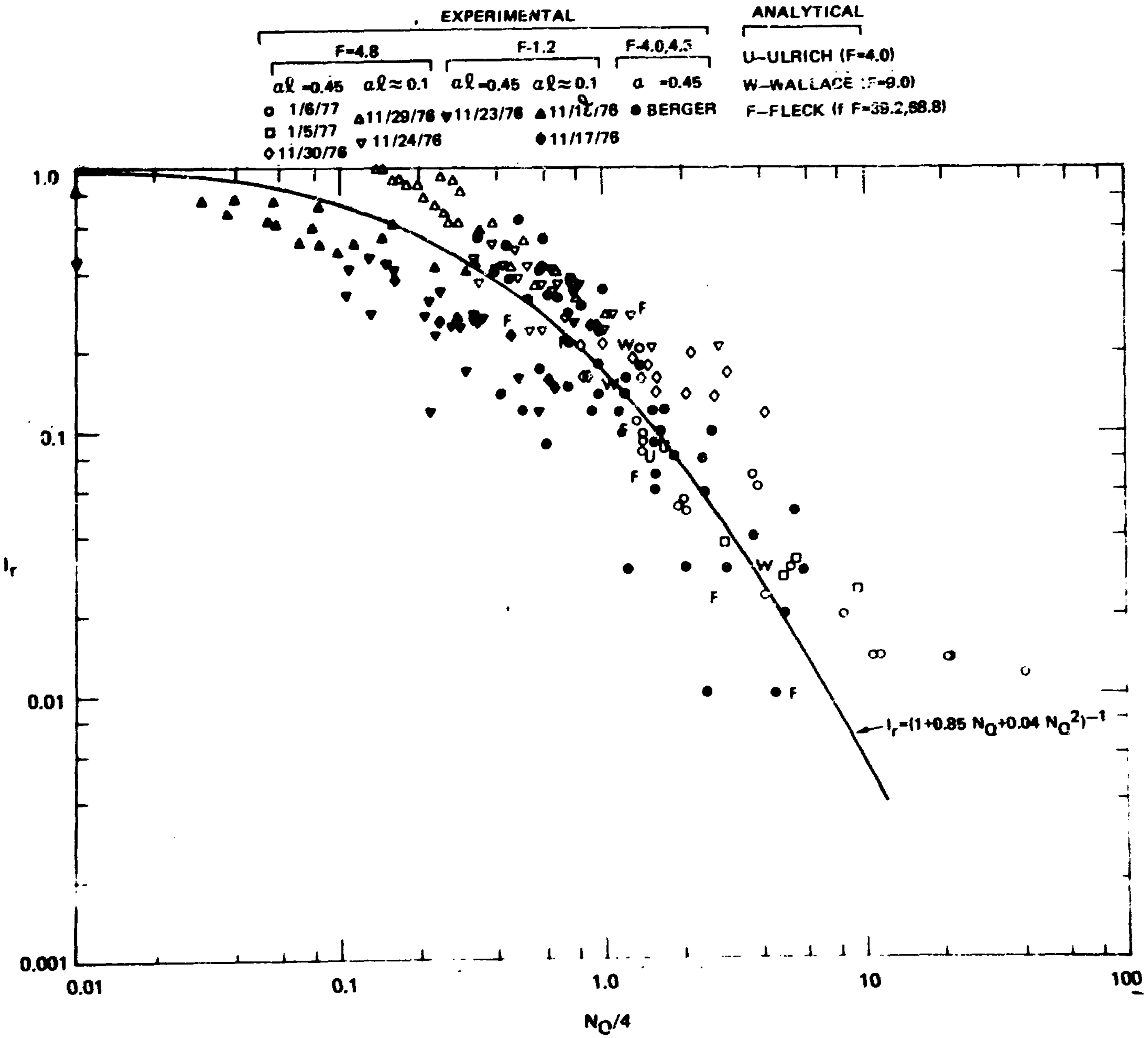

STATIONARY STAGNATION ZONE RESULTS VS N_L

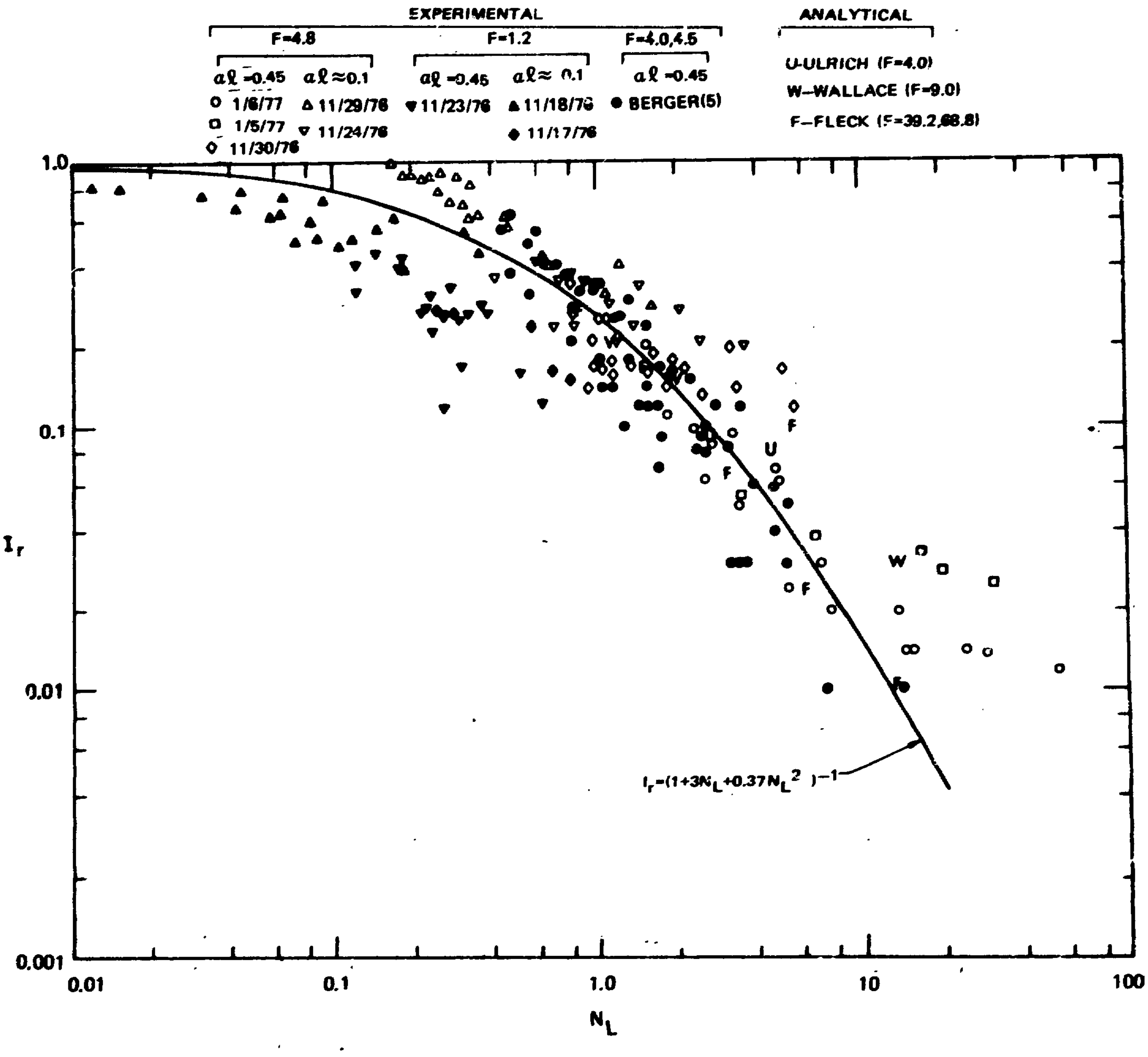

STATIONARY STAGNATION ZONE RESULTS VS N_L'

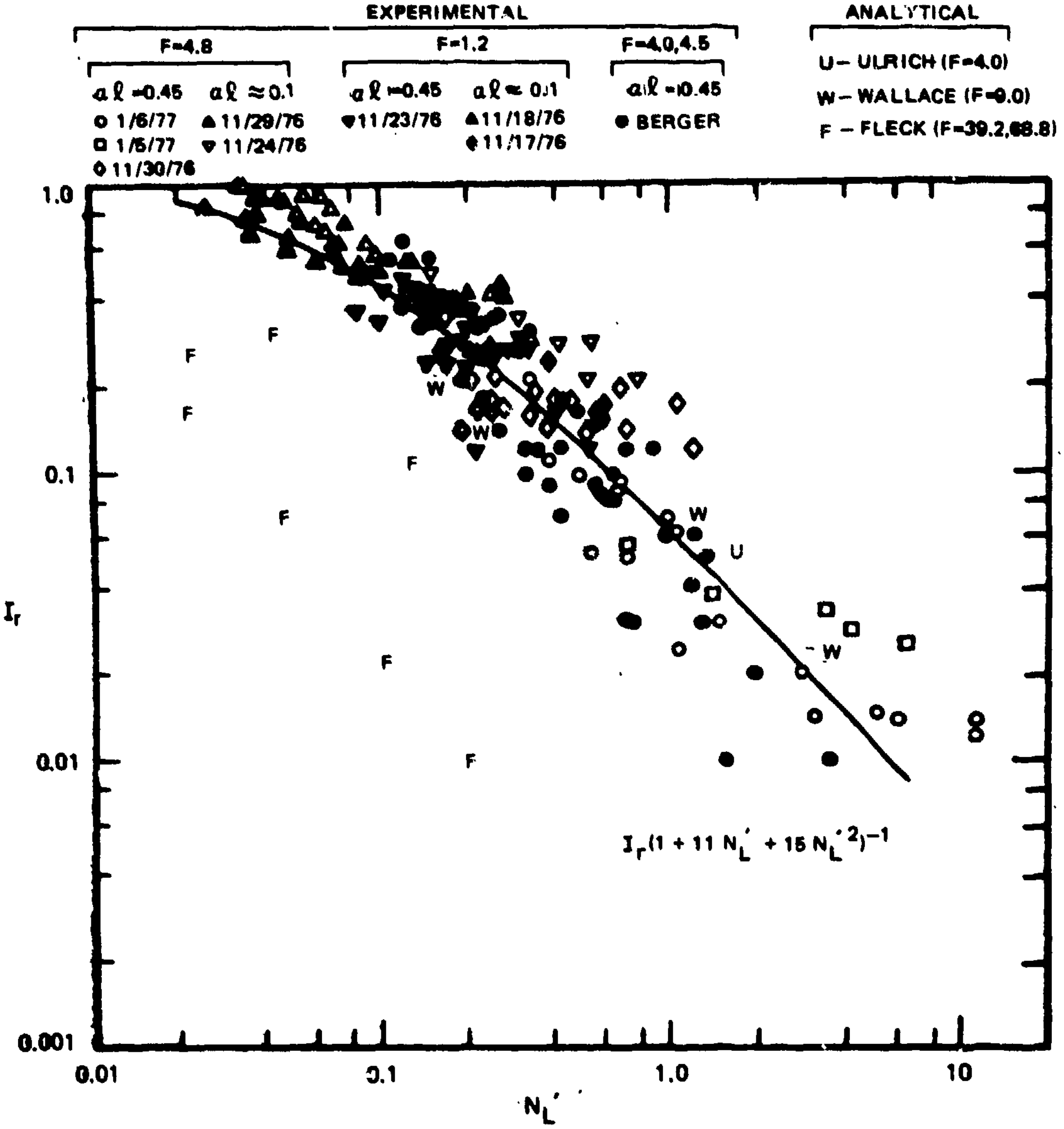

MOVING STAGNATION ZONE EXPERIMENT

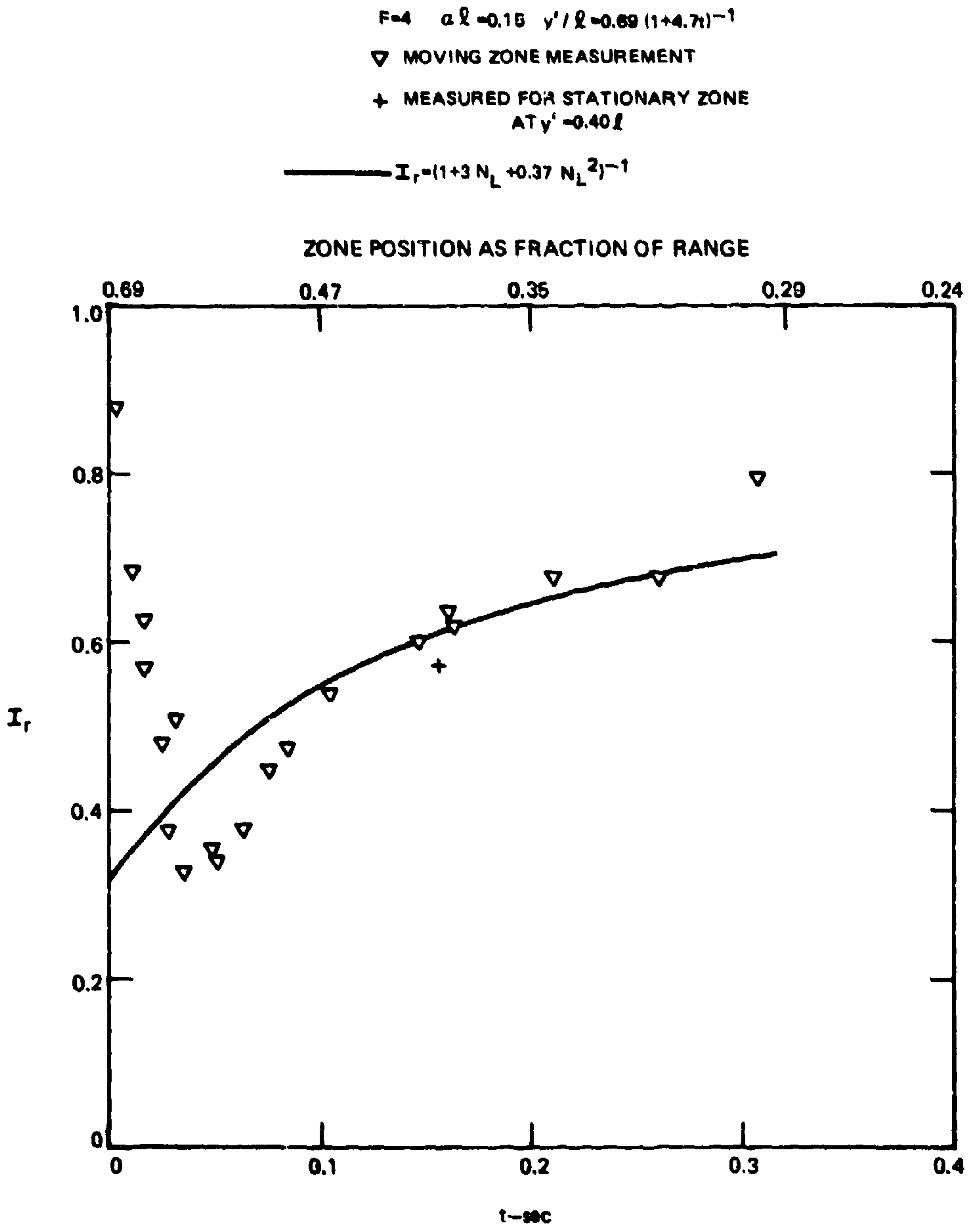

MOVING STAGNATION ZONE EXPERIMENT

$F=1.2 \quad a\ell=2.0 \quad y'/\ell=0.51(1+3.5t)^{-1}$

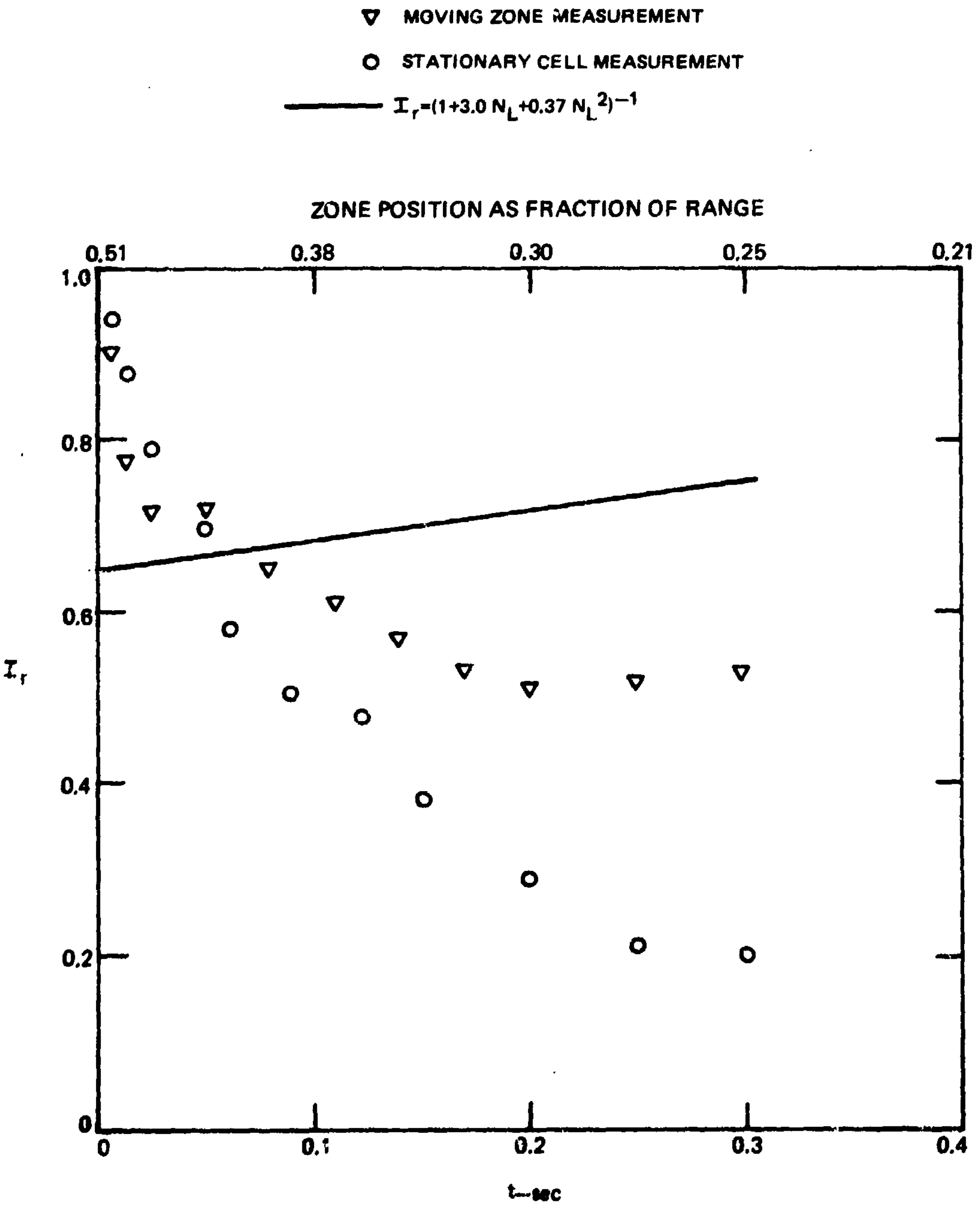

77–04–37–2

MOVING STAGNATION ZONE DATA RECORDS—INTENSITY VS TIME

F=4.3

$\dot{x}_o=-3.9$ cm/sec

$a\ell=0.21$

a) P=5.6W
b) P=11.5W
c) P=16W

0.5 V/cm

$a\ell=0.45$

d) P=5.6W
e) P=11.5W
f) P=16W

0.05 V/cm

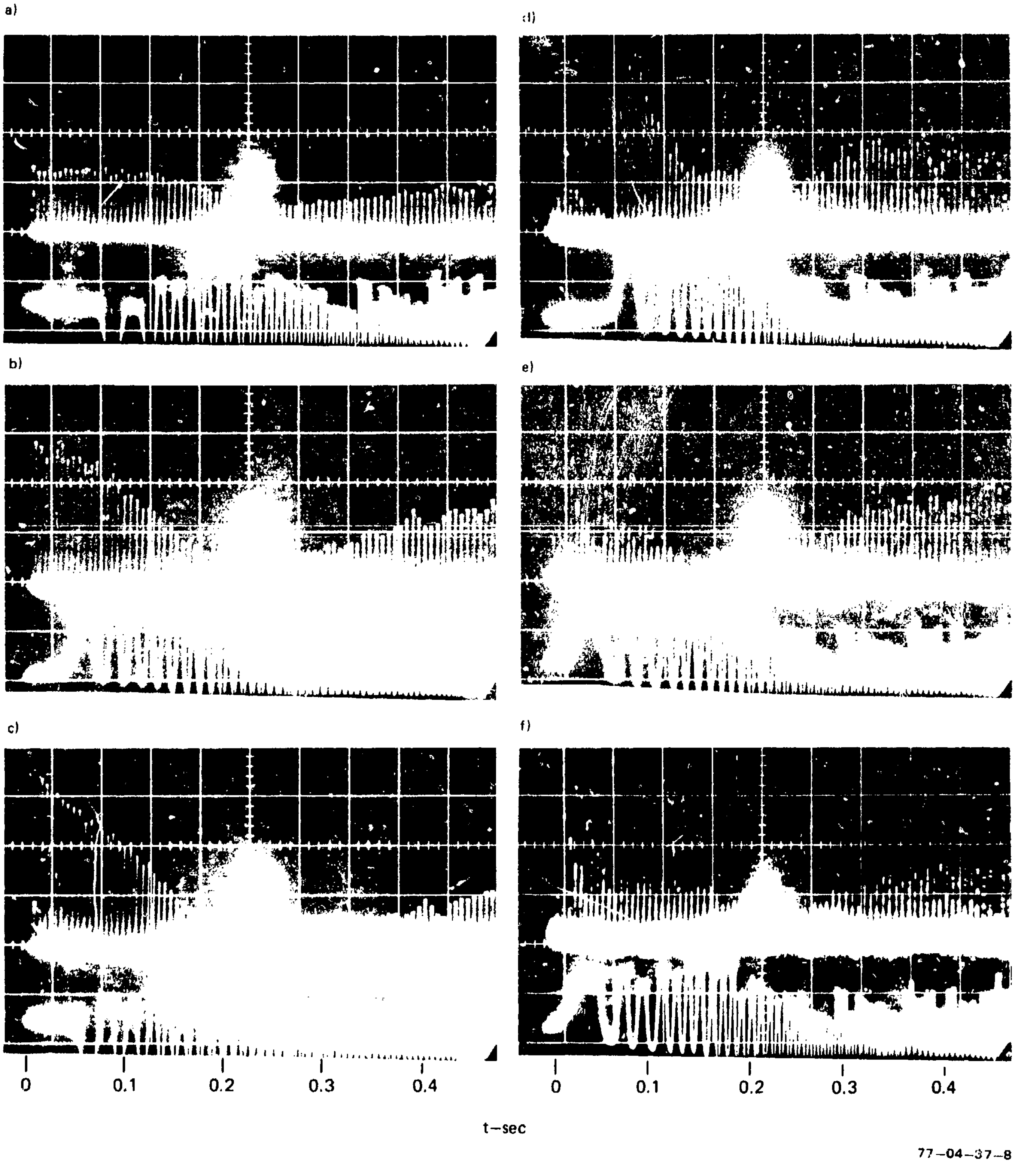

77–04–37–8

MOVING STAGNATION ZONE EXPERIMENTAL RESULTS—$I_r(t)$ VS N_L

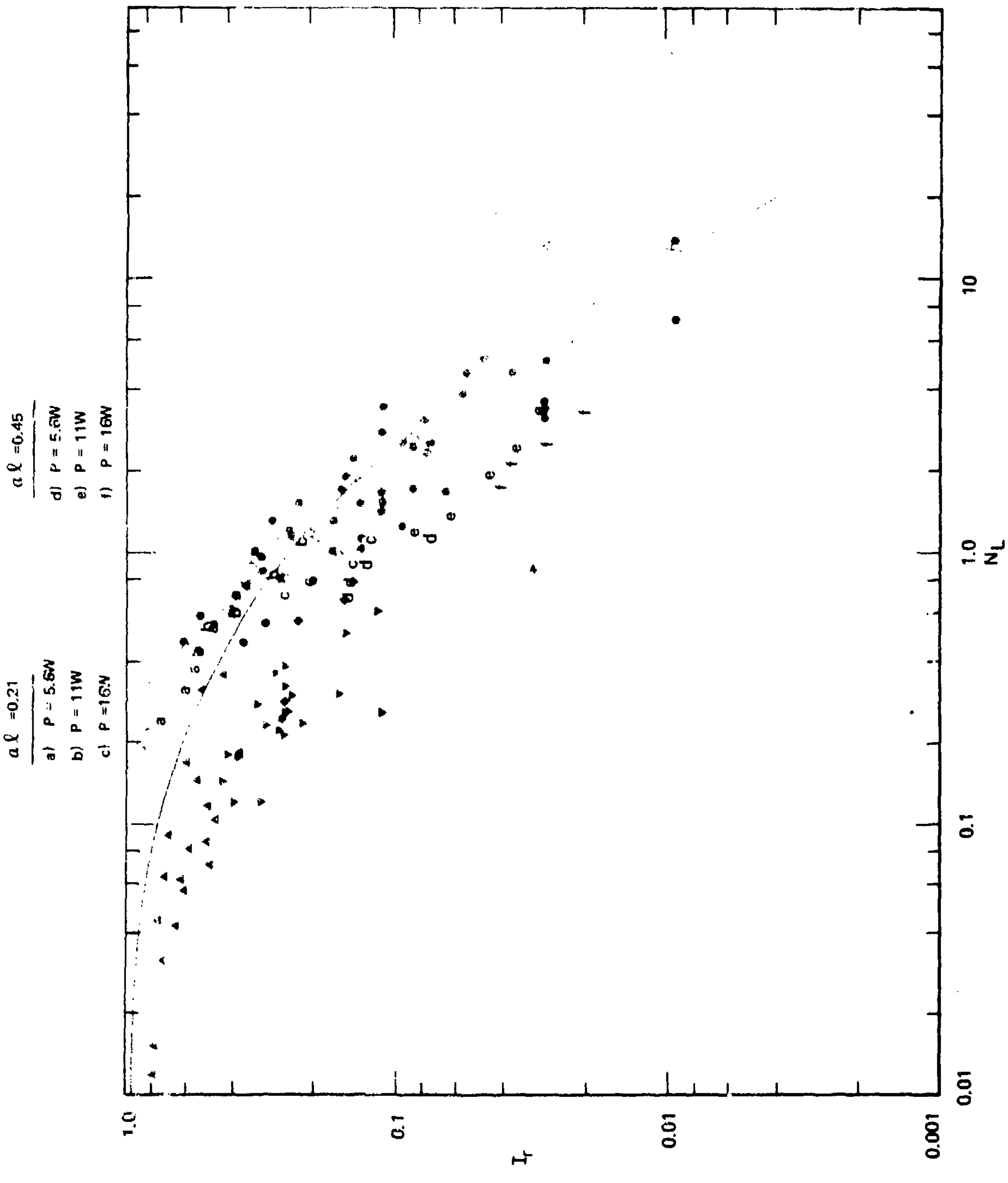

77-04-37-10

t_{ss} vs. $4a(z')/z_f\omega$

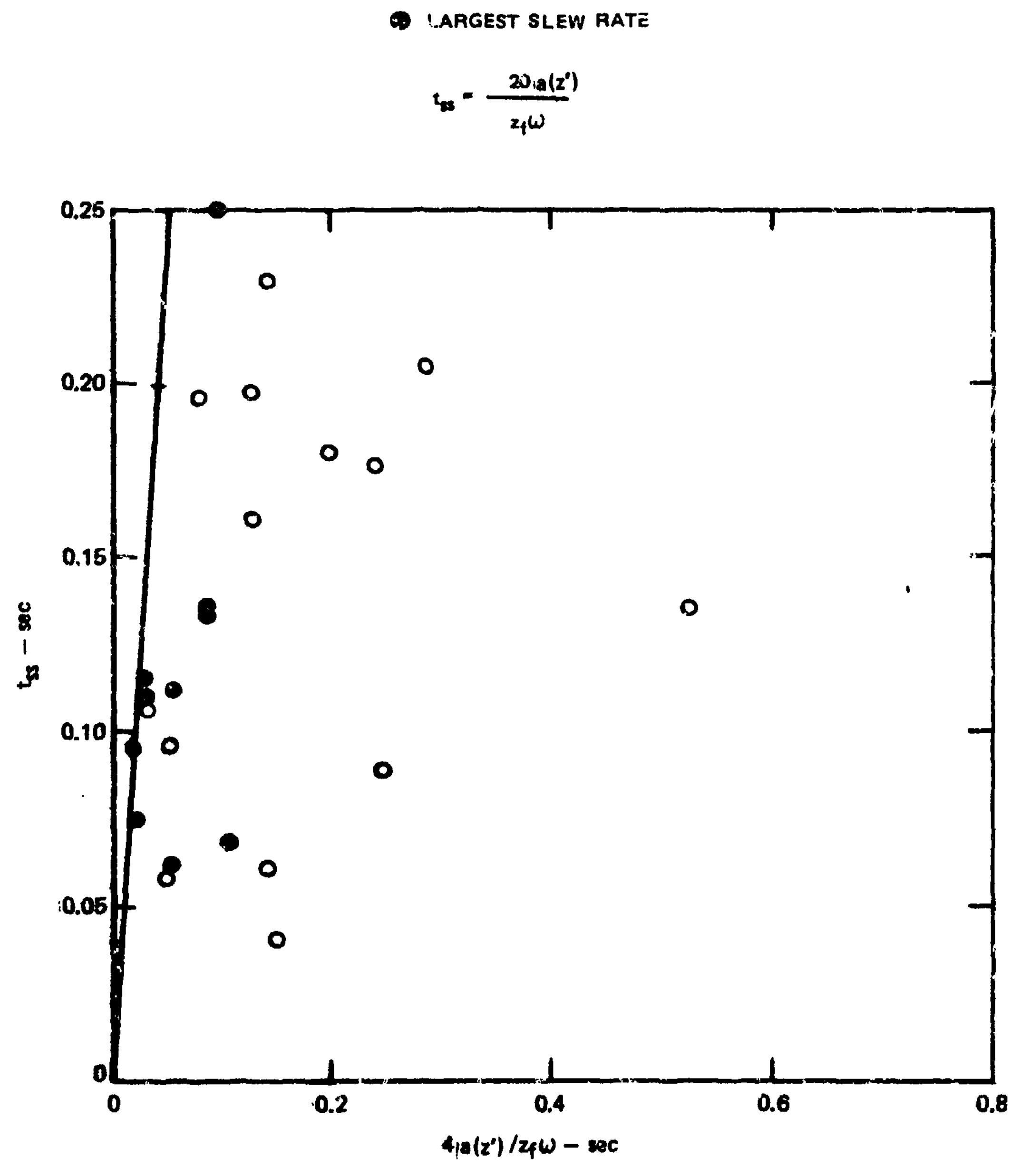

77-06-138-1

$t_{ss} z_f \omega / a(z')$ vs. z'/z_f

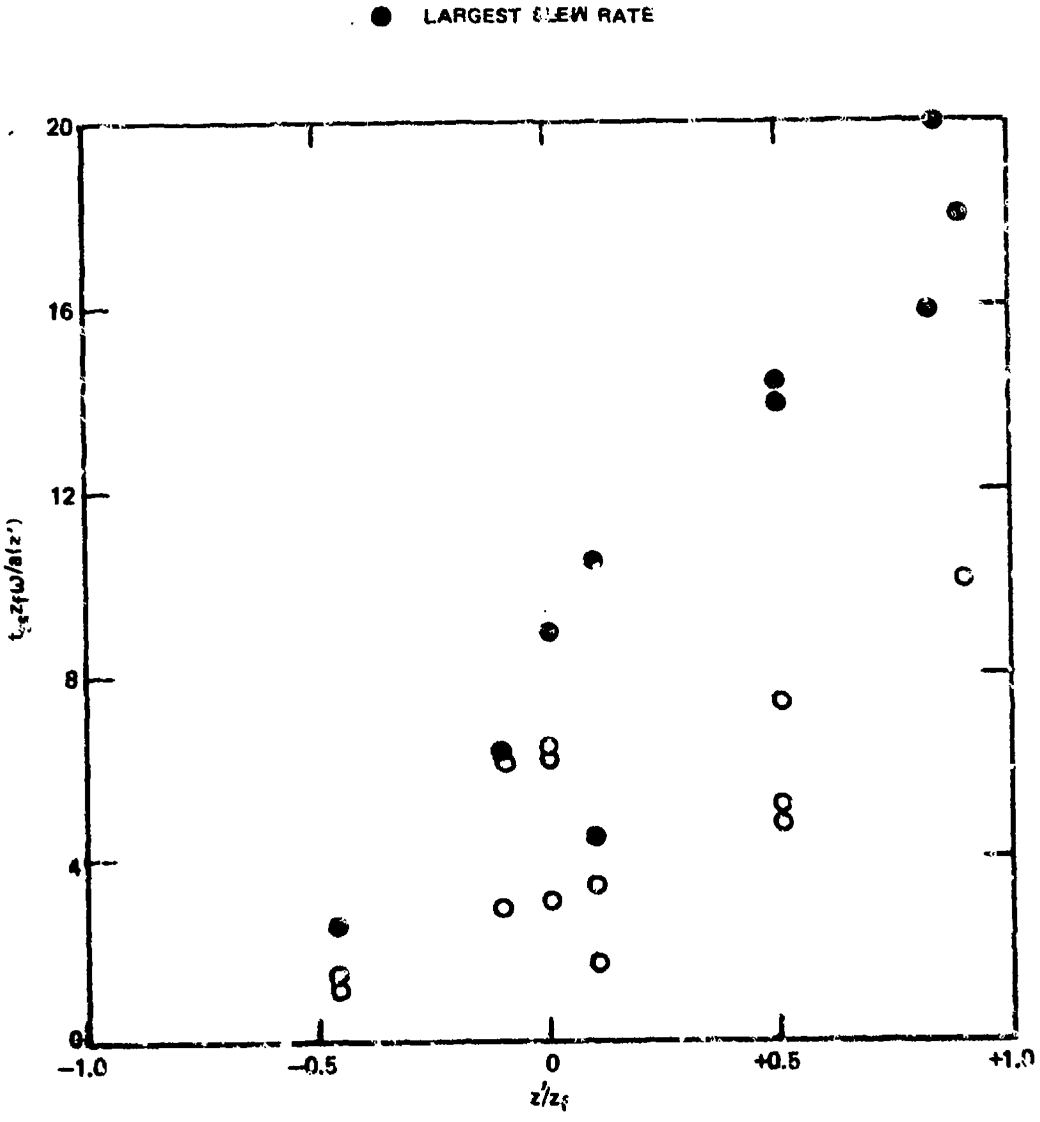

77–06–138–3

$t_{ss}\, z_f \omega / a_0$ vs. z'/z_f

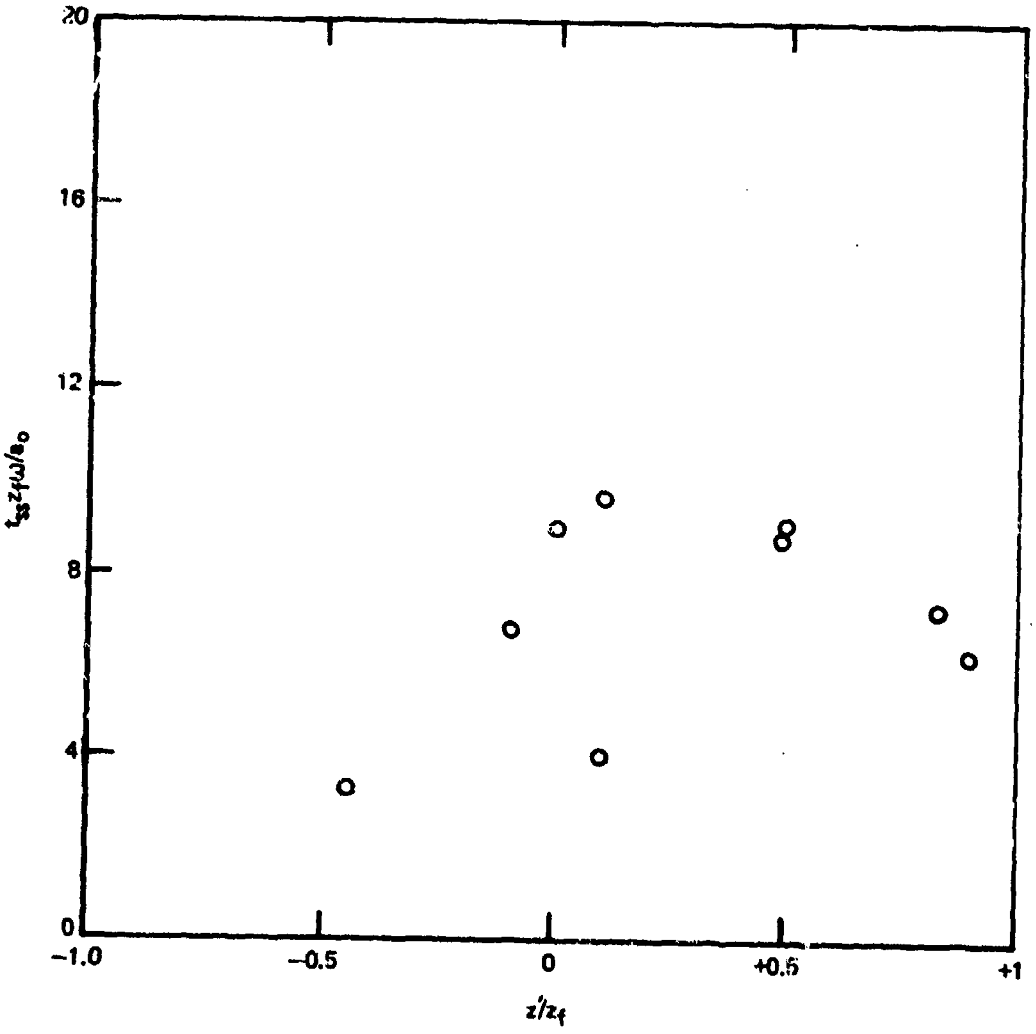

t_{ss} vs. $4a_o/z_f\omega$

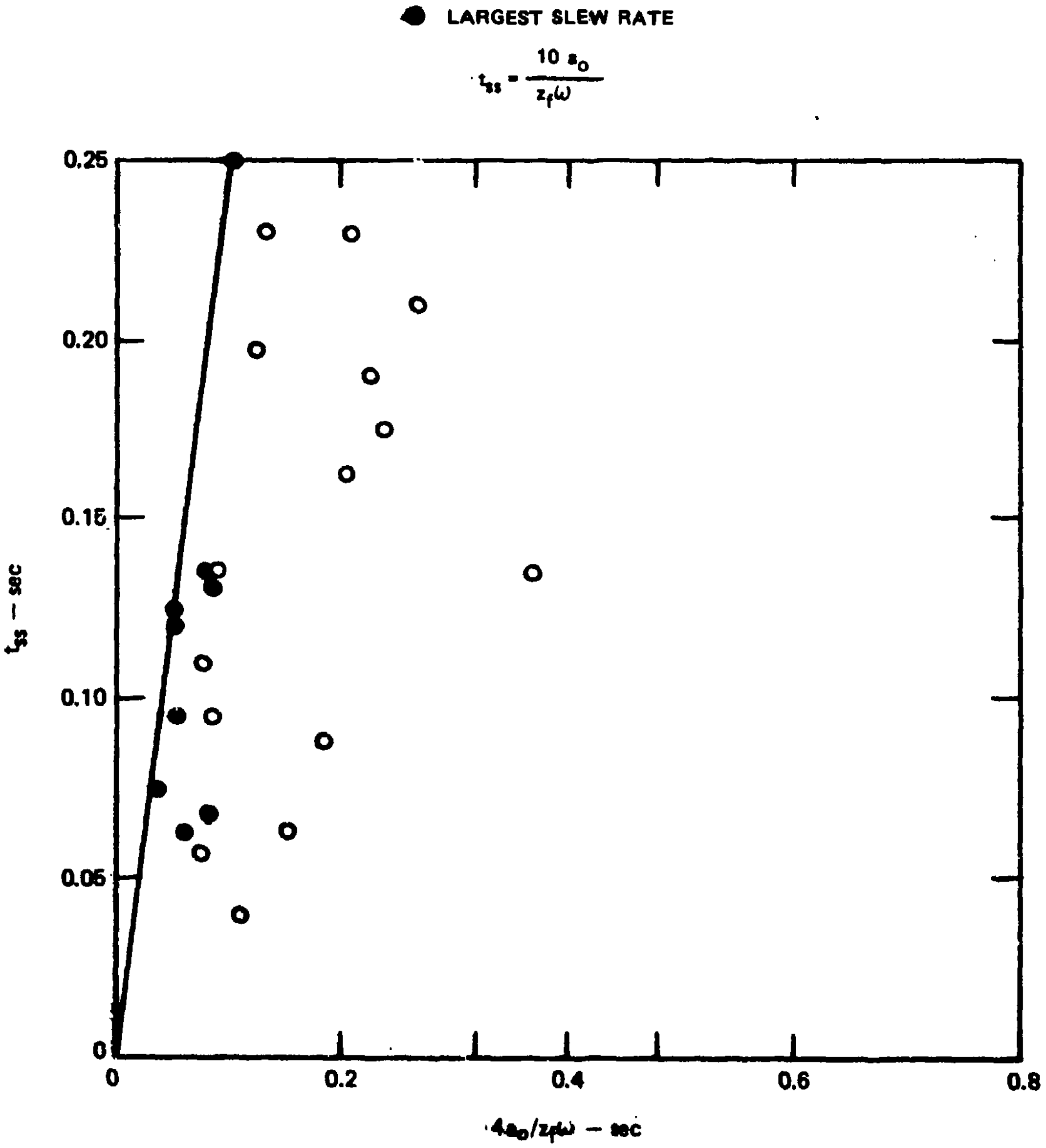

77-06-138-4

KINEMATIC DEPENDENCE OF Ψ*

$x_o = -4.0$cm/sec

$s_o = 0.36$

10 ATMOSPHERES N_L

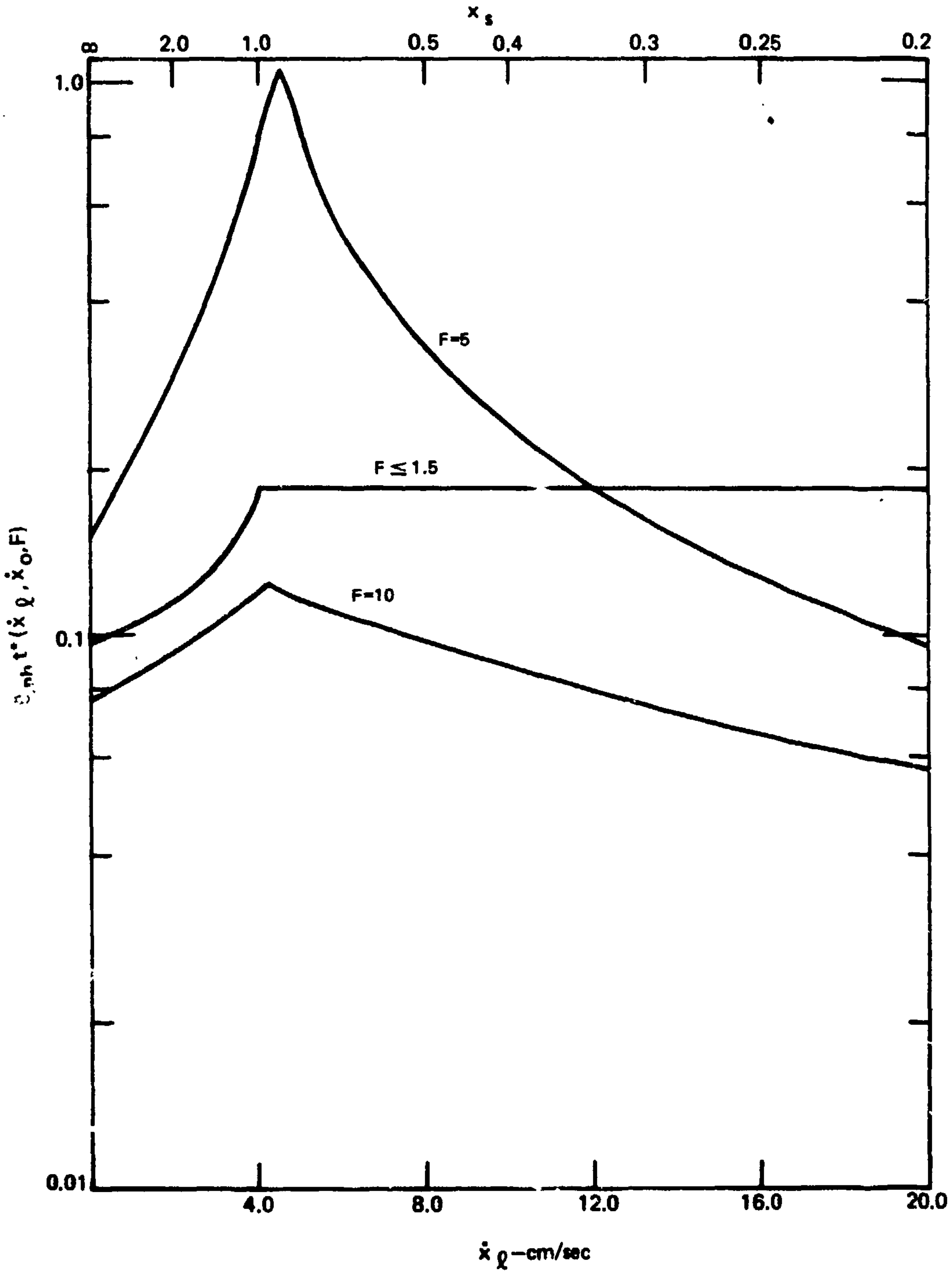

77–04–37–1

STATIONARY STAGNATION ZONE RESULTS VS Ψ

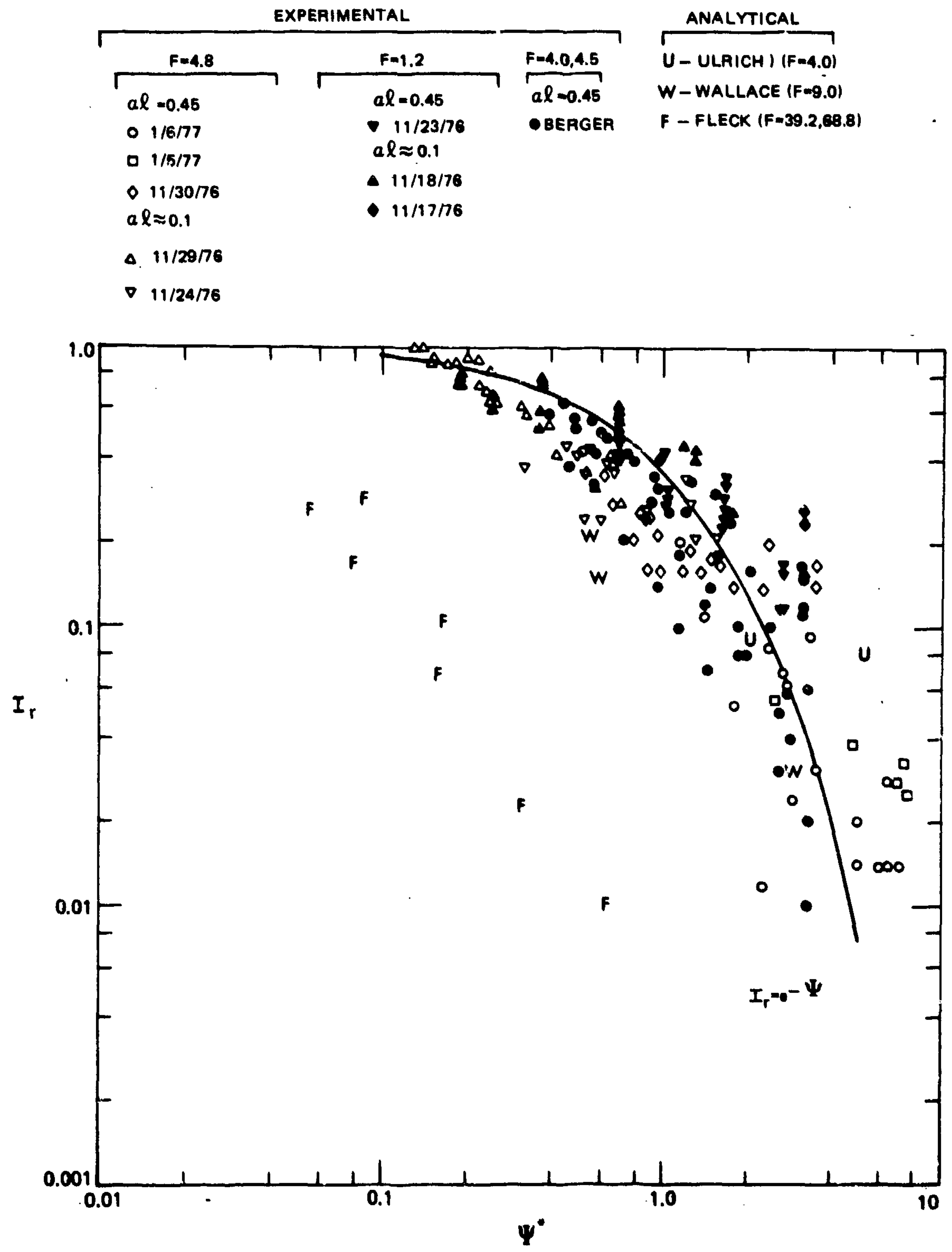

77–04–37–9

MOVING STAGNATION ZONE EXPERIMENTAL RESULTS—$I_r(t)$ VS Ψ^*

F=4.3

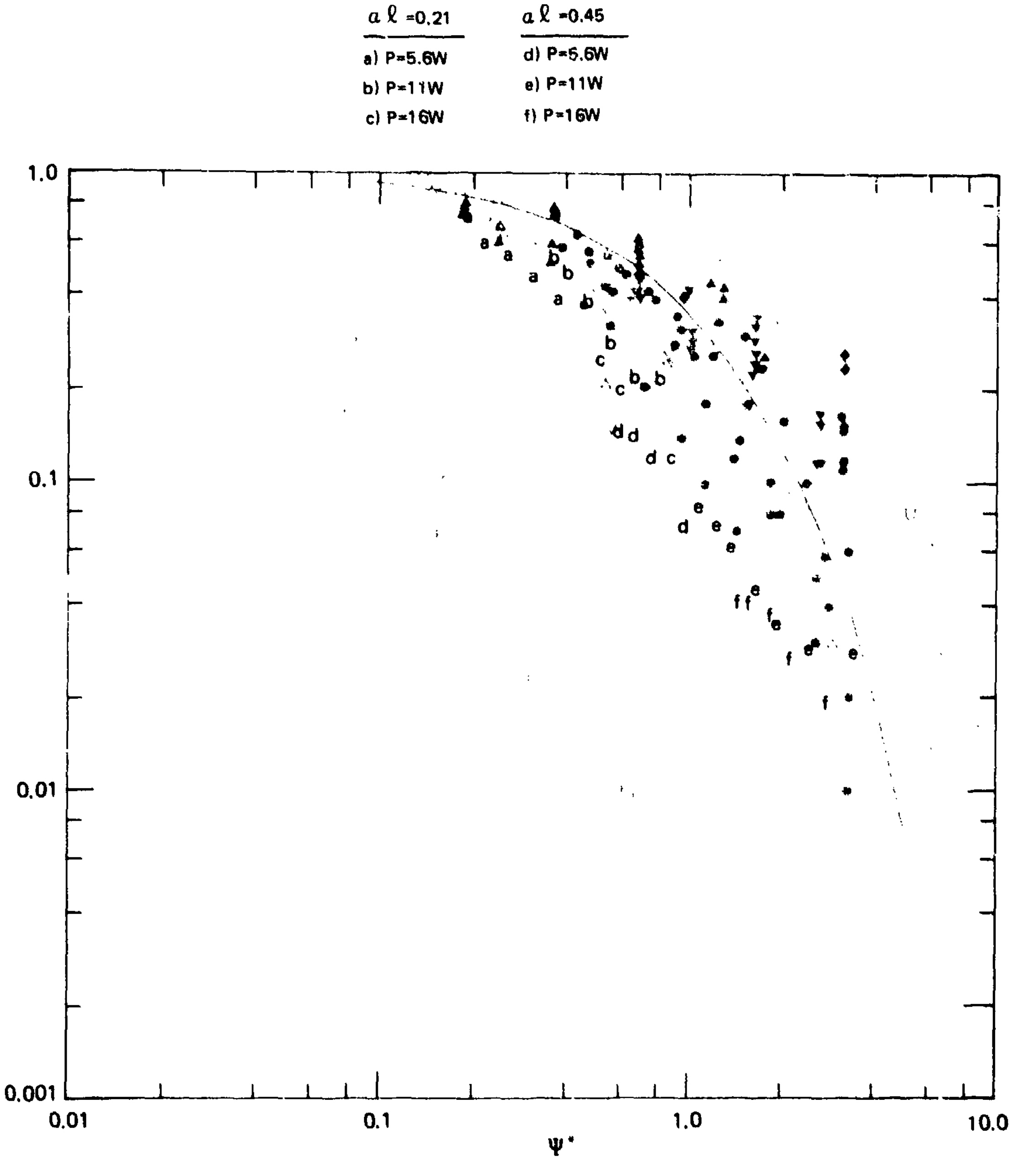

AEROSOL EFFECTS ON CO_2 LASER PROPAGATION

SECTION BI

INTRODUCTION

Understanding the propagation characteristics of high power CW laser beams through an aerosol ladened medium is important for Navy applications of lasers for two basic reasons. First, if the laser is operating at a middle infrared wavelength for which there is an atmospheric window, the effective absorption coefficient of suspended aerosol can dominate over the ambient molecular absorption coefficient [1,2] and second is the problem of propagation through fog. When these situations arise, thermal distortion of the high power beam must be calculated from a theory based on the absorption coefficient of the aerosols. It has been demonstrated experimentally[3,4] and theoretically[5] for the steady state, CW case that the propagation models of molecular induced thermal blooming were applicable to the aerosol case by merely replacing the gas absorption coefficient with that indicative of the suspended aerosols. This modeling is adequate for particles that cannot be vaporized by the high power beam. The other aerosol propagation problem, i.e., when vaporization occurs, has not been understood as well. This second important aerosol propagation condition exists when the target is shrouded by fog. The detrimental effects of fog are of concern whether the laser device is operating in the middle infrared region or at longer wavelengths such as 10.6 microns. The thermodynamics of the fog droplets have been studied [6,7] and some of the propagation effects have been investigated,[8,9] but this work typically neglects the problem of thermal blooming. Furthermore, early attempts to experimentally measure fog induced thermal blooming[10] failed to provide measurable distortion, presumably due to high transverse velocities that could not be alleviated. Therefore, the goal of this research program was envisioned as filling this information gap by operating a high power laser in a scaled regime where fog induced thermal blooming could be measured and analyzed. We have accomplished this goal.

Another important goal of this research program was to operate the fog induced thermal blooming experiments in a parametric arrangement that was a scaled subset of conditions that might be encountered during a full-scale field situation. To achieve this goal we have utilized a multi-kilowatt, CW CO_2 laser to provide intensity levels similar to those anticipated for field conditions. In addition, the beam was translated through the fog cell to simulate a uniform wind transverse to the trajectory. In the propagation cell, a very concentrated, artificially-generated fog was used to model natural fog conditions over long atmospheric paths, while maintaining a droplet size similar to natural conditions. The parameters of the scaled experiment are compared with approximate field conditions in Table B-I. The entire range of parameters used during the experiments is listed in Table B-II.

This report summarizes our efforts to measure fog induced thermal distortion during the conditions discussed above (Section BIII) and to model the physics of the interaction between high power beam and a medium shrouded in fog (Section BII). Computer codes for thermal distortion in a saturable absorber and for Mie scattering functions were developed under United Technologies Corporate IR&D funds in support of this research.

SECTION BII

THEORETICAL MODELING

A. INTRODUCTION

This section reviews the basic effects of a water droplet on propagation at 10.6 microns. The effects are discussed in terms of the extinction coefficient, the absorption coefficient and the scattering coefficient. Pertinent examples of Mie calculations are included. Furthermore, we introduce the decay of the water droplet as a consequence of high power laser irradiation. For conditions when droplet vaporization is significant, we model the fog as a saturable absorber. The saturable, fog absorber model has subsequently been included in our CW thermal blooming computer code. The ensuing results of reduced thermal blooming and enhanced power transmission are examined in a limited sensitivity study of the code predictions. Finally, with the goal of an empirical model in mind, we indicate an approach to simplified scaling.

B. PROPAGATION THROUGH NONVOLATILE AEROSOLS

The irradiance loss on target for linear propagation is given by

$$\frac{I}{I_0} = e^{-\int_0^L \alpha_{ext}(z)dz} \qquad \text{(B-1)}$$

where L is the pathlength through a fog of extinction coefficient α_{ext}. It is assumed that the beam exerts no modifying influence on the fog droplets. If the fog is uniform and homogeneous then one may write Eq. (B-1) simply as

$$\frac{I}{I_0} = e^{-\alpha_{ext}L} \qquad \text{(B-2)}$$

The extinction coefficient is given by

$$\alpha_{ext} = \int_0^\infty \pi r^2 Q_{ext}(r) N(r) dr \qquad \text{(B-3)}$$

in which Q_{ext} is the extinction efficiency for droplets of radius r with a size distribution N(r). For a monodisperse droplet population Eq. (B-3) is

$$a_{ext} = \pi r^2 Q_{ext}(r) C \tag{B-4}$$

where C is the concentration of fog droplets per unit volume.

In this development it is important to identify two mechanisms responsible for intensity loss during the aerosol propagation problem. These are absorption and scattering, such that

$$Q_{ext}(r) = Q_{abs}(r) + Q_{sca}(r) \tag{B-5}$$

The scattering coefficient has no bearing on thermal distortion considerations except with respect to a general intensity loss as the beam propagates to the target. However, the absorption coefficient is directly responsible for transferring energy from the laser beam to heating of the ambient gas. These induced temperature changes in the gas can cause severe beam distortion and are the result of nonlinear propagation effects.

Now, if one is concerned with nonlinear propagation effects and assumes that the droplets remain unmodified by the propagating beam, the amount of thermal blooming is conveniently modeled by the peak target irradiance relative to the undistorted value. The empirical expression[2] for the reduced target irradiance (considering only thermal distortion) is

$$I_{rel} = \frac{I}{I_0 e^{-a_{abs}L}} = \frac{1}{1 + \left(\frac{N_f}{4}\right)^2} \tag{B-6}$$

where

$$N_f = \frac{-\eta_T a_{abs} PL^2}{\pi n \rho C_p v a^3} f(a_{abs}L) q(a) \tag{B-7}$$

The basic parameters are defined as

n_T = index change per unit temperature

P = laser power

n = unperturbed index of refraction

ρ = ambient gas density

C_p = ambient gas heat capacity

v = transverse wind velocity

a = 1/e intensity radius

In Eq. (B-7) $f(a_{abs}L)$ and $q(a)$ are correction factors for large absorption coefficients (and/or long path lengths) and strong focussing:

$$f(\alpha_{abs}L) = \frac{2}{(\alpha_{abs}L)^2}\left[\alpha_{abs}L - 1 + e^{-\alpha_{abs}L}\right] \qquad \text{(B-8)}$$

$$q(a) = \frac{2F^2}{(F-1)}\left[1 - \frac{\ln F}{(F-1)}\right] \qquad \text{(B-9)}$$

F is the Fresnel number. Note in this development that the absorption coefficient (assuming negligible background molecular absorption) must be representative of the fog droplets,

$$\alpha_{abs} = \pi r^2 Q_{abs}(r)\,C \qquad \text{(B-10)}$$

Therefore, a fundamental part of the linear/nonlinear fog propagation problem consists of identifying the absorption and scattering efficiencies of the droplet constituents at the wavelength of interest.

A Mie scattering[12] computer program[13] has been developed at UTRC and was utilized to provide the necessary efficiency factors. This program calculates the angular scattering function for a droplet of given size. Two examples are given in Fig. B-1. These curves are for polarization perpendicular to the plane of incidence. In the case of the 0.5 μm radius droplet we observe nearly perfect Rayleigh scattering[12] while in the 5 μm radius case the angular function has developed more structure. This angular scattering function is integrated over all angles to derive the total scattering efficiency for a droplet radius. The absorption efficiency is also calculated. Figure B-2 gives the ratio of the absorption and scattering efficiencies for droplet sizes in the range of interest for this project. Furthermore, the absolute absorption efficiency is illustrated in Fig. B-3. The calculations illustrated in Figs. B-2 and B-3 can be used to estimate the severity of the linear and nonlinear propagation problems through a nonvolatile fog.

The parameters for a full-scale propagation example in light fog[14] are listed in Table B-III. The target irradiance losses are substantial with the effect of fog induced thermal blooming being most severe. In contrast, only nominal losses are suffered for the clear atmosphere. In summary, this example alone serves as sufficient justification for concern over the degrading effects that occur during foggy conditions.

Note that this discussion was based on the assumption that the fog was not modified by the laser beam. In reality a fog droplet is very volatile and under certain conditions a sufficiently powerful laser may destroy a large portion of the droplet population. In this situation the outlook for high power propagation is not nearly as bleak. The theoretical results for propagation in actively modified fog are discussed in the next section.

C. PROPAGATION THROUGH ACTIVELY MODIFIED FOG

Figure B-4 presents the calculated decay of a 10 μm fog droplet irradiated by a high power beam. In this illustration the droplet enters a uniform 5 kW beam with a 1.5 cm radius. A scaled wind of 15 cm/s is blowing transverse to the trajectory. By the time the droplet has reached the beam axis it has disappeared. The importance of the droplet lifetime problem is compounded when Eqs. (B-4) and (B-10) are recalled in which the extinction and absorption coefficients are a strong function of the fog droplet size. As a consequence, models for power transmission and thermal distortion must be appropriately modified to reflect the influence of the decaying droplets. In this section we address such a modification with an initial discussion of the droplet thermodynamics.

Many references[6,9,15] give the rate equation for a vaporizing droplet

$$\frac{d(4/3\,\pi r^3 \rho H_v)}{dt} - 4\pi r^2 K_a \frac{dT(r)}{dr} = I\alpha_{abs} \qquad \text{(B-11)}$$

In this development it is assumed that the droplets are not vaporized fast enough to force the velocity of the escaping vapor to exceed the acoustic velocity[6]. In addition, Mullaney, et al[9] show that the solution to this equation may be written as

$$r(t,I) = r_i e^{-\Delta t/\tau(I)} \qquad \text{(B-12)}$$

where

$$\tau(I) = \frac{3\rho H_v}{I\alpha_B}\left[1 + \frac{K_a R^2 T^3(r)}{D H_v^2 w^2 P_{wv}(r)}\right] \qquad \text{(B-13)}$$

for

α_B = bulk absorption coefficient of H_2O

K_a = thermal conductivity of air

R = gas constant

$T(r)$ = temperature at drop surface

H_v = H_2O heat of vaporization

D = diffusivity of H_2O vapor in air

w = molecular weight of H_2O

$P_{wv}(r)$ = partial pressure of water vapor at $T(r)$

From Ref. 6 we find that for conditions of interest $T(r) \approx$ ambient, an approximation good to about 10 percent. Hence, $P_{wv}(r)$ is the vapor pressure of the saturated solution at the ambient temperature. For the following constant values

$$\alpha_B = 9.48 \times 10^{2} \text{ cm}^{-1}$$

$$\rho = 1 \text{ g/cm}^{3}$$

$$H_v = 2448 \text{ J/gm}$$

$$K_a = 2.55 \times 10^{-4} \text{ J/cmSecoC}$$

$$R = 8.318 \text{ J/}^{o}\text{K mole}$$

$$T = 293^{o}\text{K}$$

$$D = 2.4 \times 10^{-1} \text{ cm}^{2}\text{/sec}$$

$$w = 18 \text{ gm/mole}$$

$$P_{wv}(293) = 23.4 \text{ mb}$$

$\tau I \approx 11$ J/cm^2 with I in w/cm^2, so we rewrite Eq. (B-12) as

$$r(t,I) = r_i e^{-\Delta tI/11} \qquad \text{(B-14)}$$

In general, we expect Eq. (B-14) to be a reasonable solution to Eq. (B-11) for droplets with radii less than about 10 µm.

Furthermore, we have performed a linear regression analysis of Q_{abs} as a function r(cm) and find

$$Q_{abs}(r) = (1.18 \times 10^{3})\, r + 4.87 \times 10^{-3} \qquad \text{(B-15)}$$

The correlation coefficient for this fit to the Mie calculated values is better than 99 percent for $r = 10^{-4}$ to 10^{-3} cm. We may further simplify this expression (error less than 10 percent in range of interest) to

$$Q_{obs}(r) = (1.18 \times 10^{3})\, r \qquad \text{(B-16)}$$

Combining Eqs. (B-16), (B-14) and (B-10)

$$\alpha_{obs}(t,I) = (1.18 \times 10^{3})\, \pi C r_i^{3} e^{-3\Delta t I/H} \qquad \text{(B-17)}$$

It is then obvious that α will depend on a droplets initial size and the total time it has been illuminated by the high power beam. Since I may be a function of position, and the medium is moving with velocity v, we may rewrite Eq. (B-17) as

$$\alpha_{obs}(x) = (1.18 \times 10^{3})\, \pi C r_i^{3} e^{-\frac{3}{HV}\int_{-\infty}^{x} I(x'')dx''} \qquad \text{(B-18)}$$

upon considering only the plane of the beam containing the wind vector. Now, Gebhardt and Smith[16] show the perturbation in the ambient gas temperature is

$$\Delta T(x) = \frac{1}{\rho C_p v}\int_{-\infty}^{x} I(x')\, \alpha_{obs}(x')\, dx' \qquad \text{(B-19)}$$

At this point we must acknowledge that a significant portion of the energy is lost to the vaporization mechanism and cannot be conducted to the gas. That is

$$\Delta T(x) = \left[\frac{1}{\rho C p v}\int_{-\infty}^{x} I(x')\,\alpha(x')\,dx'\right]\epsilon \tag{B-20}$$

where ε is the fraction of absorbed heat that is conducted to the gas from the droplet. ε is just[6]

$$\epsilon = \frac{K_0 R^2 T^3(r)}{D H_v^2 w^2 P_{wv}(r)} \tag{B-21}$$

which has a value between 0.3 and 0.4. We will use 0.33. Finally

$$\Delta T(x) = \frac{(0.33)(1.18\times10^{3})\pi C r_i^3}{\rho C p v}\int_{-\infty}^{x} I(x')\,e^{-\frac{3}{11V}\int_{\infty}^{x'} I(x'')dx''}\,dx' \tag{B-22}$$

where T(x) is the one-dimensional perturbation temperature of the ambient gas when the fog is subject to vaporization. If we normalize this temperature change by that experienced for no induced droplet vaporization Eq. (B-22) becomes

$$\frac{\Delta T}{\Delta T_0}(x) = \frac{\int_{-\infty}^{x} I(x')\,e^{-\frac{3}{11V}\int_{-\infty}^{x'} I(x'')dx''}\,dx'}{\int_{-\infty}^{x} I(x')dx'} \tag{B-23}$$

The importance of Eqs. (B-22) and (B-23) can be illustrated by considering a uniform transmitter illumination function. Equation B-22 becomes

$$\Delta T(x) = \frac{(9.05\times 10^{3})\pi C r_i^{3}}{\rho C_p}\left[1 - e^{-\frac{3I_0 x}{11v}}\right] \qquad \text{(B-24)}$$

where I_o is the laser intensity and x is the position in the beam cross section along the direction of the wind. Furthermore, Eq. (B-23) becomes

$$\frac{\Delta T}{\Delta T_0}(x) = \frac{11v}{3I_0}\left[\frac{1}{x}\left(1 - e^{-\frac{3I_0 x}{11v}}\right)\right] \qquad \text{(B-25)}$$

The above equations indicate that the maximum temperature perturbations may be severely limited due to the saturable absorber. The significance of this effect is displayed in Fig. 5 where we have graphed the relative ambient temperature rise for a nonsaturable and a saturable absorber. This example shows that the on-axis temperature perturbation for the saturable fog absorber is only about 14 percent of that for a nonvolatile absorber (or molecular absorber). Even more important is the fact that the perturbed temperature gradients are also drastically limited. This condition implies reduced thermal distortion of the laser beams spatial intensity distribution.

The expressions corresponding to Eqs. (B-24) and (B-25) for a Gaussian illumination function are

$$\Delta T(x) = \frac{(0.33)(1.18\times 10^{3})\pi r_i^{3} I_0}{\rho C_p v}\int_{-\infty}^{x} e^{-\frac{x'^2}{a^2}}\, e^{-\left(\frac{3I_0}{11v}\right)\left(\frac{a\sqrt{\pi}}{2}\right)\left[1+\mathrm{erf}(x'/a)\right]}\,dx' \qquad \text{(B-26)}$$

and

$$\frac{\Delta T}{\Delta T_0}(x) = \frac{\int_{-\infty}^{x} e^{-\frac{x'^2}{a^2}} e^{-\left(\frac{3I_0}{11v}\right)\left(\frac{a\sqrt{\pi}}{2}\right)\left[1+\mathrm{erf}(x'/a)\right]} dx'}{\frac{a\sqrt{\pi}}{2}\left[1+\mathrm{erf}(x/a)\right]} \qquad \text{(B-27)}$$

where I_0 is the peak intensity for a beam with e^{-1} radius of a.

In conclusion, these modified temperature perturbations can be used in a thermal blooming code to calculate the resulting distortion of a high power beam and to study the importance of the saturable absorber.

D. PROPAGATION CODE WITH SATURABLE FOG ABSORBER

The saturable fog absorber model has been incorporated into a CW thermal blooming code[17]. The modified code takes the initial fog droplet size and concentration and uses Mie calculations to develop the appropriate extinction and absorption coefficients. The beam then propagates through one incremental step toward the target, forcing droplet evaporation. The phase changes due to index perturbations from the fog induced temperature perturbations are identified and utilized as initial information for the next Z step. The background molecular absorption coefficient is also accounted for. In addition, the extinction from the modified fog is calculated such that the initial intensity for the subsequent Z step is appropriately modified. Calculations over the beam cross-section are performed on a rectangular mesh that is adapted to the convergence of the focused beam, and the incremental Z stepping toward the target is actively adjusted to keep the accumulated distortion per step very small. The general calculational procedures are similar to other nonlinear propagation codes[18].

An example of the output graphics from the code is given in Fig. B-6. Shown for typical experimental conditions are the phase distribution, intensity distribution, transverse intensity profile and the integrated intensity in the target plane. This particular example is for 0.5 kW, and thermal distortion of the intensity distribution is evidenced as is a large total power loss via extinction. When the power is increased to 4.0 kW, Fig. B-7 shows that thermal blooming decreases and the overall relative transmission to the target plane has increased substantially. In an attempt to understand the scaling of these effects, we have looked at some code runs in a more comprehensive fashion.

To date the new propagation code has been exercised over a limited range of parameters. For instance, we have performed a sensitivity study study of parametric variations on the nominal thermal blooming conditions of one case from the experimental data runs to be discussed in Section BIII. In this study we have investigated I_{rel} (from Eq. (B-6)) as a function of the distortion parameter N_f, when N_f is determined by the absorption coefficient of the unmodified fog. The result is presented in Fig. B-8. Table B-IV reviews the range of parameter variations. As P and v are adjusted providing different "burn-through" capabilities, the breakdown of the classical thermal blooming model Eq. (B-6) becomes very apparent. Additionally, the value of N_f shows a sensitivity to variations in the droplet radius. This is due to the strong dependence of the absorption coefficient on r (Eq. (B-10). However, I_{rel} does not appear to be very sensitive to the small adjustments of r. Both I_{rel} and N_f show a much weaker dependence on the fog concentration. The results of a small variation in C reside between the indicated points ($\overset{1}{\Delta}$ and $\overset{2}{\Delta}$) along the "P-variable" line.

The enhancement of high power propagation through the saturable fog (and breakdown of the classical model) can be explained as occurring from two effects. First of all, the saturable absorber permits only limited temperature perturbations to be produced in the ambient gas. This results in reduced spatial distortion of the beam. The second enhancement mechanism is simply that of droplet destruction; consequently the steady state effective absorption coefficient is significantly reduced. As a result, overall transmission increases in addition to the inhibition of spatial distortion. In the data, these effects may be separated by analyzing the target intensity from two additional points of view. We suggest that the effects of reduced spatial distortion may be understood by investigating the area of the bloomed beam normalized by that of the undistorted beam at the 1/e intensity contour. Furthermore, the mechanism of enhanced transmission may be analyzed by studying the total power delivered to the target plane through the 1/e intensity contour for the distorted case compared to the undistorted case. These parameters will be defined as A_{rel} and P_{rel}.

The A_{rel} results are summarized in Fig. B-9. In this example we have maintained N_f as the abscissa, but do so recognizing that N_f may not be a good parameter for the scaling of actively modified fog results. The calculations show that as P increases or v decreases the fog is more effectively destroyed, and the amount of spatial beam distortion is dramatically reduced relative to the classical model. On the other hand, if P and v are fixed and the droplet radius or the droplet concentration is adjusted. then the amount of thermally induced distortion seems to have the same slope or functional dependence on N_f as the gas model but with a significantly lower magnitude.

Figure B-10 illustrates P_{rel} as a function of the initially unmodified fog $\alpha_{ext}L$. Large increases in transmission are predicted for either increased power or decreased wind velocity. Also, Eq. (B-2) seems to still be valid in the modified fog examples for fixed P and v with variable r or C, but a new effective extinction coefficient must be identified. In essence, this implies that a 10.6 μm transmission through the modified fog remains a relatively simple function of the total remaining liquid water content in the trajectory[14]. These code data suggest that some simplified scaling may be possible for the nonlinear, fog propagation problem.

E. SCALING AND A MODIFIED EMPIRICAL MODEL

A reasonable engineering approximation to the code results illustrated in Fig. B-10 may be developed by realizing that for the droplet size range of interest the extinction coefficient is approximately equal to the absorption coefficient. With this assumption we may utilize Eq. (B-17) to write

$$\alpha_{ext} = \alpha_{ext_{initial}} \, e^{-\frac{3}{11v}\int_{-\infty}^{x} I(x')dx'} \qquad \text{(B-28)}$$

which becomes

$$\alpha_{ext} = \alpha_{ext_{initial}} \, e^{-\left(\frac{3P}{22\sqrt{\pi}\,va}\right)\left[1 + \mathrm{erf}(x/a)\right]} \qquad \text{(B-29)}$$

For simplicity, we will choose to calculate the scaling at beam center where $x = 0$ and include a fitting parameter D such that

$$\alpha_{ext} = \alpha_{ext_{initial}} \, e^{-D(0.0769)\frac{P}{\sqrt{a}}} \qquad \text{(B-30)}$$

We select a value of $D = 0.437$ to provide a good empirical fit between the code data and the simplified formulation of Eq. (B-30) (one should note that this fitting constant will change depending on the illumination function and the Fresnel number of the beam). Equation (B-30) becomes

$$\alpha_{ext} = \alpha_{ext_{initial}} \, e^{-(0.0336)\frac{P}{\sqrt{a}}} \qquad \text{(B-31)}$$

When this modified extinction coefficient is used in

$$P_{rel} = e^{-\alpha_{ext} L} \qquad \text{(B-32)}$$

the simplified model agrees to better than 10 percent with all but one of our code sensitivity results. At one low power (0.5 kW) case where burn-through was not very effective the agreement dropped to 17 percent.

Now, since $\alpha_{abs} \approx \alpha_{ext}$ we may estimate a new effective absorption coefficient to be used in calculating N_f and I_{rel} of the empirical model. In other words

$$\alpha_{\substack{\text{thermal}\\\text{blooming}}} \cong \alpha_{\substack{\text{abs}\\\text{initial}}} \, e^{-(0.0336)\frac{P}{va}} \tag{B-33}$$

The results of Fig. B-11 occur when Eq. (B-33) is used to calculate a new N_f for the computed values of A_{rel} in Fig. B-9. This evidence implies that the parametric modeling by Eqs. (B-6) and (B-7) remains valid and that if the appropriate modified absorption coefficient is known within the beam, then the thermal distortion occurs as derived for the molecular absorption theories. The one point where our simplified scaling has not worked well was for large P/va (> 100). In this case the simplified model predicted a lower A_{rel} than calculated by the computer code. Our work indicates that during these conditions of large P/va the simple exponential law of Eq. (B-28) must be generalized to include an integration along the trajectory. In such a case scaling will become more complicated.

F. LIMITATIONS OF THE SIMPLIFIED MODEL

The analysis of the computer calculations discussed in this section represents only a limited sensitivity study, and therefore does not investigate all limits of the simplified scaling, e.g., very large P/va. Furthermore, the illumination function was assumed to be Gaussian with a fixed Fresnel number. A change of either of these geometric parameters will affect a change in the constants of the scaling equations. Finally, the assumptions that $\lambda = 10.6$ μm and $r = 2 - 3$ μm simplified the calculation of Q_{abs} and Q_{ext}. For large deviations from these values, we expect similar parametric effects to occur but with different constants determining the amounts of burn-through and reduced thermal distortion. In conclusion, it appears that the simplified model could be used to predict high power propagation effects during realistic scenario conditions if $\lambda = 10.6$ μm, $F < 10$ and $P/va \leq 100$.

SECTION BIII

EXPERIMENTAL MEASUREMENTS

We experimentally investigated the possibilities of reduced thermal distortion and enhanced transmission for high power laser propagation through fog. This portion of the report summarizes these measurements and the equipment utilized to perform the study.

A. APPARATUS

1. System Overview

A simplified schematic diagram of the expermental system is provided in Fig. B-12. The arrangement consists of six basic components: laser, uniform translator, cell, fog generators, fog diagnostics and target plane diagnostics.

In order to perform the experiment providing full-scale intensity levels it was necessary to use a relatively high powered laser. We employed an electric discharge, transverse flow device developed and maintained at UTRC for the U. S. Navy.[19] Figure B-13 is a photograph of the laser. In the MOPA configuration, this device has provided more than 25 kW; however, our investigation typically required less than 10 kW average output power. During our experiments, the 200-300 watt oscillator beam was chopped at 500 Hz with a 50 percent duty cycle to allow synchronized detection of fog propagation phenomena. The chopping effect is considered negligible in this experiment because the fog is irradiated for sufficient time during each cycle to allow the droplet thermodynamics to approach a steady-state,[6] and the amount of effective pulse overlap is large to ensure CW thermal distortion effects[20] (pulses per flow time of 33-113).

From the laser, the beam was relayed to a translating mirror via a telescope. The moving mirror provided an apparent uniform wind with velocities adjustable between 10 and 50 cm/s. The translation rate was calibrated with a digital system that utilized a stationary photodiode viewing an LED through a photographic negative attached to the moving mirror. The negative had a well defined cyclic bar pattern to generate regular signals in the diode with a frequency dependent on the mirror translation rate. During calibration procedures, the velocity of the mirror was found to be uniform to better than 10 percent over the range given above. The beam was then deflected into the propagation cell by the translating mirror.

2. Aerosol Propagation Cell

The configuration of the aerosol propagation cell is shown in Fig. B-14. The assembled chamber is approximately 10-m long and consists of five equal length sections of approximately 30-cm-ID standard wall thickness aluminum pipe. The recirculation loop of the test chamber consists of five equal sections of approximately 7.5-cm-ID aluminum Schedule 40 pipe. All sections of pipe are interconnected and sealed by means of Vitaulic couplings. Each section of the test chamber and recirculation loop is mounted on its own movable stand.

Two fans for maintaining circulation through the cell are provided. A 7.5-cm dia 529 L/min capacity fan is located in the center section of the recirculation loop. A second fan, 17.5-cm dia and 2175 L/min, is positioned near the cell input. These fans were vital elements for stabilizing the relative humidity for fog absorption data runs and for mixing CO_2 with N_2 for molecular absorption data runs. Each end of the cell was sealed with a 0.0005 mil thick mylar window until the appropriate interior conditions were generated. Then the windows were cut away and a test conducted. A pressure relief valve set at approximately 1.007 atm is located on the test chamber and prevents overpressurization of the mylar windows during introduction of the fog and carrier gas into the test chamber.

Four sets of two diametrically opposed 5-cm dia viewports are provided on the first, third, fourth and fifth test chamber sections, respectively. These ports enabled us to operate fog uniformity tests along the length of the chamber.

Aerosol generators are located on all sections of the propagation cell. Furthermore, the second section contains the scattering and extinction diagnostics for characterization of the fog. Details of the second section are provided schematically in Fig. B-15. The third section contains additional diagnostics, e.g., spectrophone head, relative humidity probe and temperature probe. These diagnostics are described in more detail in following sections of this report. Figure B-16 provides a photograph of the entire cell, viewing from the target toward the input end.

3. Aerosol Generator

In selecting a droplet generator for this experiment, we kept four goals in mind. First, it is desirable to conduct the propogation experiment with a monodisperse population of droplets. This is important from the modeling point of view because the propagation code as we have developed it to this point, assumes a monodispersed population. Since Eq. B-18 and Figs. B-8 - 10 show a sensitivity to the aerosol radius, we place the importance of a monodisperse distribution as a primary goal in selecting a fog generator. As a second goal we would like to operate with a droplet radius that closely resembles natural fog droplets. However, this goal must be tempered with the fact that our experiments are conducted over a very short range compared to that of a full-scale scenario, and we must maximize the droplet absorption efficiency in order to transfer sufficient energy to the ambient gas to simulate realistic thermal blooming conditions. This means that the droplet size should be the largest we can generate compatible with the natural scenario (see Fig. B-3). On the other hand, Fig. B-2 indicates that for large droplets a significant fraction of the intercepted energy will be scattered in addition to being absorbed. This portion of the lost energy is difficult to document during the experiments, so as a practical matter we would also like to maintain as high an absorption to scattering ratio as possible. Droplet radii between 2 and 3 microns represent a good compromise between these various limitations. The third goal envisioned as a specification of the aerosol generator was that it must produce a very large number of droplets per second. If we require on the order of 10^5 droplets per cm^3 and the volume of our chamber is 7.1×10^5 cm^3, then we must provide about 10^{11} droplets per data run. In actuality the number must exceed this value when taking into account those droplets that will be impacted on the sides of the chamber during generation or that will settle out[21] just prior to a data run. Hence, to keep the initial set-up time of the propagation conditions to a reasonable minimum, the aerosol generator must produce about 10^{11} droplets per second. As a final goal in our selection process the fog generator should operate at relatively low air and water pressures so that specialized pumping systems are not required.

Table V summarizes the decision making process in which we were forced to compromise the monodisperse specification in order to obtain a droplet generator satisfactory for fulfillment of this investigation's overall goal of measuring and analyzing fog induced thermal distortion. Of two companies which produce aerosol generators which utilize the shearing forces of an acoustic field to aid the production of uniform droplets, we purchased generators from the Sonic Development Corporation. This company claimed slightly better adjustability of the droplet radius than the other. A photograph of the generator is given in Fig. B-16.

After receipt of the generators, we attempted to document the population distribution emitted at the nozzle outlet. Initially, we used a Corporate-owned, pulsed-ruby holographic system to make records of the generated droplets. This technique was abandoned after a few attempts because the holographic system could only resolve droplets down to 10 μm in radius, leaving most of the population inadequately measured. Then, we employed two angle scattering in a second attempt to characterize the droplets. However, concentration fluctuations in the immediate vicinity of the nozzle made these measurements somewhat unreliable. Our final effort to characterize the fog produced by the generators was conducted by filling a large chamber

(2 m long and 0.25 m diameter) with the fog in a situation similar to that of the real experiments. This procedure was successful, proved that the generator was adequate and is discussed in the next section.

4. Fog Characterization

Since water droplets are rather volatile it is desirable to have real time documentation, of the mean aerosol diameter, the fog droplet concentration, the extinction and absorption coefficients at 10.6 μm, and the visible extinction coefficient. As indicated by Ref. 11 these measurements may be achieved with optical techniques that depend on the relative sizes of the droplets and the probe laser wavelengths. We have accomplished this goal of fog characterization by utilizing transmission and scattering measurements at 10.6 μm and 6328 Å.

Data from the two wavelength transmission diagnostics provide most of the basic information. As an example, the extinction coefficient measured at 6328 Å provides an estimate of the visibility in the experimental fog conditions. Reference 23 shows that the visibility through a fog is simply

$$V \cong \frac{3.912}{\alpha_{ext}(6328\ \text{Å})} \qquad \text{(B-34)}$$

Using this parameter we may compare our scaled measurements with full scale scenarios in which fog conditions are described in terms of the visibility. In addition, the transmission diagnostic provides us with the extinction coefficient of the fog at 10.6 μm which, as we discussed earlier in Section BII, is a fundamental parameter in our modeling of nonlinear propagation through fog.

Furthermore, Fig. B-17 shows that we may measure the average fog droplet radius simply by taking the ratio of the extinction coefficients at the two wavelengths of our transmission diagnostics. With this estimate of the droplet radius we may go back to the extinction measurement at 6328 Å and calculate the droplet concentration by observing

$$C = \frac{\ln(I/I_0)}{2\pi r^2 L} \qquad \text{(B-35)}$$

Reference 24 explains that this method of measuring the aerosol concentration is reliable to about 10 percent. Finally, since we have a measure of the droplet radius, Fig. B-2 can be consulted to give an indication of the absorption coefficient at 10.6 μm for use in the theoretical predictions from the fog propagation models.

We recognize that all of the above analyses assumes that the fog is distributed in a monodisperse population, and we have initiated work to understand the importance of the distribution effects on these measurements. For instance, we simultaneously support the above transmission diagnostics with scattering measurements (6328 Å) at two angles. The scattered intensity ratio for two angles may then be used as an indicator of droplet radius. However, due to the large droplet radius to wavelength ratio for this diagnotic, Mie calculations show very complicated scattering patterns developing as a function of radius (Fig. B-19). The result is depicted in Fig. B-20 which shows a significant amount of ambiguity for the scattered intensity ratio at two selected angles. Much of this ambiguity may be removed by utilizing measurements at angles very near zero degrees. However, this is not practical for our experimental arrangement. Hence, this two angle measurement technique is not a good primary indicator of droplet radius, but does serve as a good technique for confirmation of the radius measured via the transmission diagnostics. During the actual experiments we first found the droplet radius using the transmission data and checked the inferred value with the two angle scattering predictions. In nearly all cases excellent agreement was observed.

The importance of this fact becomes apparent when we analyze the effect of polydispersion on this backup diagnostic of droplet radius measurements. To do this we have developed a computer code for Mie calculations subject to a polydisperse distribution of aerosols. The program incorporates the ZOLD distribution reviewed in Ref. 12. The width and skewness of this distribution are specified by σ_o and the remaining parameter is r_m, the modal radius of the population. For narrow distributions $r = r_m$, the mean radius of a normal distribution, and the equivalent width of a normal distribution is $\sigma = r_m\sigma_o$. Figure B-21 illustrates the density function for $r_m = 2.5$ μm and various σ_o, normalized to the modal value. The effect of this distribution with a small width of $\sigma_o = 0.1$ has been calculated for the two angle scattering diagnostic, Fig. B-22. This figure predicts very obvious differences in the scattering ratio when compared with the monodisperse results of Fig. B-20. Furthermore, our measurements are not consistent with Fig. B-22. Assuming that the ZOLD distribution function is reasonable for modeling our problem, the measurements would infer a real distribution significantly narrower than $\sigma_o = 0.1$. However, modeling and experiments should be extended to further resolve uncertainties surrounding the distribution dilemma

To accomplish the fog characterization measurements discussed above we probe about 2 m of the fog with coaxial HeNe and CO_2 lasers. The beams were combined and directed through a ZnSe window into the propagation cell. After passing through the fog and exiting through another window, the two beams are separated and deflected to their respective detectors. At 6328 Å (chopped) we utilize a simple photodiode/operational amplifier system to produce the signal for phase sensitive detection by a lock-in-amplifier. At 10.6 microns sufficient sensitivity for signal processing was obtained from a Coherent Radiation Laboratories Model 201 power meter. These transmission signals are simultaneously recorded on a strip chart. Concurrently with the transmission recordings, we record scattered light signals at 30 and 60 degrees from the probing HeNe beam. Then during data analysis, we collect the appropriate signal information for fog characterization recorded just prior to the time when the high power beam was propagated through the cell. A photograph of the optical system is provided in Fig. B-23.

5. Spectrophone

During high power propagation through a fog, some of the intercepted energy will be lost to scattering and evaporation of droplets, and some will go directly into heating of the ambient gas. The fraction of energy that is deposited into gas heating dictates the strength of the thermal blooming. Therefore, it is important to measure or otherwise document this amount of heating. One very sensitive method of achieving this information is to measure the strength of pressure waves generated from the gas heating.[25] These perturbations can be detected by an instrument called a spectrophone.[25-30] In this section we discuss a spectrophone developed for these fog propagation experiments.

In contrast with closed cell spectrophones which use Barocell[25,29] type monometers as sensors, the system described here operates with a propagation cell that is not sealed. To accomplish this, the laser source must be chopped. The spectrophone electronics are then "tuned" to the chopping frequency in order to synchronously detect the laser generated pressure waves. The actual detector of the pressure waves is a microphone.[26,27,28,30] In the system that we have constructed, the microphone is followed by an ultra-low noise preamplifier (Fig. B-24). The output of this preamplifier is filtered by a preselector before final measurement with a lock-in-amplifier.

Table B-VI indicates the basic characteristics of the components used in our spectrophone. The information suggests that for operating conditions during which no background noise exists the minimum detectable pressure signal will be dictated by the noise characteristics of the microphone, rather than the subsequent electronics. In practice, however, ambient laboratory sound levels limit the minimum detectable pressure signals. This fact can be illustrated by the following preliminary spectrophone tests.

The spectrophone head (consisting of the microphone and the preamplifier) was mounted in the middle of a one meter propagation cell. The cell diameter was about 3.8 cm. Initial tests were conducted with germanium windows closing off the cell. The windows were used only to hold in the calibration gas and were not pressure-sealed. A 6 watt CO_2 beam was aimed coaxially down the cell and chopped at 500 Hz. The beam radius was about 0.3 cm. The dimensions were chosen to be an approximate one-tenth scaling of the larger fog propagation experiment. The test cell was flooded with CO_2, and the lock-in-amplifier was adjusted for maximum response. For 125 seconds averaging time and an effective bandwidth of 0.001 Hz, the output was 36 mV rms. The beam was then blocked so that the spectrophone responded to only background noise. The background signal level was 0.002 mV rms. These measurements imply a signal to noise ratio of 1.8×10^{4}. Since the absorption coefficient of CO_2 is about 1.4×10^{-3} cm^{-1}, the noise equivalent absorptivity of the spectrophone is about 7.8×10^{-8} cm^{-1}.

When the cell windows were removed so that the laboratory background noise had its full impact on the spectrophone, the background level increased to 0.035 mV rms. Hence, the signal to noise ratio for the completely open cell was 1.0×10^{3}. The resultant noise equivalent absorptivity becomes 1.4×10^{-6} cm^{-1}.

The important question to be answered next, is whether or not these spectrophone characteristics are sufficient for the full scale fog propagation experiment. References 25 and 31 show that the laser generated pressure waves will have to be proportional to $\alpha P/\pi a_o^2$ where α is the absorption coefficient (cm^{-1}), P is the laser power (W) and a_o is the beam radius (cm). For our initial spectrophone tests, this quantity was 3.0×10^{-2}. In the case of the fog propagation experiment, we will have an aerosol absorption coefficient of about 1.0×10^{-3} cm^{-1}, a power of 5 kW or more and a beam radius of approximately 2.5 cm. The quantity discussed above becomes 2.6×10^{-1}. This represents nearly an order of magnitude increase in the signal to noise ratio for the fog experiments and pressures still within the dynamic range of the microphone. In conclusion, this spectrophone electronics design is satisfactory for the larger fog propagation experiments.

6. Target Plane Diagnostics

In the target plane, the beam is attenuated by reflection from two NaCl wedges and is deflected to a scanned, linear array of pyroelectric detectors. Its 32 elements can be read at a 5 kHz rate, but only 500 Hz was utilized in this experiment. The array triggering was synchronized to the chopper in the high power laser oscillator with an adjustable time delay to optimize phasing. In this fashion, we were able to measure a profile of the beam as it was translated across the array. The array output was fed into an adjustable gain amplifier and then to an operational amplifier follower circuit to eliminate loading effects on the detection systems calibration. The output signals from the follower were recorded on a video tap recorder used as a wide bandwidth FM data recorder. These signals were used later to reconstruct the fog induced thermal blooming profiles.

7. Data Analysis

Analysis of the recorded beam profiles was accomplished by digitizing the array generated profiles using a Tektronix Digital Processing Oscilloscope. The digitized data was stored on floppy discs for analysis by a PDP-11 minicomputer. Application of this system enabled us to reconstruct the high power beam's two-dimensional intensity distribution, measure I_{rel}, measure the increased area of the distorted beam, and calculate the power delivered to the target by integrating over the intensity distribution. The results of this analysis are presented next.

B. RESULTS

An example of the reconstructed intensity distributions is provided in Fig. B-25. Here, we illustrate on an arbitrary intensity scale that fog induced thermal blooming (increased beam area) is reduced merely by increasing the laser power from about 1.8 kW to just over 6.2 kW. The spatial scale is identical for both runs. The area of the lower power run is 2 times the undistorted beam area. In the second case, the beam was very effective in destroying much of the fog, and it burned its way to the target with only a 2 percent area increase over the undistorted case. This reduced thermal distortion was achieved even though αL of the higher power run was 43 percent greater. Referring to the classical model, thermal blooming decreased even when the standard nonlinear distortion parameter increased by a factor of about 5. Ordinarily for molecular absorption this would have resulted in about a 5-fold increase in beam area going from the lower to the higher power case, but instead we observed a 2-fold decrease due to the increased burn-through of the higher power case. Our attempts to comprehensively analyze measurements of these new nonlinear propagation effects are presented in the following discussion of the observed parameters I_{rel}, A_{rel}, and P_{rel}.

1. I_{rel}

Figure B-26 summarizes the measurements of I_{rel} for the range of experimental conditions listed in Table I. I_{rel} is defined as $I/I_0e^{-\alpha_{abs}L}$ where α_{abs} is indicative of the molecular absorber or the unmodified fog conditions in the cell. The same absorption coefficient is used deriving N_f from Eq. (B-7). Figure B-26 shows that our experimental system measured molecular absorption (CO_2 diluted with N_2) induced thermal distortion that was consistent with the classical, empirical model of Eq. (B-6). Furthermore, when the relative humidity of the cell was forced to near saturation but no fog droplets were present, we again measured thermal distortion that was well described by the molecular absorption model. However, in this case, the dominate absorption coefficient resulted from water vapor.

The breakdown of the empirical model is dramatically displayed in Fig. B-26 for data collected when fog was the dominate absorber in the cell. During these conditions P was increased, v was decreased or α_{abs} was increased to force larger values of N_f. But rather than observing increased thermal distortion, we measured increasingly better propagation. We were able to deliver up to 10,000 times more peak intensity to the target than would be expected based on the linear absorption due to the fog at low intensities. The enhanced propagation resulted from forced vaporization of the droplets, enabling increased transmission and decreased thermal distortion. The following discussion will enable us to differentiate between the two effects.

2. A_{rel}

The extent of decreased thermal distortion is illustated in Fig. B-27 which shows the ratio of the area in the 1/e intensity contour of the undistorted beam to the distorted profile. The data is plotted as a function of the same N_f used in Fig. B-26. The empirical model is used in this case to indicate the approximate parametric form of A_{rel} for molecular absorption induced thermal distortion. The data shows significantly less thermal blooming than expected. However, no new parametric dependencies on N_f are observed due to the fact that many different P, v, and fog conditions were utilized during these measurements. We stress at this point that N_f based on the unmodified fog characteristics is no longer a good measure of parametric effects.

3. P_{rel}

We display the amount of enhanced transmission through the fog in Fig. B-28. P_{rel}, which is defined as the power transmitted to the target plane through the 1/e intensity contours of the distorted beam in proportion to the undistorted beam, is given as a function of the unmodified optical thickness of the fog, $\alpha_{ext}L$. This parameter should illustrate extinction of the beam independent of the thermal distortion mechanism. Our measurements show that propagation of a beam with sufficient power to force droplet vaporization provides increased transmission, and that the unmodified fog extinction coefficient is no longer useful for parameterization.

4. Spectrophone Corrected I_{rel}

During some of our data runs, we successfully operated the spectrophone in conjunction with the other diagnostics. The spectrophone measures pressure waves induced in the ambient gas resulting from absorbed energy that goes into gas heating and is not sensitive to that absorbed energy which is used to vaporize particles. Therefore, the effective absorption coefficient measured by the spectrophone ignores the unmodified fog parameters and responds directly to the average effective absorption coefficient of the fog as actively modified by the high power beam. It is this modified fog absorption coefficient which causes distortion. The spectrophone measurements are calibrated by comparing signals recorded during CO_2, molecular absorption, blooming experiments with signals from the fog experiments. A simple, geometric argument is used to account for blooming induced changes in beam radius at the spectrophone location. The effective, modified fog absorption coefficient is utilized to calculate new values of I_{rel} and N_f. The results are compared in Fig. B-29 with the same parameters based on the unmodified fog characterization. The spectrophone corrected I_{rel} measurements agree with the empirical model, and this fact supports our code calculations that show: thermal blooming induced by fog agrees with the empirical model if the appropriate modified absorption coefficient within the beam is known.

5. Direct Comparison with Code

The measured A_{rel} and P_{rel} values were compared directly with the modified nonlinear propagation code taking into account vaporization. The results are shown in Figs. B-30 and B-31. We find very little correlation between the measurements and the code predictions. A similar problem was encountered when we attempted to parameterize the measurements by the (P/va) modified absorption coefficients predicted by the code study. The scatter is too great to draw any useful conclusions. Without further extended measurements and code exercises, we cannot determine whether the dominate uncertainty lies in the code predictions or in the experimental measurements.

SECTION BIV

CONCLUSIONS

We have performed a scaled experimental investigation of high power laser propagation effects in fog. The beam was sufficiently powerful to vaporize much of the fog. As a result we observed transmission enhanced beyond expected levels and less thermal distortion than would be normally predicted. The standard empirical model used to describe thermal blooming was found inadequate when based on the standard fog absorption coefficient. However, if a new absorption coefficient was identified for the actively modified fog by use of a spectrophone, then the empirical model agreed with the measurements.

In support of the measurements we have developed a nonlinear propagation code that takes into account fog vaporization forced by the high power beam. The code predicts enhanced transmission and decreased thermal distortion. Some simplified scaling for the modified fog parameters has been identified, and as in the experiments when the modified absorption coefficient was used as a parameter, the validity of the empirical model was retained. So as verified by spectrophone measurements and detailed code calculations a useful, simplified parametric scaling law has been identified for high power propagation through fog. To describe thermal distortion Eq. B-33, the beam modified fog absorption coefficient, is used in conjunction with Eqs. B-6 and B-7; while to predict enhanced transmission Eq. B-31 may be utilized in Eq. B-32. Finally, some inconsistencies were found for a detailed comparison between the absolute code predictionsand the experimental measurements. But with the studies limited to this report we have not been able to identify whether the dominant uncertainties lie in the new code or in the experimental measurements. Further effort should be extended to resolve these questions.

SECTION BV

SUGGESTIONS FOR FURTHER WORK

In this closing section we list items that should be considered to aid in the resolution of remaining questions with respect to high power laser propagation through fog:

1. The modified code should be exercised over a much broader range of conditions. This would aid in identification of additional simplified scaling possibilities, and identification of real-scale system capabilities.

2. Additional experiments should be conducted to investigate limits on the validity of the modified absorption coefficient modeling and the parametric dependencies of aerosol induced blooming.

3. Additional fog characterization should be initiated for direct characterization of the droplet population width and distribution.

4. The code should be modified to account for fog droplet populations of variable width and distribution.

5. In an attempt to further model real-scale meteorological conditions, experiments should be conducted with fogs activated by hygroscopic nuclei.

6. Code modifications should be developed to predict the effects of high power beams on fogs with hygroscopic nuclei.

REFERENCES FOR SECTION B

1. J. A. Dowling and K. M. Haught. Laser-Calibrated High-Resolution Atmospheric Transmission Measurements, Paper 15.5 presented at the 1977 Conference on Laser Engineering and Applications, Washington, C.D., June 1-3, 1977.

2. F. G. Gebhardt, Appl. Opt. 15, 1479 (1976).

3. D. C. Smith and R. T. Brown. Laser-Particle Interaction, Final technical Report N-921503-16 on Contract No. N00014-72-C-0469, Sponsored by the Office of Naval Research, Washington, D.C., October 1974.

4. R. T. Brown and D. C. Smith, J. Appl. Phys. 46, 402 (1975).

5. D. E. Lencioni and H. Kleiman. Effects of Aerosol Particle Heating on Laser Beam Propagation, Project Report LTP-27 on Contract No. F19628-73-C-002, sponsored by the Advanced Projects Agency, July 22, 1974.

6. G. E. Caledonia and J. D. Teare. Aerosol Propagation Effects, Final Report, Physical Sciences Inc., PSI TR-13, September 13, 1974.

7. S. L. Glickler, Appl. Opt. 10, 644 (1971).

8. J. E. Lowder, et al., J. Appl. Phys. 45, 221 (1974).

9. G. J. Mullaney, et al., Appl. Phys. Lett. 13, 145, (1968).

10. D.C. Smith and R. T. Brown. Effects of Particulate Matter on Atmospheric Propagation of CO_2 Laser Radiation, Semi-annual Technical Report N921503-10 on Contract No. N00014-72-C-0469, Sponsored by the Office of Naval Research, Washington, D.C., May 1974.

11 H. C. Van De Hulst. Light Scattering by Small Particles (John Wiley and Sons, Inc., N.Y., 1957).

12. M. Kerker. The Scattering of Light and Other Electromagnetic Radiation (Academic Press, N.Y., 1969).

13. A. J. Cantor. A Mie Scattering Computer Program, United Technologies Report UTRC77-28, March 1977.

14. T. S. Chu and D. C. Hogg, Bell Syst. Tech. J. 47, 723 (1968).

15. F. A. Williams, Int. J. Heat Mass Transfer 8, 575 (1965).

REFERENCES FOR SECTION B (CONT'D)

16. F. G. Gebhardt and D. C. Smith, IEEE J. Q. E. QE-7, 63 (1971).

17. A. J. Cantor. A Guide for Users of the UTRC CW and NRL Multipulse Nonlinear Wave-optics Propagation Codes, United Technologies Report UTRC77-9, March 1977.

18. J. Herrmann and L. C. Bradley. Numerical Calculations of Light Propagation, MIT/Lincoln Laboratory Laser Technology Program Report LTP-10, Lexington, MA, July 1971.

19. C. O. Brown, et al. Investigation of a High-Power CO$_2$ Convection Laser, Summary Technical Report UARL L910990-22 on Contract No. N60921-70-C-0219, Sponsored by the Naval Ordance Systems Command, May 1, 1972.

20. J. Wallace and J. Q. Lilly, J. Opt. Soc. Am., 64, 1651 (1974).

21. C. N. Devies. Aerosol Science (Academic Press, N.Y., 1967).

22. Sonic Development Corporation, 3 Industrial Ave., Upper Saddle River, N.J., 07458.

23. W. E. K. Middleton. Vision Through the Atmosphere (University of Toronto Press, 1968).

24. H. R. Carlon, Appl. Opt., 15, 2454 (1976).

25. E. L. Kerr and J. G. Atwood, Appl. Opt., 7, 915 (1968).

26. L. B. Kreuzer, J. Appl. Phys., 42, 2934 (1971).

27. L. Rosengren, Infrared Phys., 13, 109 (1973).

28. C. F. Dewey, Jr., et al., Appl. Phys. Lett., 23, 633 (1973).

29. T. F. Deaton, et al., Appl. Phys. Lett., 26, 300 (1975).

30. K. O. White, et al., Absorption of Atmospheric Gases in the Deuterium Fluoride Laser Spectral Region: 3.5-4.0 um, A preprint, August 1976.

31. W. J. Fader, J. Appl. Phys., 47, 1975 (1976).

TABLE I

Comparison of experimental parameters and approximate field conditions. P is power; a is the 1/e intensity radius of the beam; L is the pathlength; I is the intensity, v is the velocity, αL is the product of the absorption coefficient and pathlength; N_f is the thermal distortion scaling parameter for a focused beam (defined in text); r is the fog droplet radius; C is the fog droplet concentration; and m is the total water mass density of the fog.

	LAB	FIELD
Nondimensional Propagation Parameters		
F	= 8.0	8.3
αL	= 1-5	1-5
N_F	= 20-200	20-200
Physical Propagation Parameters		
P/va	= 40-200	P/va = 71-286
P	= 3 kW	--
a	= 1.5 cm	--
L	= 10^3 cm	2 x 10^5 cm
v_2	= 10-50 cm/s	50-200
C_h^2	= 0	10^{-14} $m^{-2/3}$
σ_J(jitter)	= 0	10 μrad
Fog Parameters		
r	= 2 x 10^{-4} cm	2 x 10^{-4} cm
C	= 3-17 x 10^4 cm^{-3}	1.7-8.4 x 10^2 cm^{-3}
m	= 1-5.7 gm/m^3	0.0056-0.028 gm/m^3
visibility (6328 Å)	= 6.47 x 10^2 cm - 3.24 x 10^3	1.3 x 10^5 cm - 6.4 x 10^5
	Very Dense Generated Fog	Light to Medium Natural Fog

TABLE II

RANGE OF PARAMETERS USED IN ACTUAL EXPERIMENTS

Power = 0.89 - 6.2 kW

Beam radius (1/e) = 1.45 - 1.66

Absorber Length = 1000 cm

Length to detectors = 1172 cm

Beam quality = 1.76 - 4.79

Fresnel number = 2.6 - 7.9

Velocity = 15 - 46 cm/s

Fog absorption coefficient (10.6 μm) = 0.74 - 4.26 x 10^{-3} cm^{-1}

Fog droplet radius, typical = 2.0 μm

TABLE III

PROPAGATION THROUGH NONVOLATILE FOG

Foggy Atmosphere

Linear Problem:

$r = 2 \times 10^{-4}$ cm

$Q_{ext} = 3.07 \times 10^{-1}$

$C = 207$ cm^{-3}

α_{ext} (Eq. 4) $= 8.0 \times 10^{-6}$ cm^{-1}

$L = 2 \times 10^{5}$ cm

- I/I_o (Eq. 2) $= 0.20$

Nonlinear Problem:

$r = 2 \times 10^{-4}$ cm

$Q_{abs} = 2.54 \times 10^{-1}$

$C = 207$ cm^{-3}

α_{abs} (Eq. 10) $= 6.6 \times 10^{-6}$ cm^{-1}

$F = 8.3$

$v = 200$ cm/s

$z = 2 \times 10^{5}$ cm

$P/va = 71.4$ W/cm^{2}S

N_F (Eq. 7) $= 25.7$

- I_{rel} (Eq. 6) $= 0.0237$

Clear Atmosphere

Linear Problem:

$\alpha_{ext} \cong \alpha_{abs} \cong 2 \times 10^{-6}$ cm^{-1}

$L = 2 \times 10^{5}$ cm

- I/I_o (Eq. 2) $= 0.67$

Nonlinear Problem:

$\alpha_{abs} \cong 2 \times 10^{-6}$ cm^{-1}

F, a, v, z P as above

N_f (Eq. 7) $= 10.1$

- I_{rel} (Eq. 6) $= 0.135$

TABLE IV

PARAMETER VARIATIONS OF FIGS. 8-10

Fixed:

$n_T = 8.75 \times 10^{-7}\ {}^{o}C^{-1}$

$Z = 10^{3}$ cm

$n = 1.0$

$\rho = 1.18 \times 10^{-3}$ cm^{-3}

$c_p = 1.0$ J/g ^{o}C

$a = 1.45$ cm

$F = 4.79$

Varied:

Power (kW)	Velocity (cm/s)	Initial Drop Radius (μm)	Concentration (cm^{-3})
0.5	10	1.7	3.5×10^{4}
1.0	20	1.9	4.0×10^{4}
2.0	30	2.1	4.5×10^{4}
4.0	40	2.3	5.0×10^{4}
	50	2.5	5.5×10^{4}

TABLE V

AEROSOL GENERATOR DECISION PROCESS

Approximate Geometric Standard Deviation* of Population	Type of Generator	Comment
< 1.05	Berglund vibrating orafice	Too few per second
1.05 to 1.15	Spinning disc	Too few per second and primary droplets too large
∿ 1.2	Atomizer with impactor and evaporative control	Droplets too small and typically used with oil rather than water
1.4 to 1.8	Atomizer with impactor	Droplets too small
1.8 to 2.0	Immersed ultrasonic transducer	Too few per second
1.5 to 3.0	Atomizer with acoustic field	Adequate production rate, size range and operating pressures.

*The geometric standard deviation is the radius of the 84.1 point to the radius of the 50 percent point on the cumulative distributions of the droplet population. For example, if the geometric standard deviation is 1.0 then all droplets have the same size.

TABLE VI

SPECTROPHONE COMPONENTS

Microphone	**Electronic**	**Absolute Pressure**
Noise (Total A-weighted) (Equivalent 1 kHz)	30 db*	6.3×10^{-3} μB 6.5×10^{-5} μB/√Hz
Distortion (3% THD)	120 db	2.0×10^{2} μB
Response (Re 1V/μB for 50-2 kHz)	-70 db ± 3	3.2×10^{-4} V/μB
Dynamic Range	90 db	3.2×10^{4}
Preamplifier (LM381AN)		
Equivalent Input Noise (total, 10-10 kHz) (at 1 kHz)	$0.5\ \mu V_{rms}$ 5.5 nV/√Hz 0.35 pA/√Hz	1.6×10^{-3} μB 5.4×10^{-5} μB/√Hz at R_L = 47 kΩ
Dynamic Range (measured)	$> 10^{4}$	
Lock-In-Amplifier (Ithaco 391)		
Noise (Typical at 1 kHz)	5 nV/√Hz 0.03 pA/√Hz	1.6×10^{-5} μB/√Hz at 50 Ω
Bandwidth (Selectable)	0.001-100 Hz	
Averaging time	1.25 mS - 125 S	
Accuracy	1%	
Chopper		
Frequency	∿ 500 Hz	
Stability	0.1%	

---

*Relative to 2×10^{-4} μB

ANGULAR SCATTERING FUNCTION

λ = 10.6 µm

H_2O DROPLET

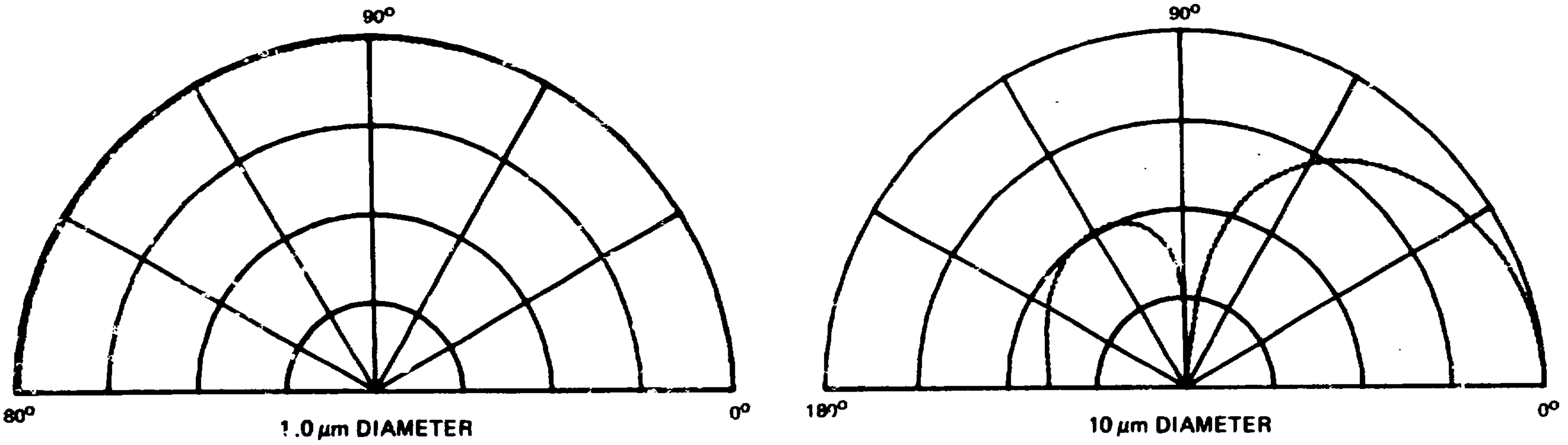

1.0 µm DIAMETER

10 µm DIAMETER

FIG. B-1

76-10-142-3

RATIO OF ABSORPTION AND SCATTERING EFFICIENCIES

H_2O DROPLET

$\lambda = 10.6\ \mu m$

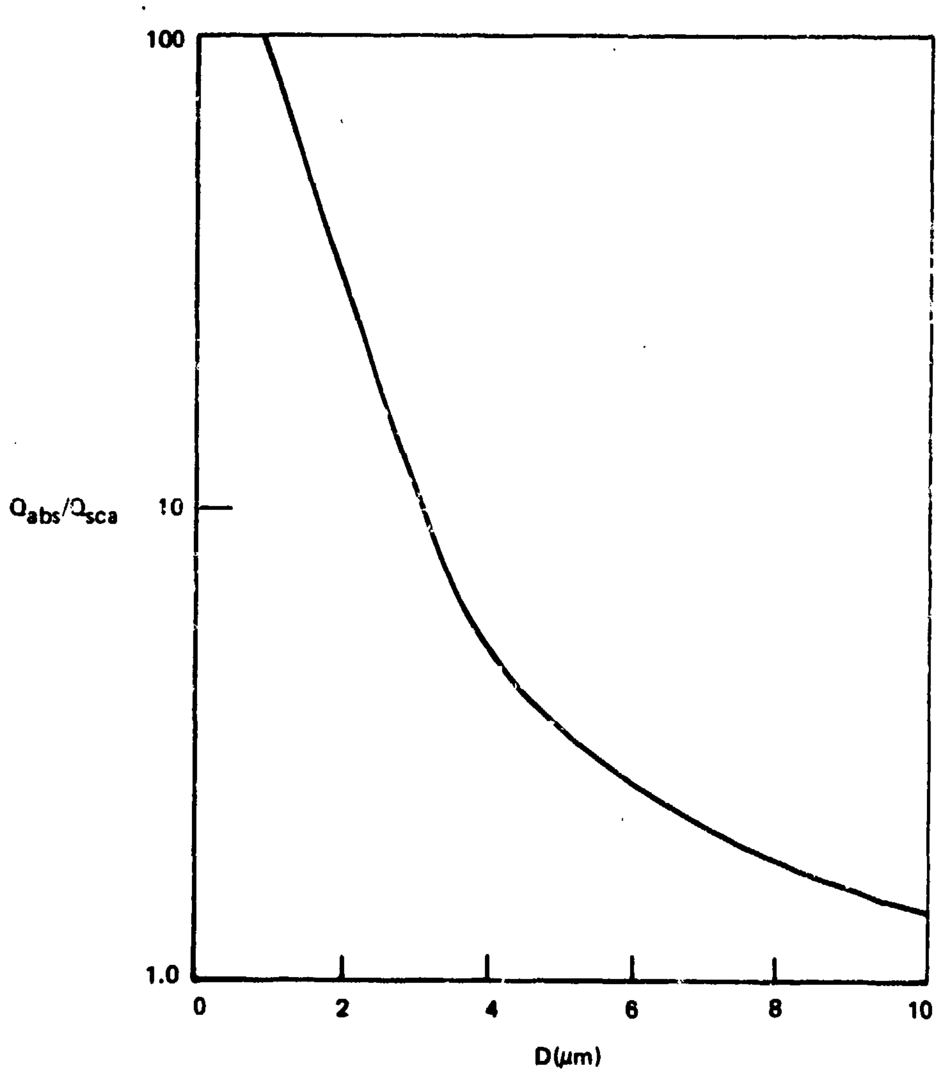

77–06–274–11

FIG. B–3

ABSORPTION EFFICIENCY

H_2O DROPLET

λ = 10.6 μm

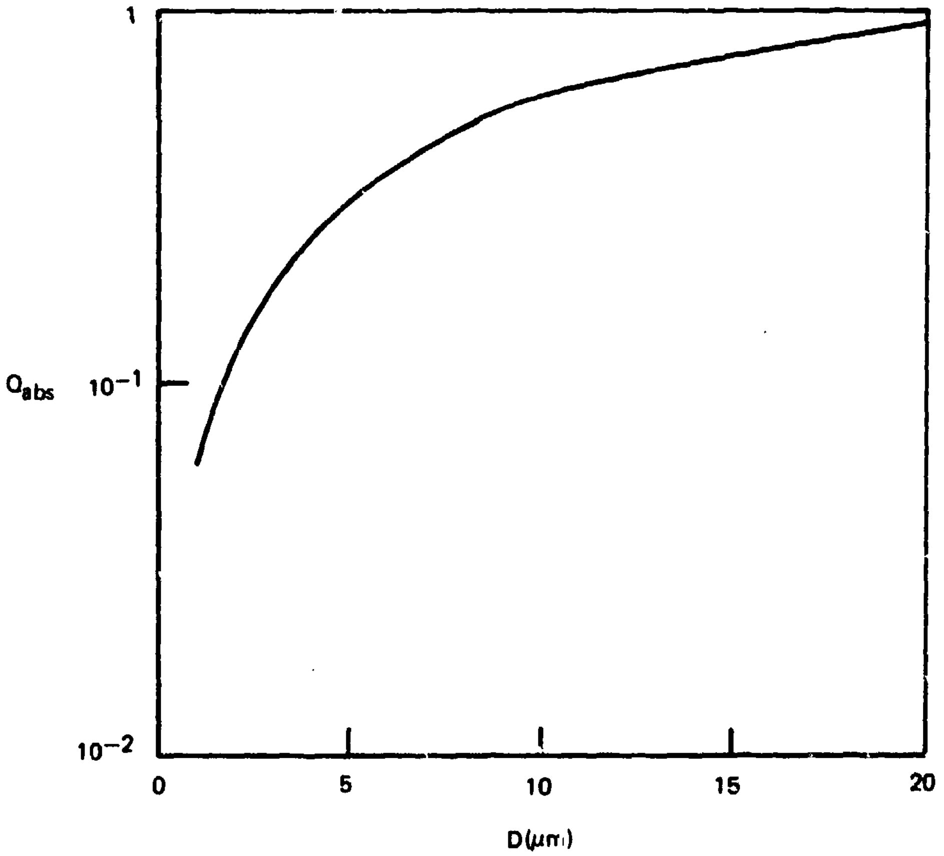

77–06–274–12

FIG. B-4

FOG DROPLET DECAY IN HIGH POWER BEAM

r(initial) = 10.6 μm
P = 50 kW, UNIFORM
a = 1.5 CM
v = 15 CM/S
λ = 10.6 μm

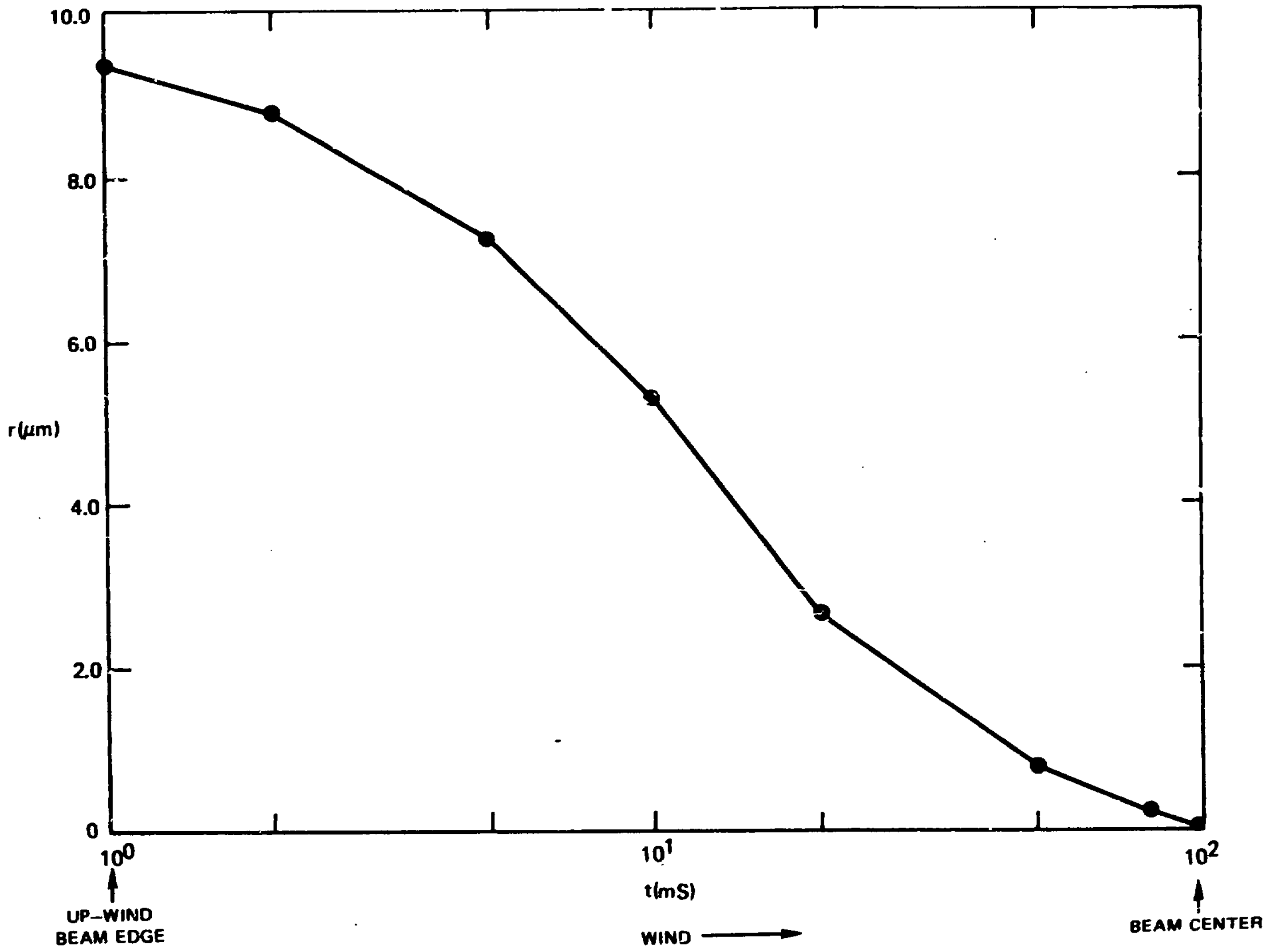

FIG. B–5

TEMPERATURE CHANGE INDUCED IN ATMOSPHERE

UNIFORM BEAM

$P = 5$ kW
$\omega = 2$ cm
$F = 1$
$v = 25$ cm/S
$r = 2\ \mu$m
$C = 5\times10^4$ cm -3

77–06–274–13

CODE PREDICTIONS WITH SATURABLE FOG ABSORBER

$P = 0.5$ kW
$a_i = 1.45$ cm
$a_f = 0.346$ cm

$v = 33$ cm/s
$r = 2.1\,\mu m$
$C = 4.55 \times 10^4$ cm^{-3}

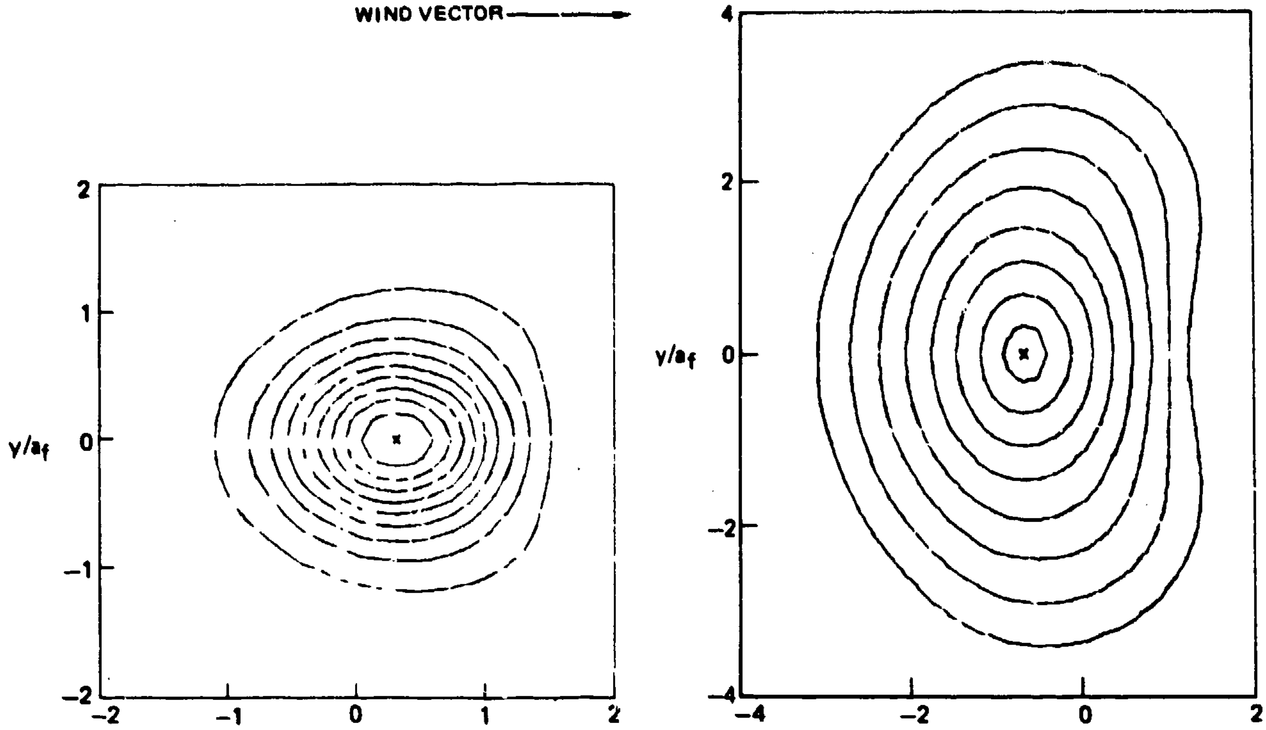

PHASE DISTRIBUTION
(10% CONTOURS ABOUT ϕ_{MAX})

INTENSITY DISTRIBUTION
(10% CONTOURS ABOUT I_p)

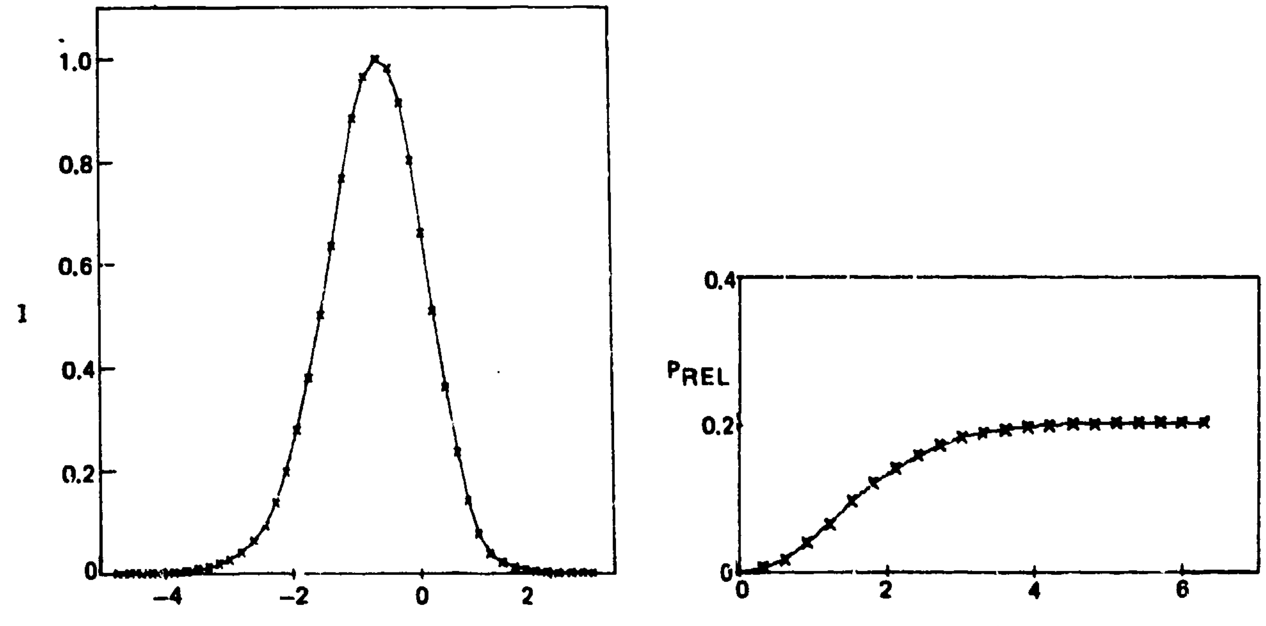

TRANSVERSE INTENSITY PROFILE
(THROUGH I_p)

INTEGRATED INTENSITY

CODE PREDICTIONS WITH SATURABLE FOG ABSORBER

$P = 4.0$ kW
$a_i = 1.45$ cm
$a_f = 0.346$ cm

$v = 33$ cm/s
$r = 2.1\mu M$
$C = 4.55 \times 10^4$ cm^{-3}

WIND VECTOR ⟶

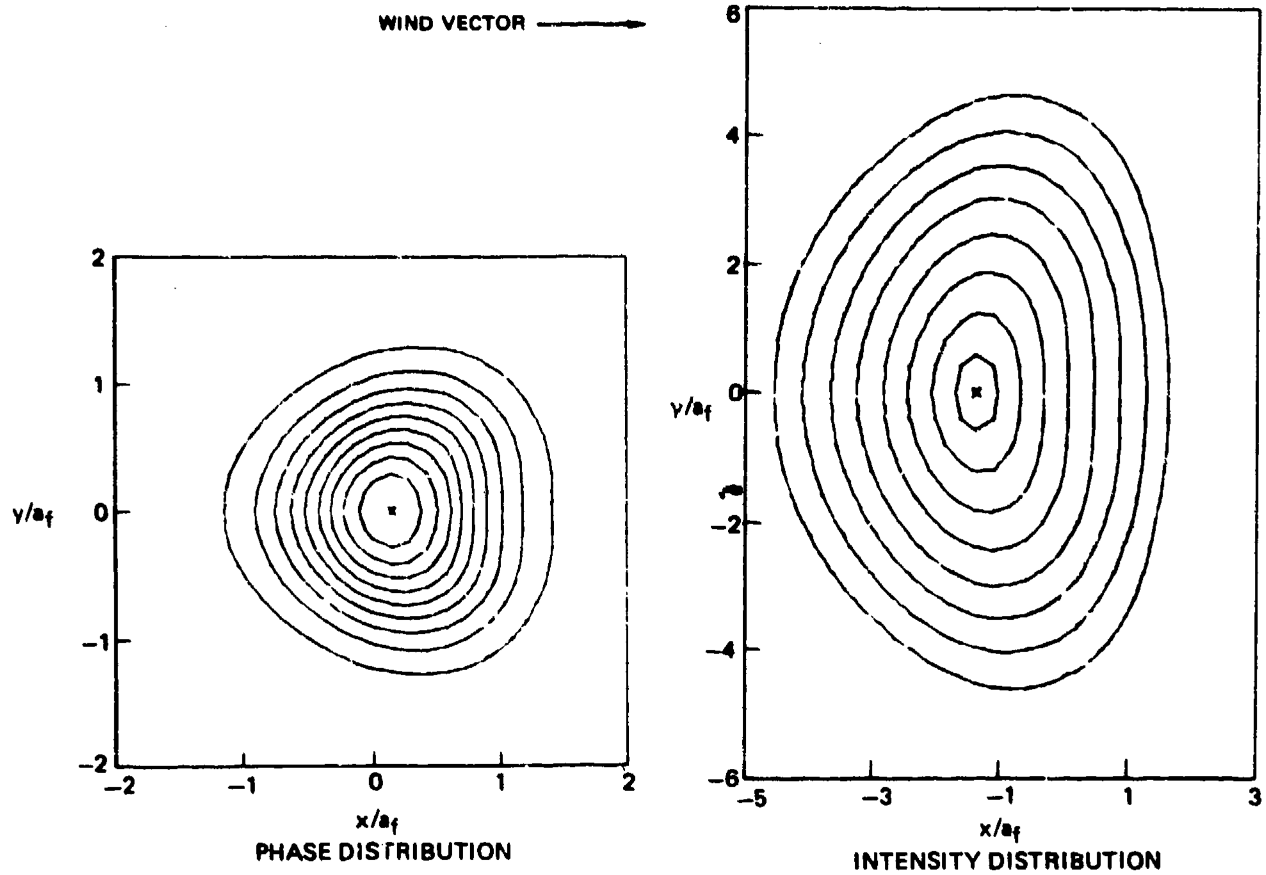

PHASE DISTRIBUTION
(10% CONTOURS ABOUT ϕ_{MAX})

INTENSITY DISTRIBUTION
(10% CONTOURS ABOUT I_p)

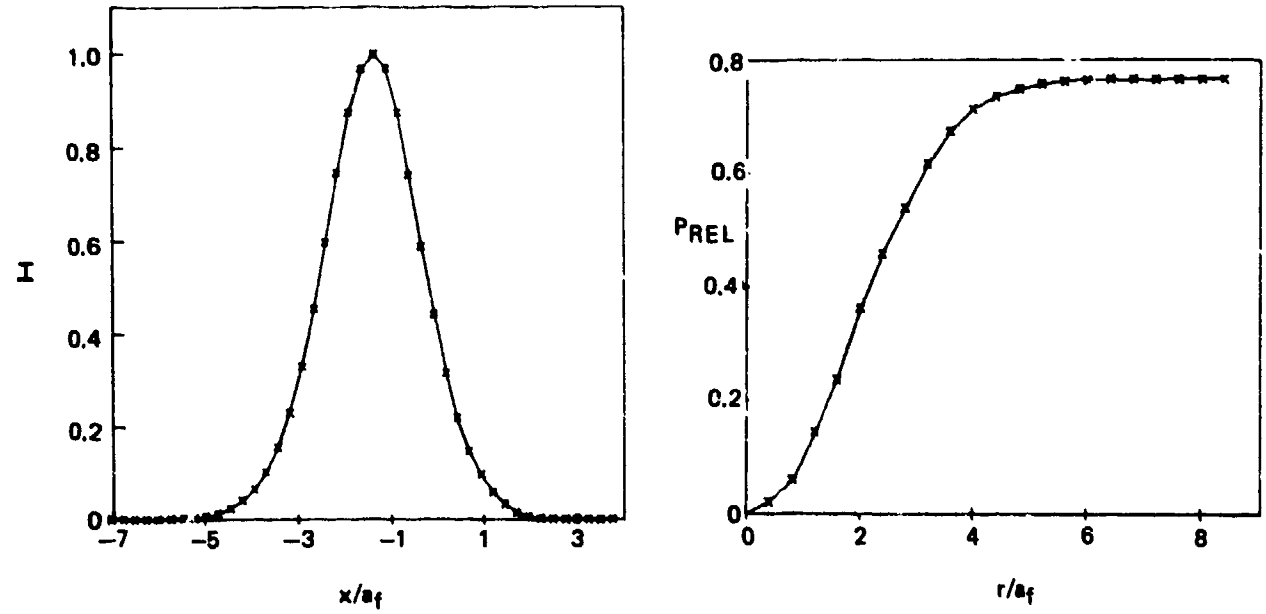

TRANSVERSE INTENSITY PROFILE (THROUGH I_p)

INTEGRATED INTENSITY

FIG. B-8

CODE PREDICTIONS WITH SATURABLE FOG ABSORBER

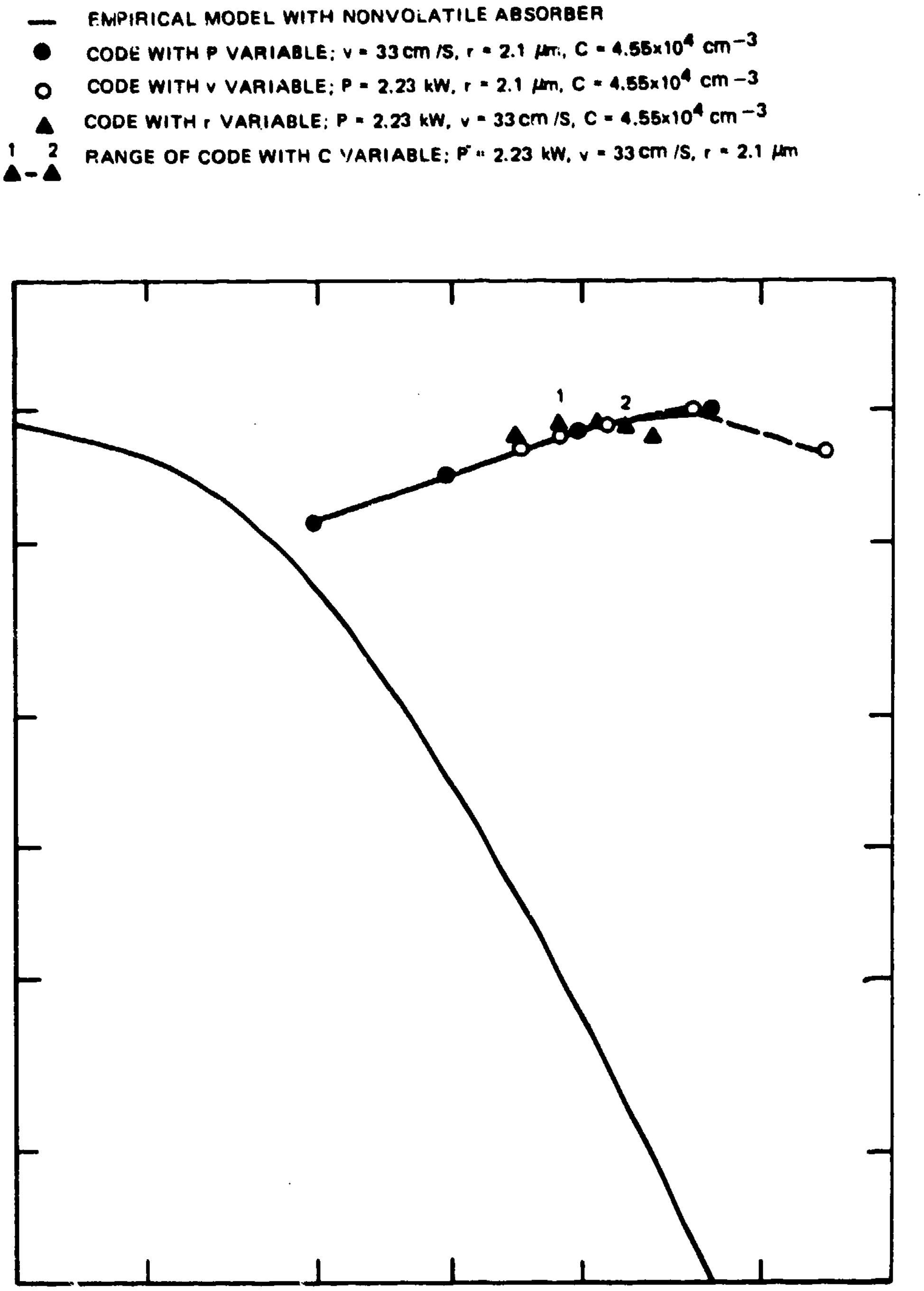

77-06-274-7

CODE PREDICTIONS WITH SATURABLE FOG ABSORBER

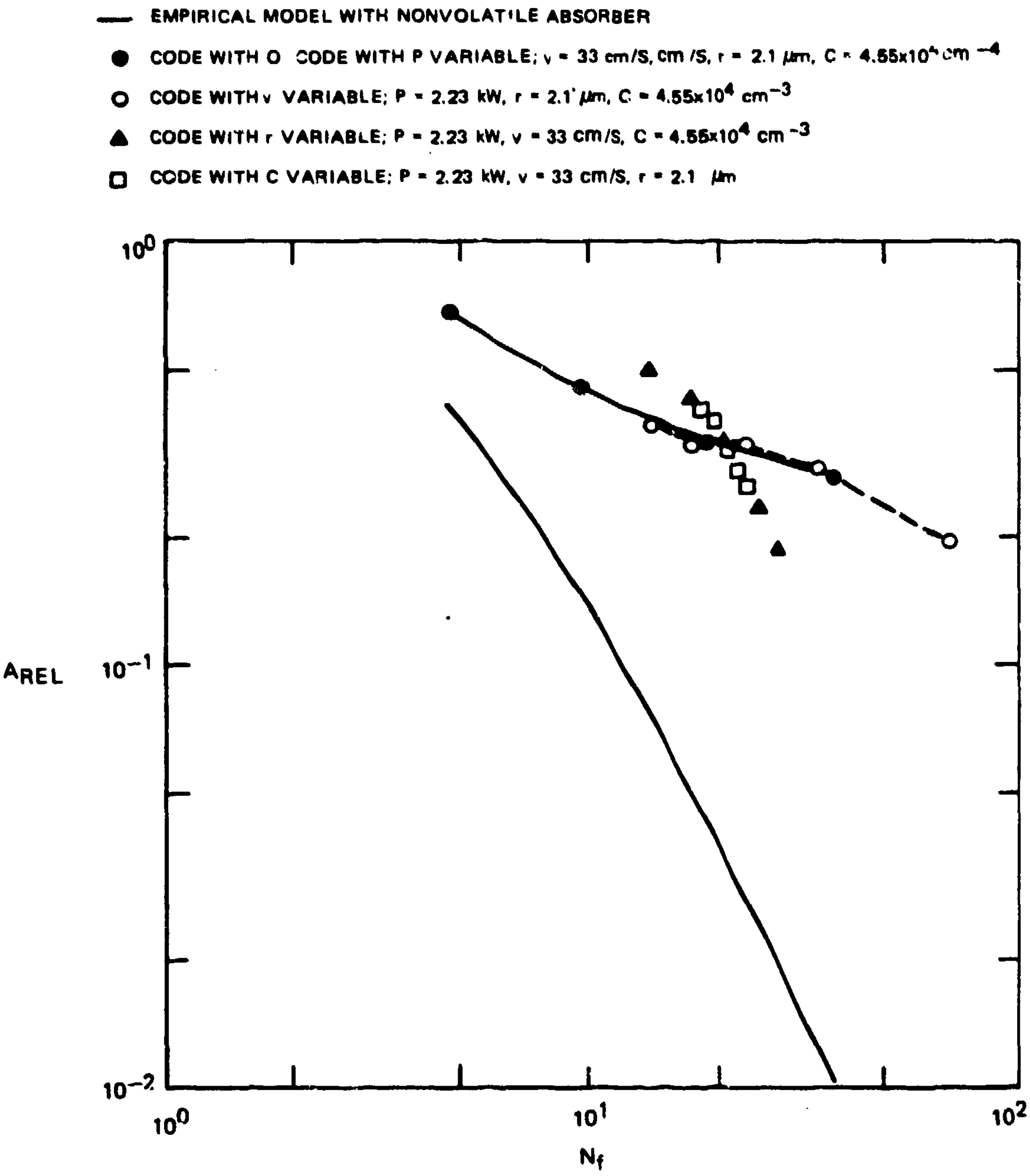

FIG. B–10

CODE PREDICTIONS WITH SATURATED FOG ABSORBER

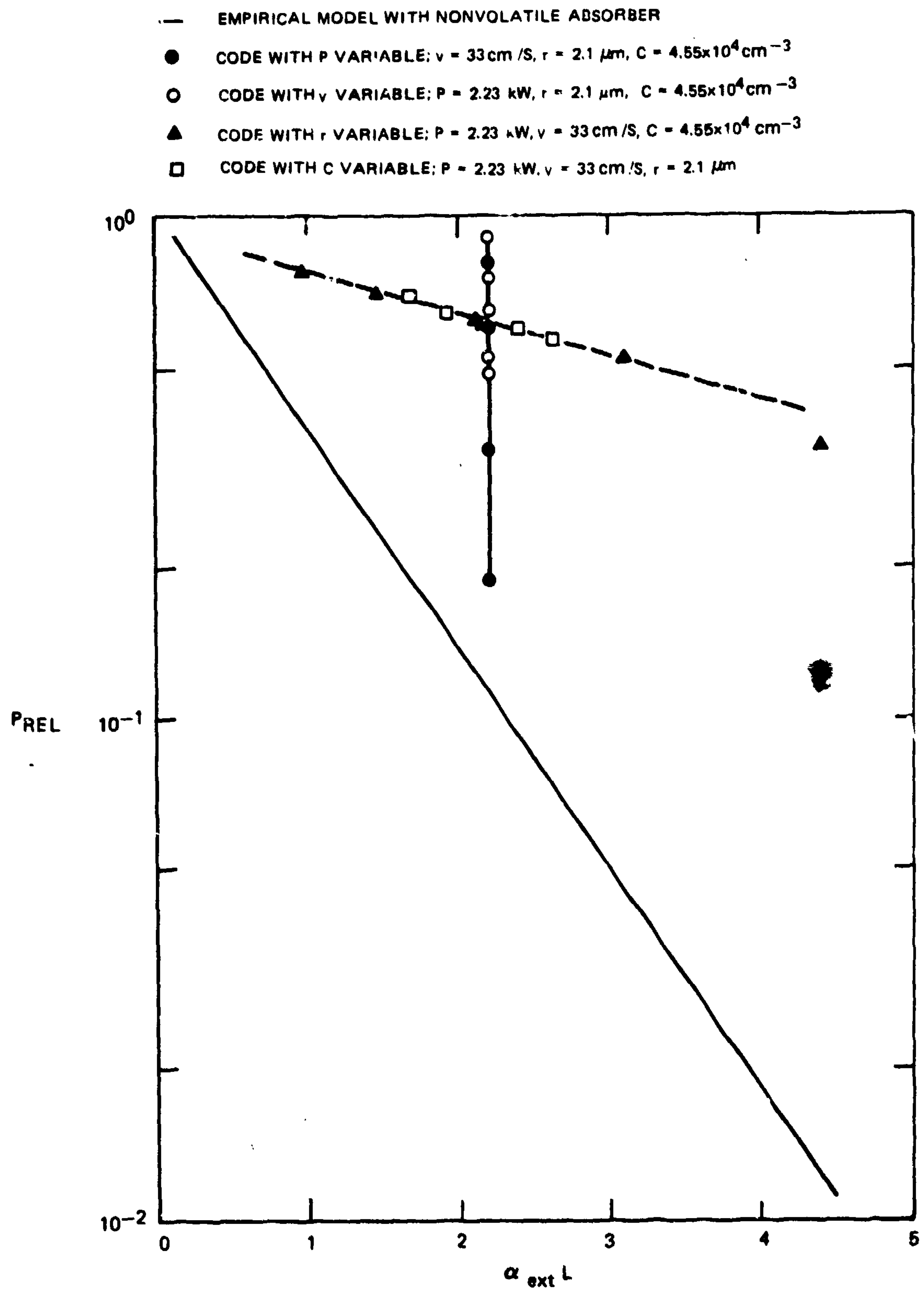

77–06–274–9

APPLICATION OF MODIFIED SCALING TO CODE PREDICTIONS

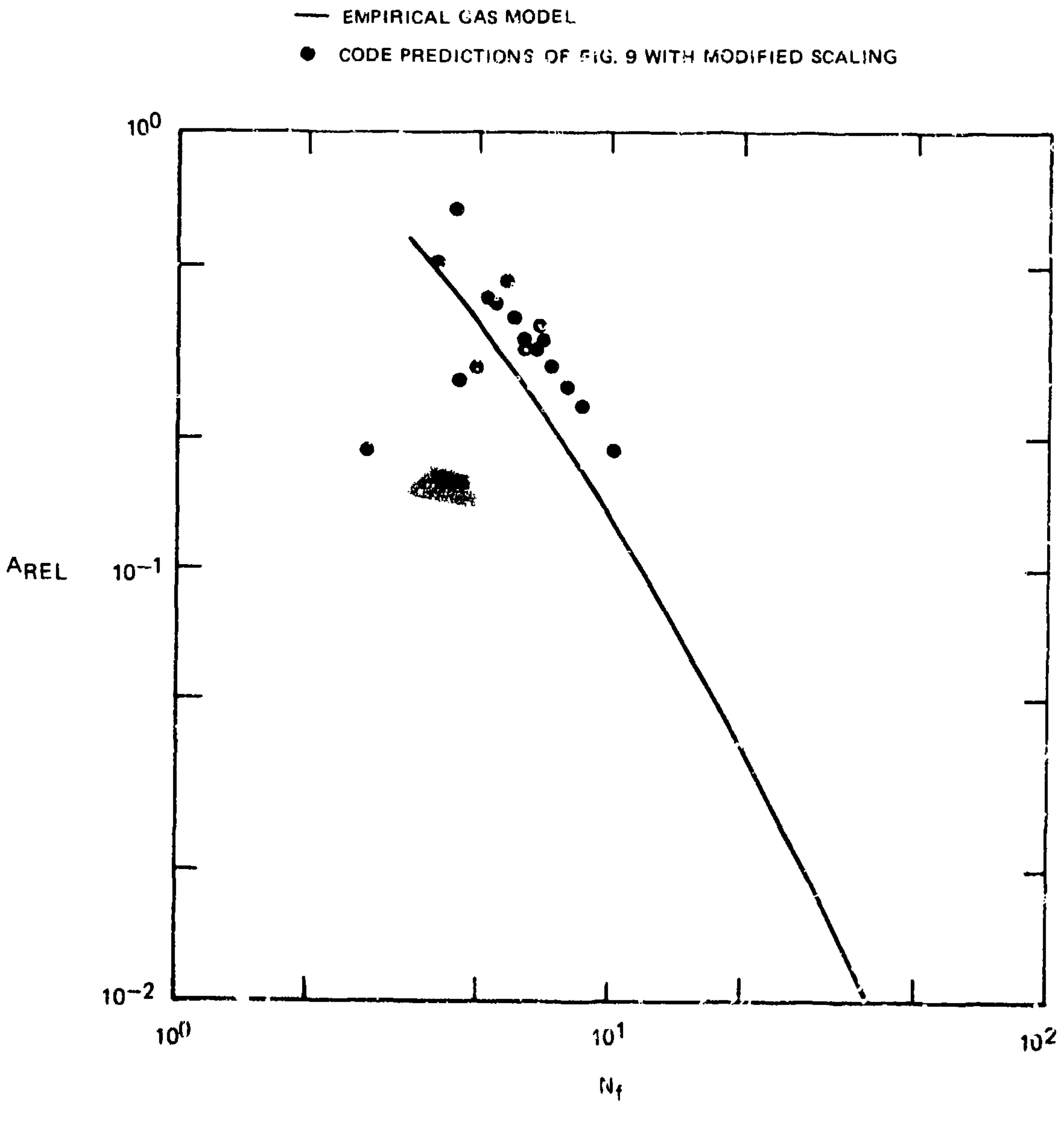

AEROSOL INDUCED THERMAL BLOOMING

EXPERIMENTAL ARRANGEMENT

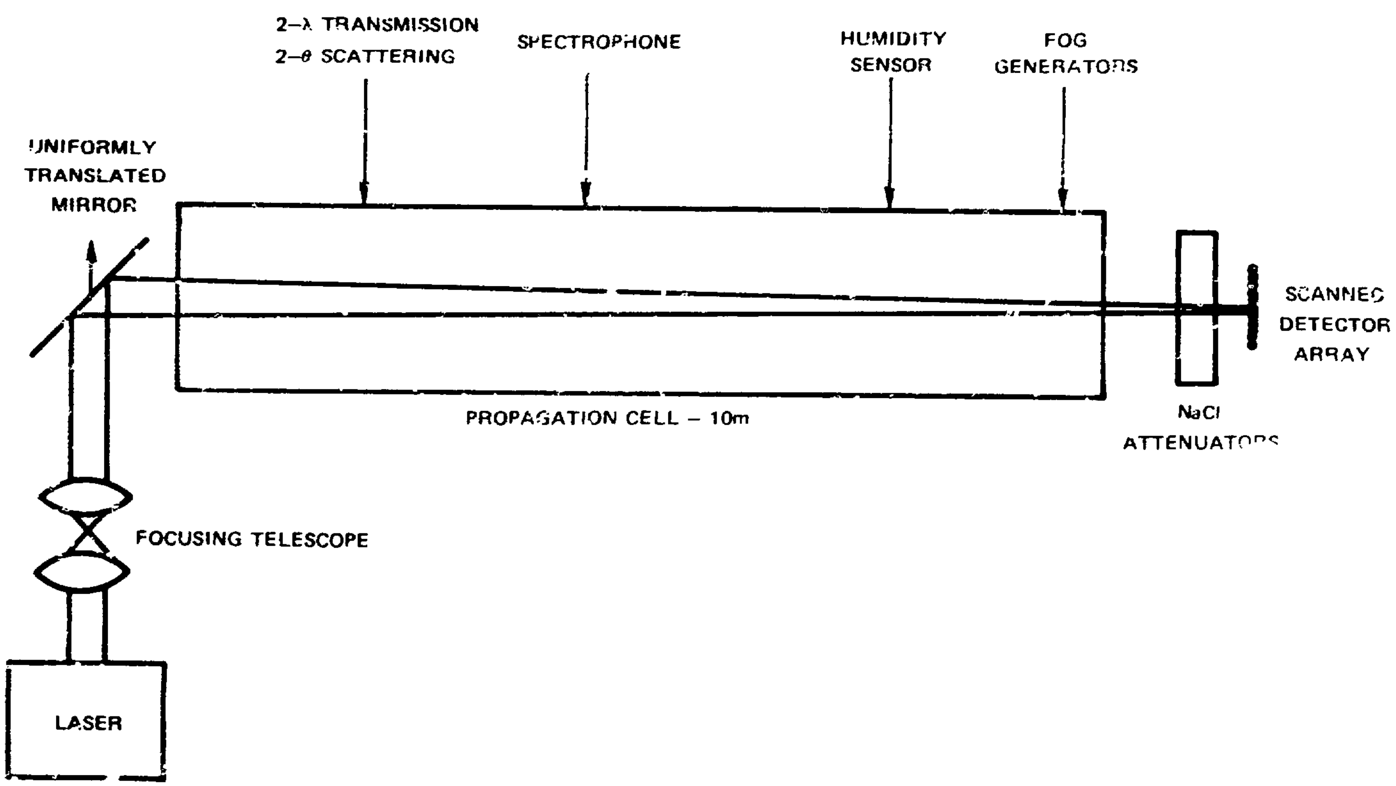

FIG. B–13

HIGH–POWER CROSS–BEAM AMPLIFIER

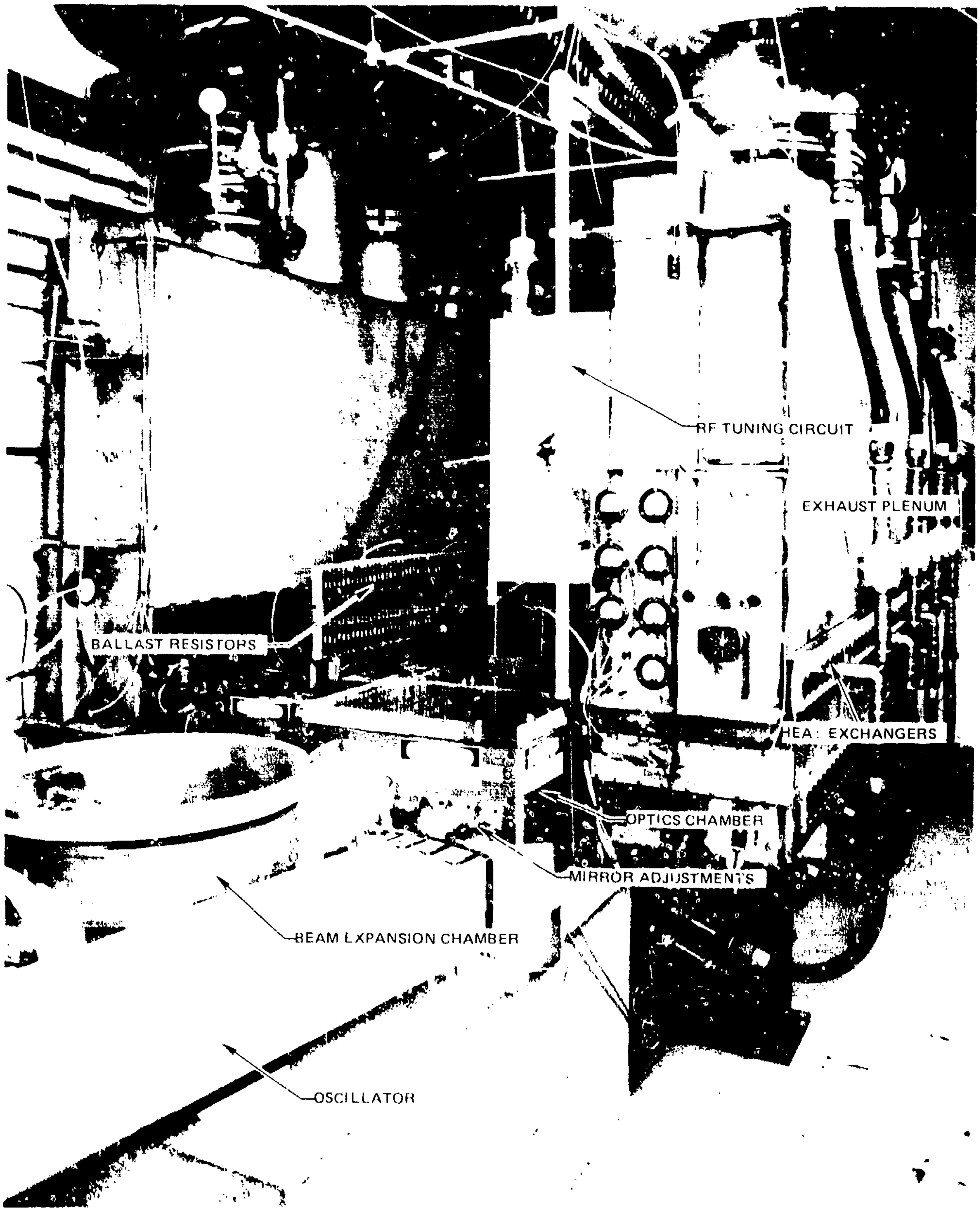

77-05-158-1

AEROSOL PROPAGATION CELL SCHEMATIC

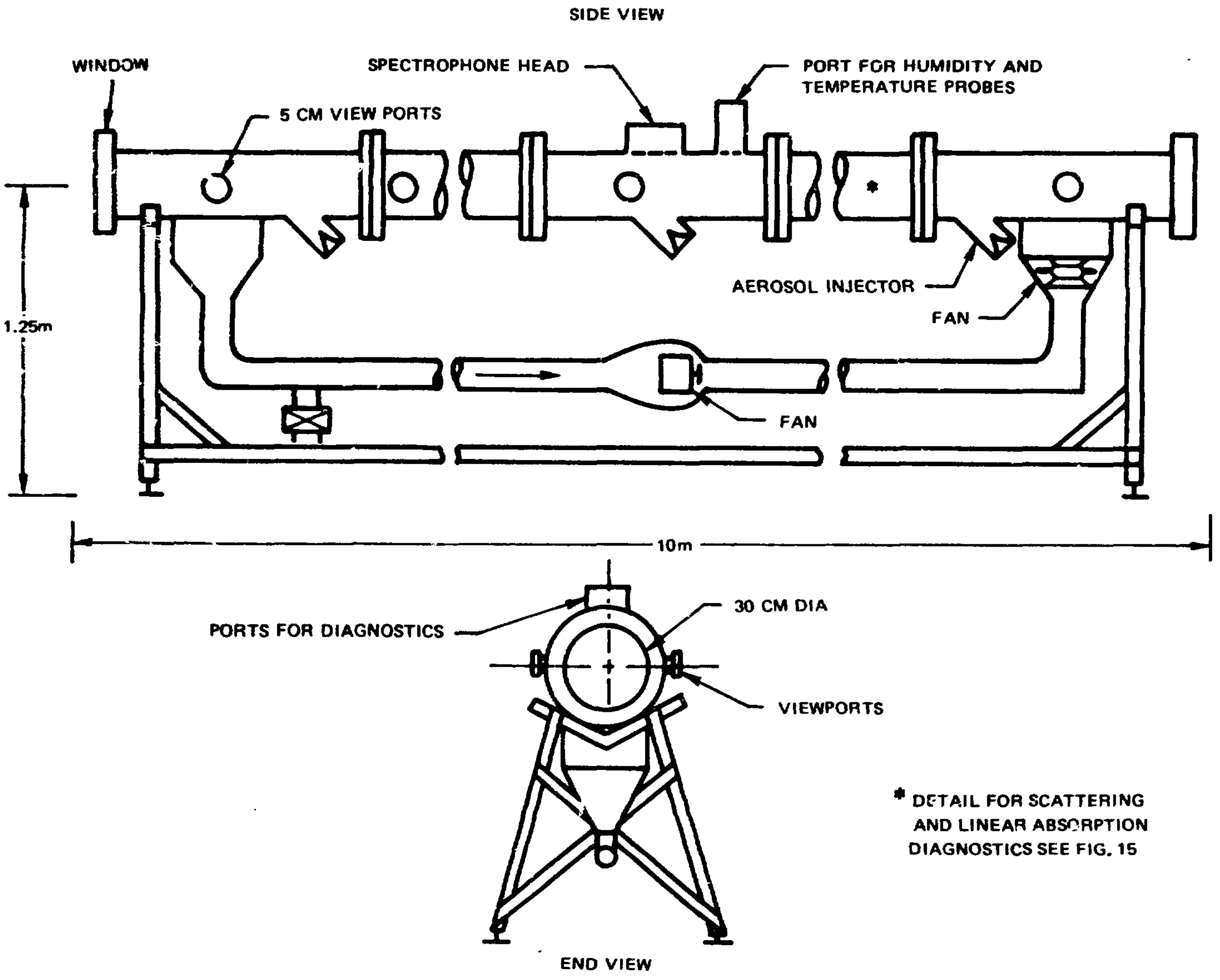

* DETAIL FOR SCATTERING AND LINEAR ABSORPTION DIAGNOSTICS SEE FIG. 15

FIG. B–14

77–06–27[illegible]–10

DIAGNOSTICS FOR AEROSOL CHARACTERIZATION

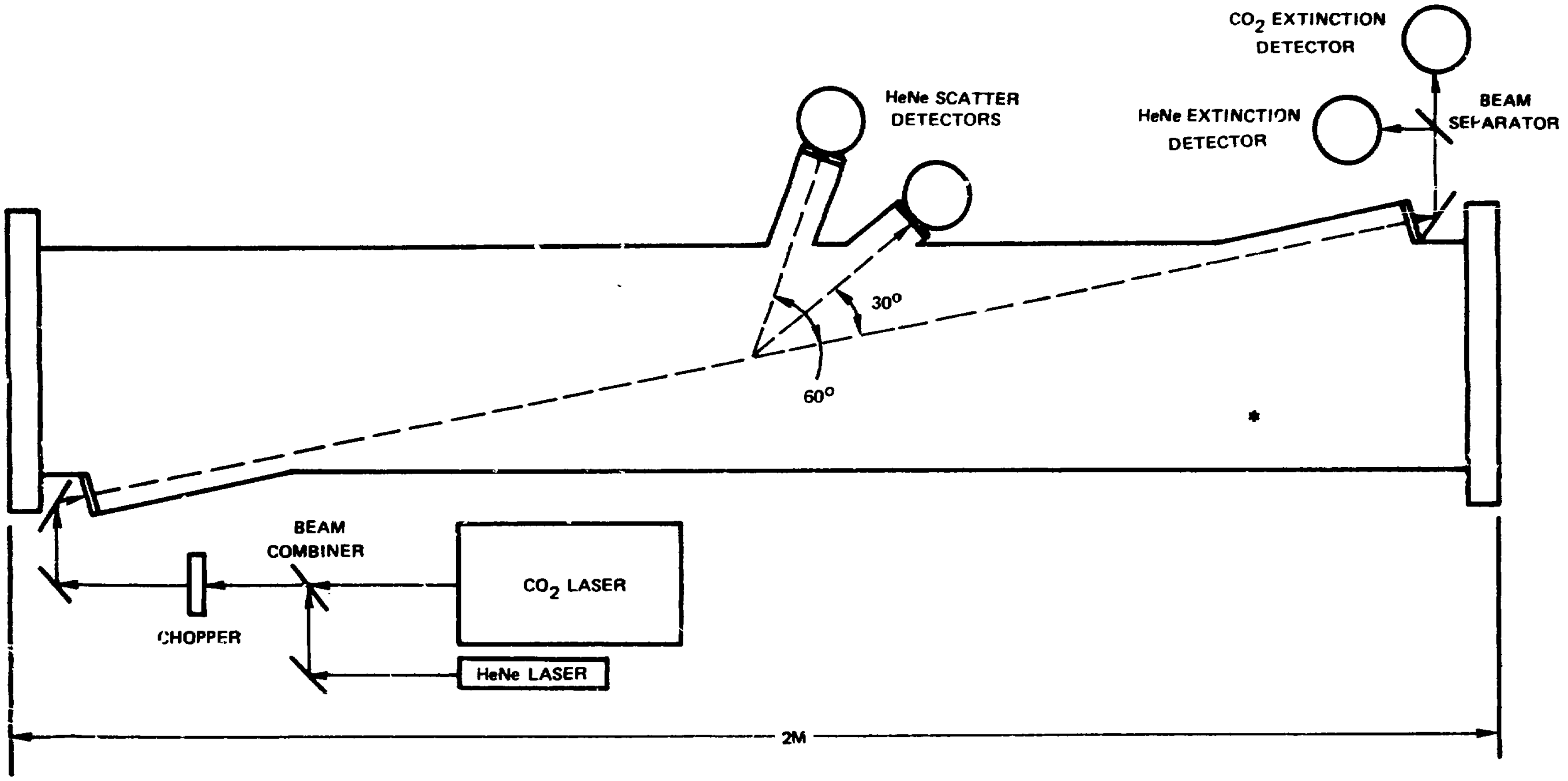

* ONE 2M SECTION OF AEROSOL PROPAGATION CELL IN FIG. 14

77-06-274-3

FIG. B-15

AEROSOL PROPAGATION CELL

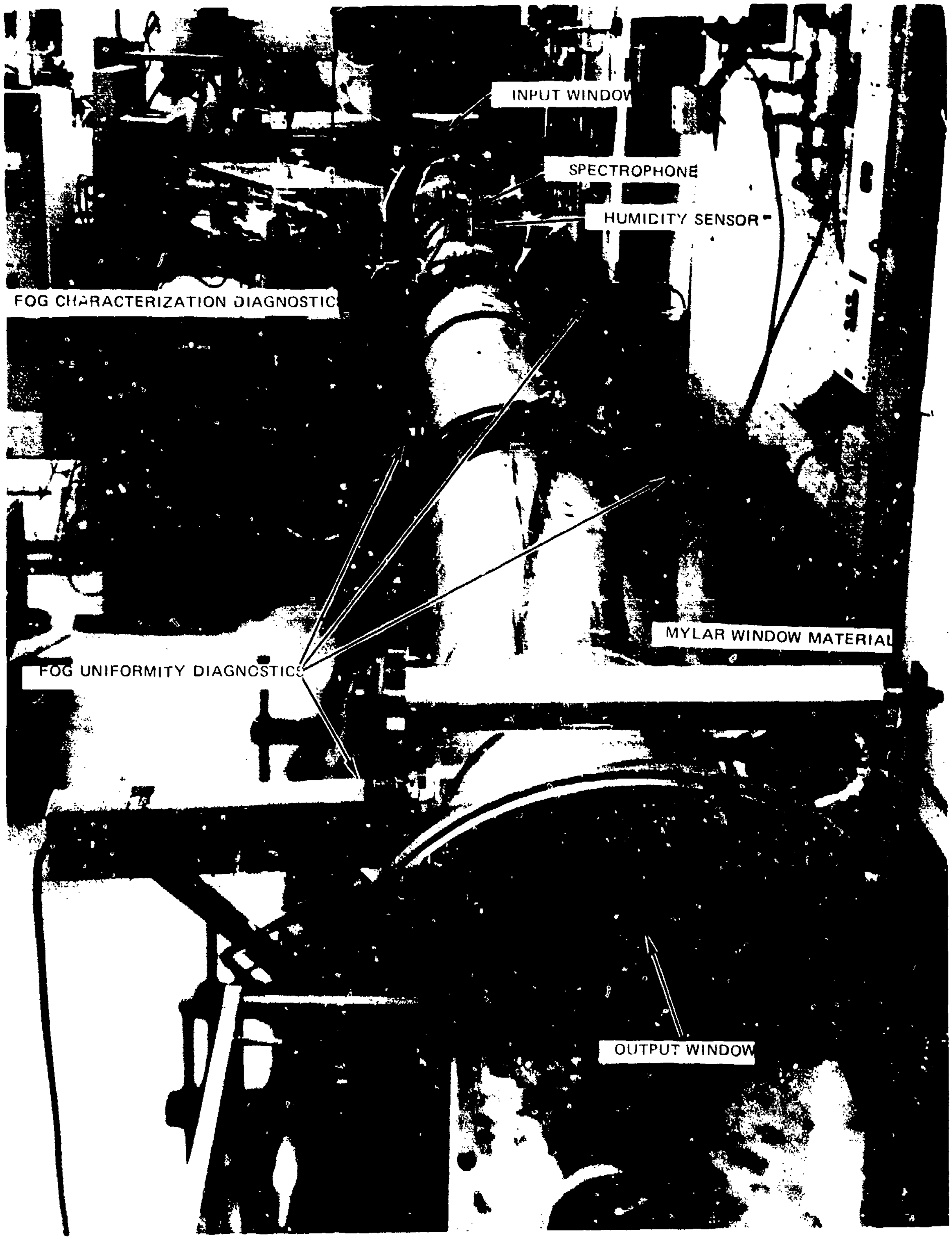

FIG. B-17

AEROSOL GENERATOR

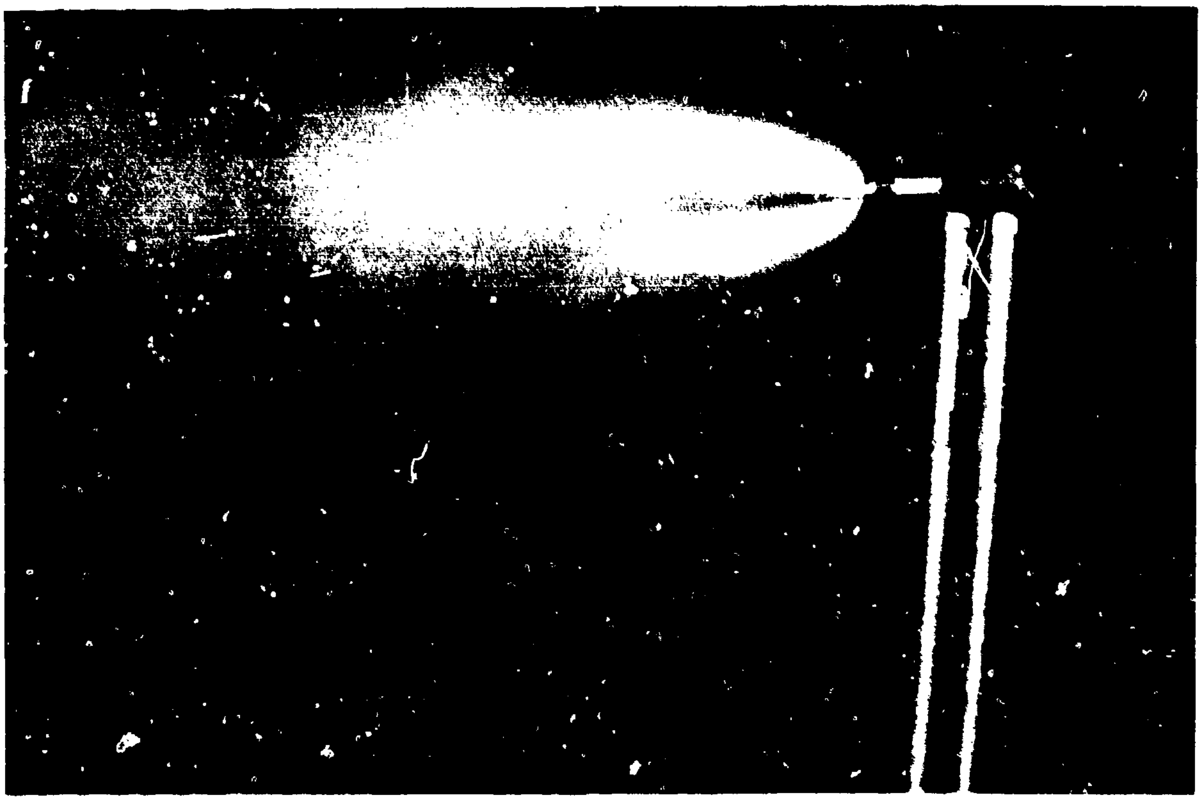

76-07-129-1

FIG. B–10

TWO WAVELENGTH EXTINCTION RATIO

H_2O DROPLET

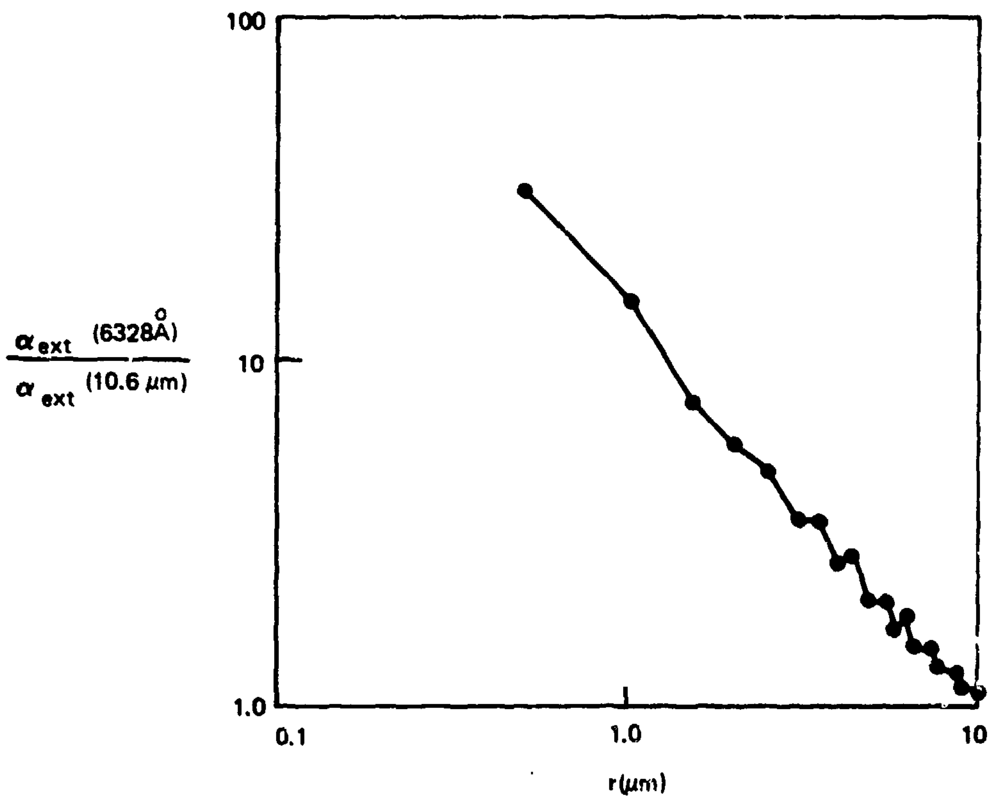

FIG. B-19

ANGULAR SCATTERING FUNCTION

$\lambda = 6328 \mathring{A}$

H_2O DROPLET

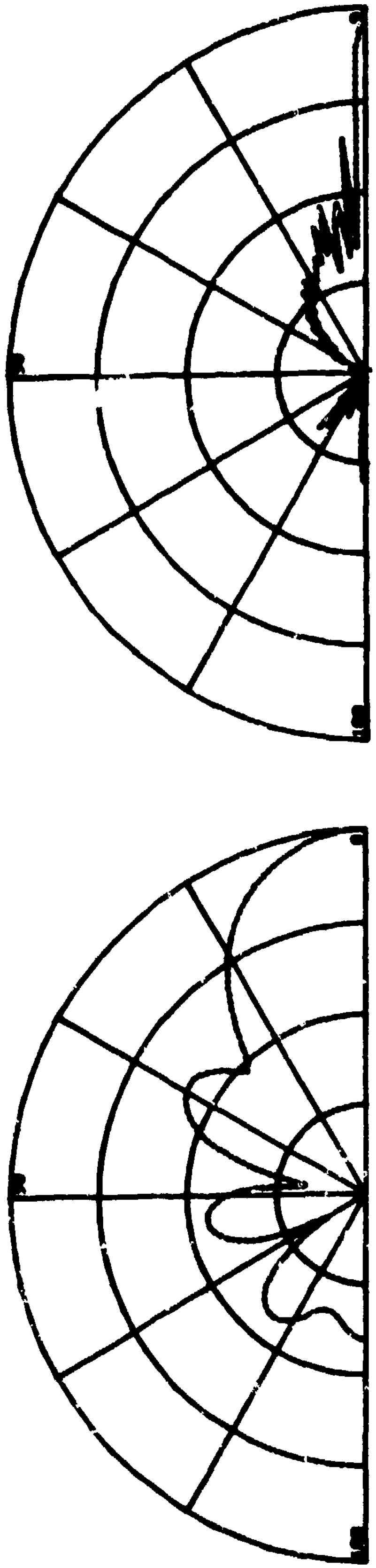

10 µm DIAMETER

1.0 µm DIAMETER

76-10-142-2

FIG. B-20

RATIO OF SCATTERING INTENSITIES

$\lambda = 6328 \AA$

H_2O DROPLET

MONODISPERSE

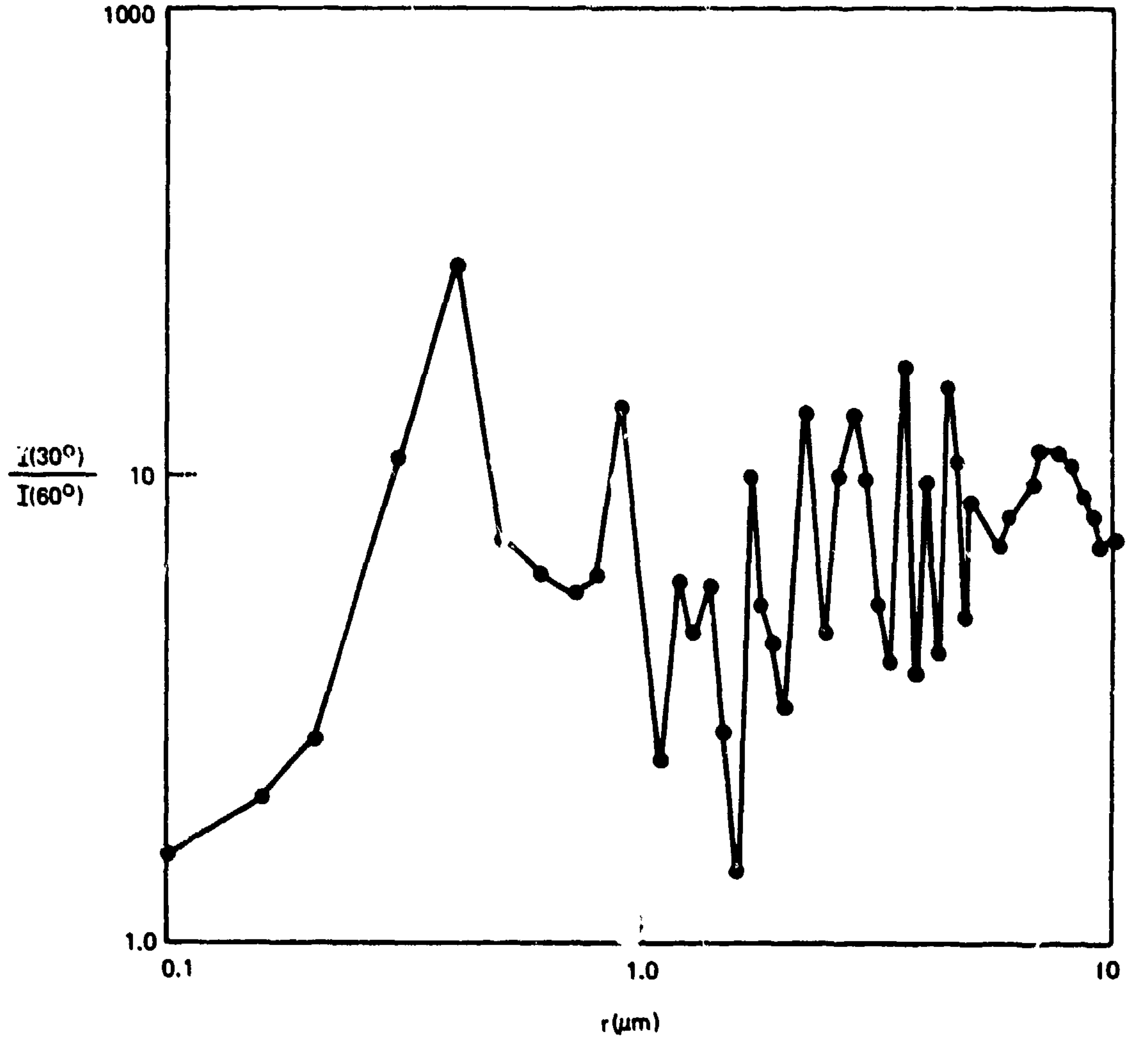

77-06-274-4

FIG. B–21

NORMALIZED DENSITY FUNCTION: ZOLD DISTRIBUTION

$r_m = 2.5$

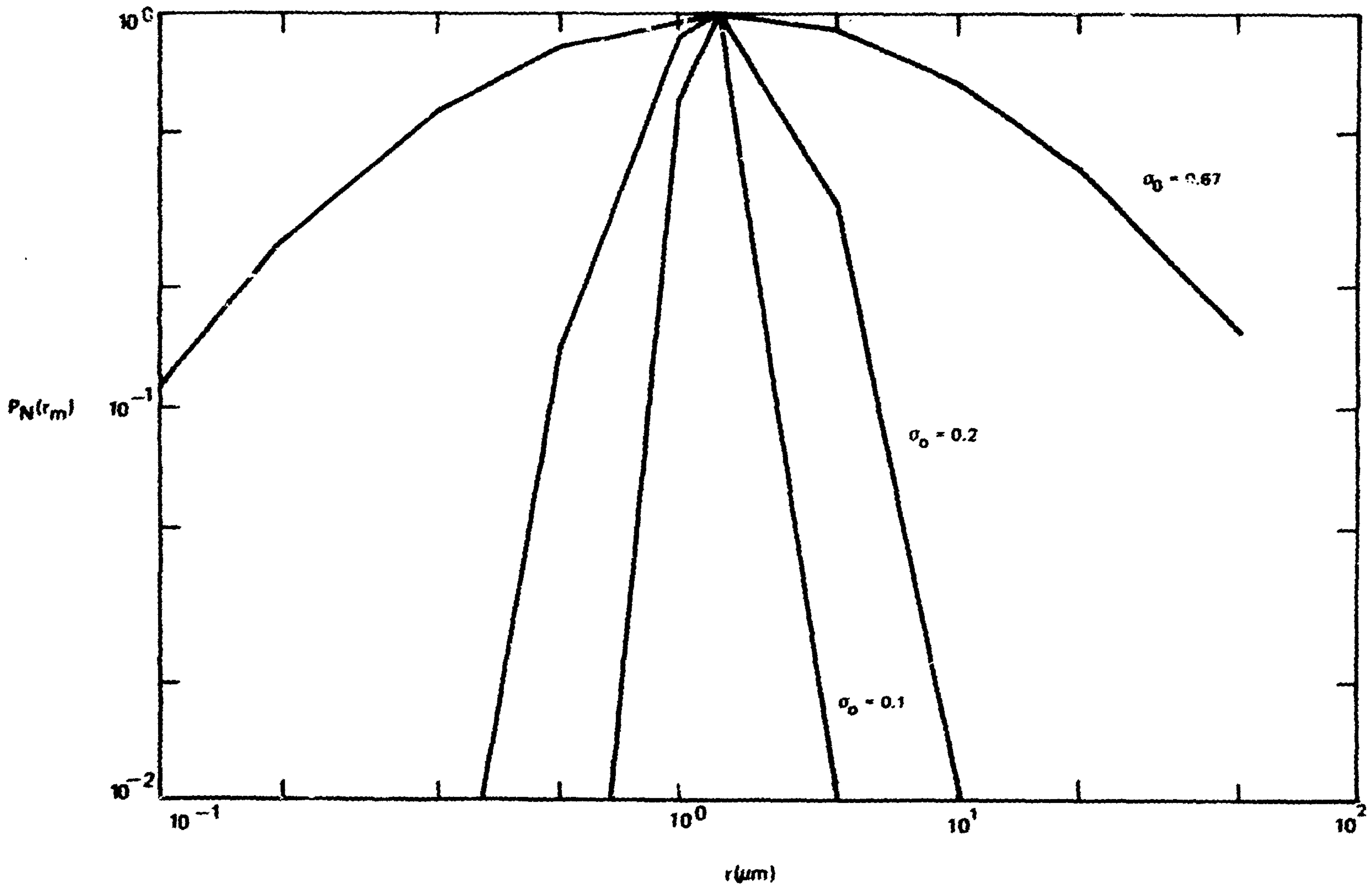

77–06–274–16

RATIO OF SCATTERING INTENSITIES

$\lambda = 6328\text{Å}$

H_2O DROPLET

ZOLD DISTRIBUTION

$\sigma_0 = 0.1$

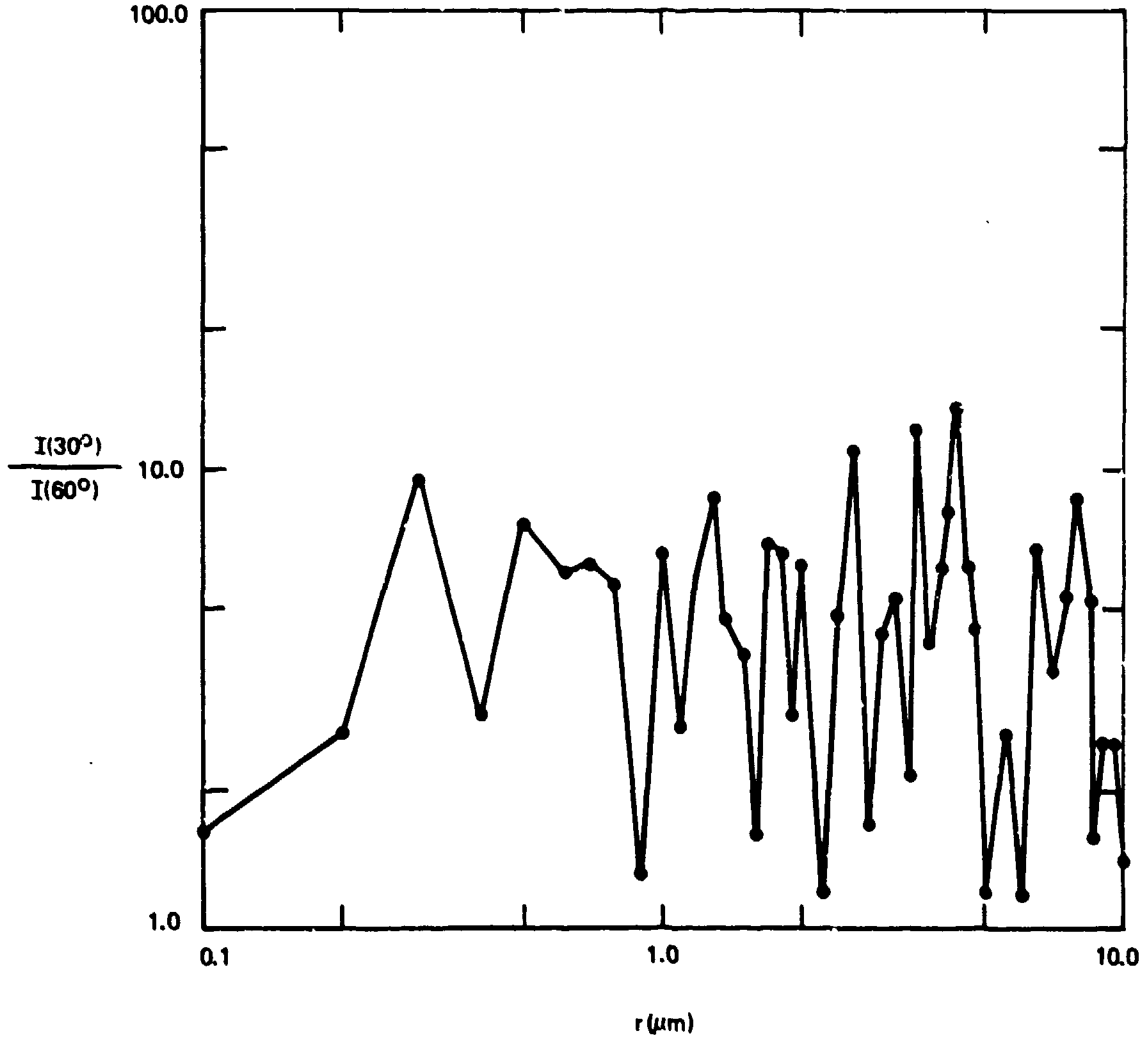

FIG. B–23

DIAGNOSTICS FOR FOG CHARACTERIZATION

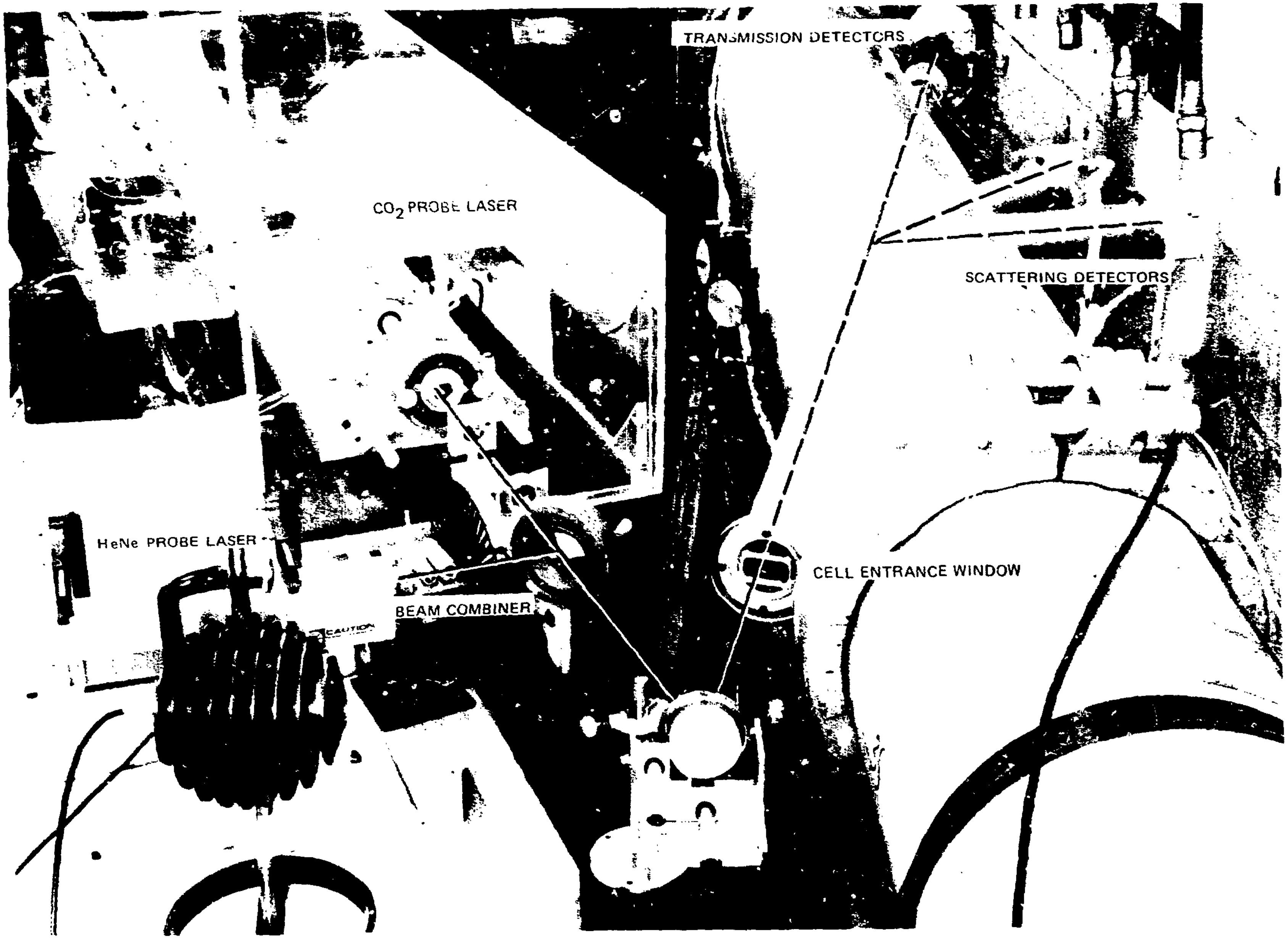

77–06–274–17

SPECTROPHONE ELECTRONICS

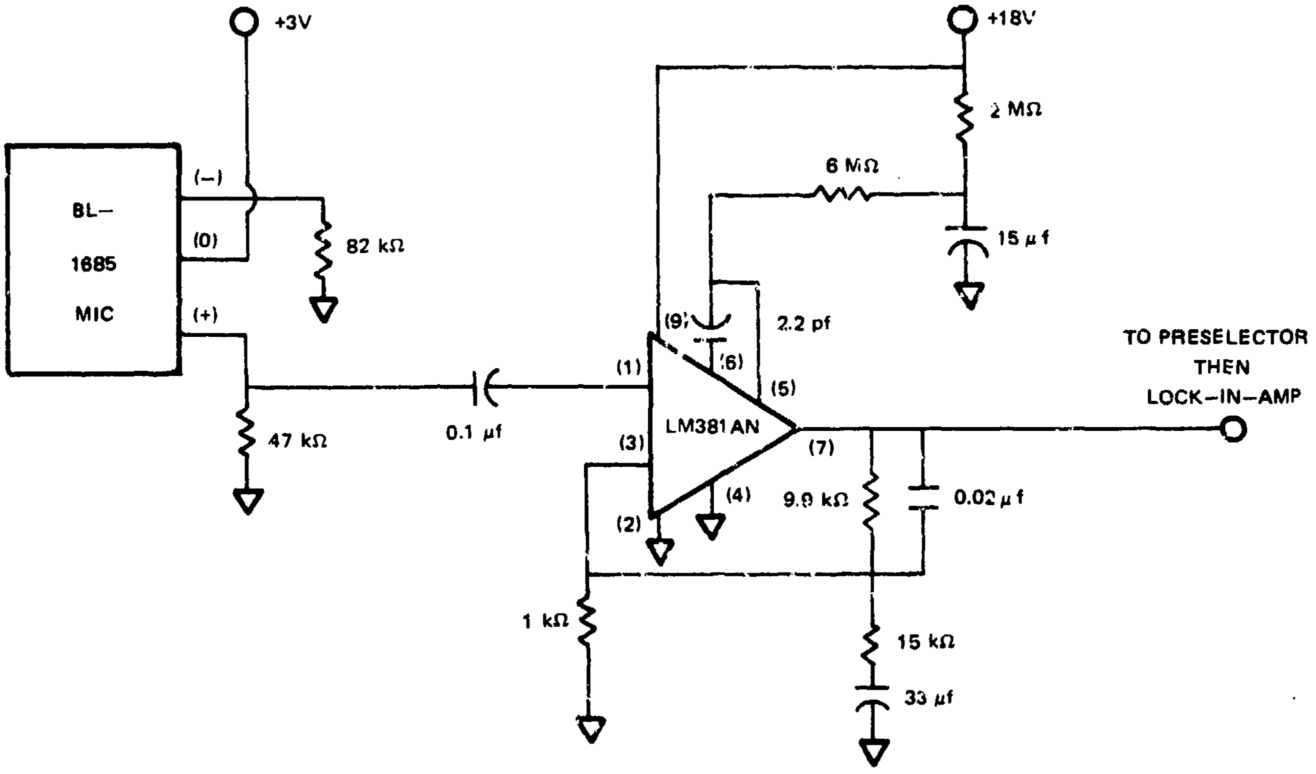

77–06–274–6

FOG INDUCED THERMAL DISTORTION

INTENSITY SCALE IS ARBITRARY

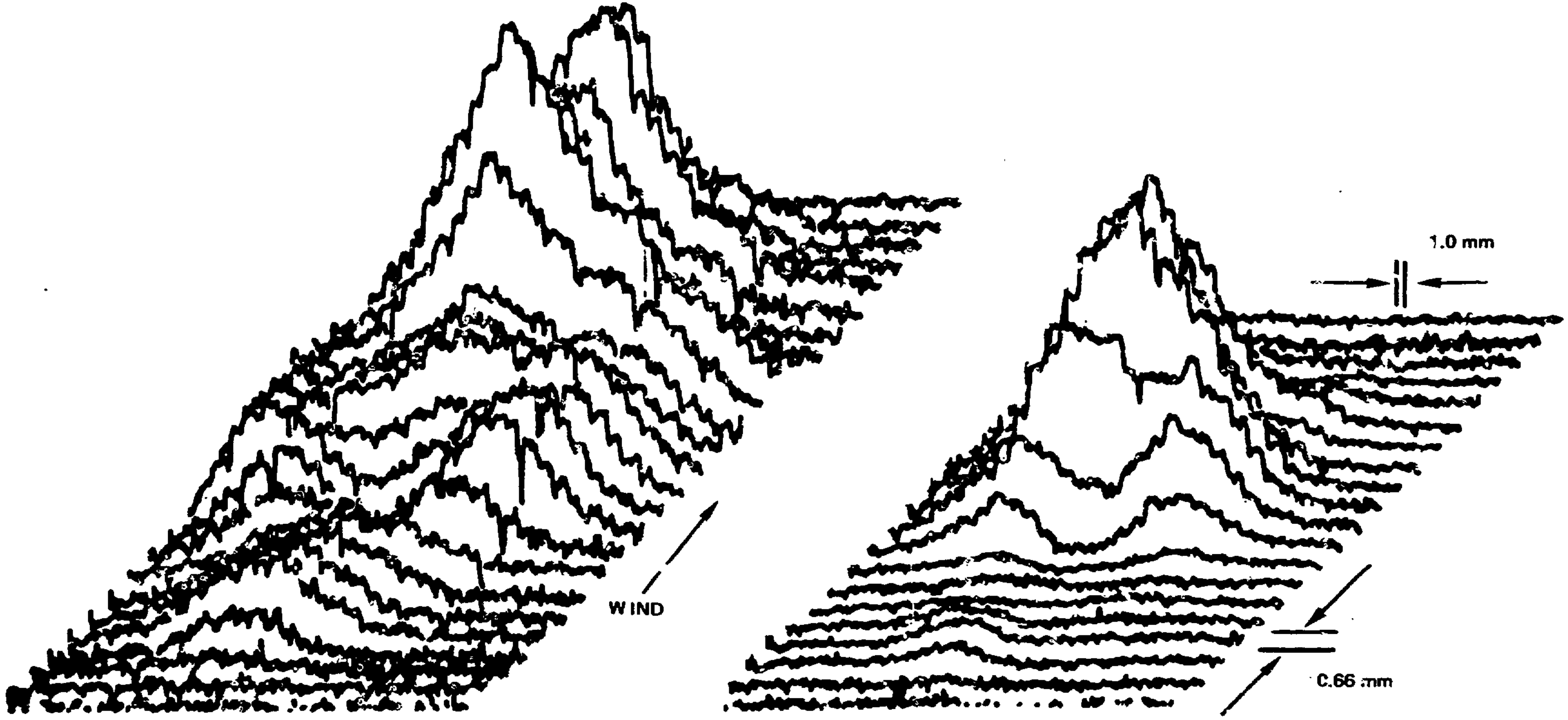

$P = 1.78$ kW
$\alpha_{abs} = 2.07$
$a = 1.45$ cm
$F = 4.19$
$v = 33$ cm/s

$P = 6.23$ kW
$\alpha_{abs} = 2.97$
$a = 1.45$ cm
$F = 4.19$
$v = 33$ cm/s

EXPERIMENTAL MEASUREMENTS

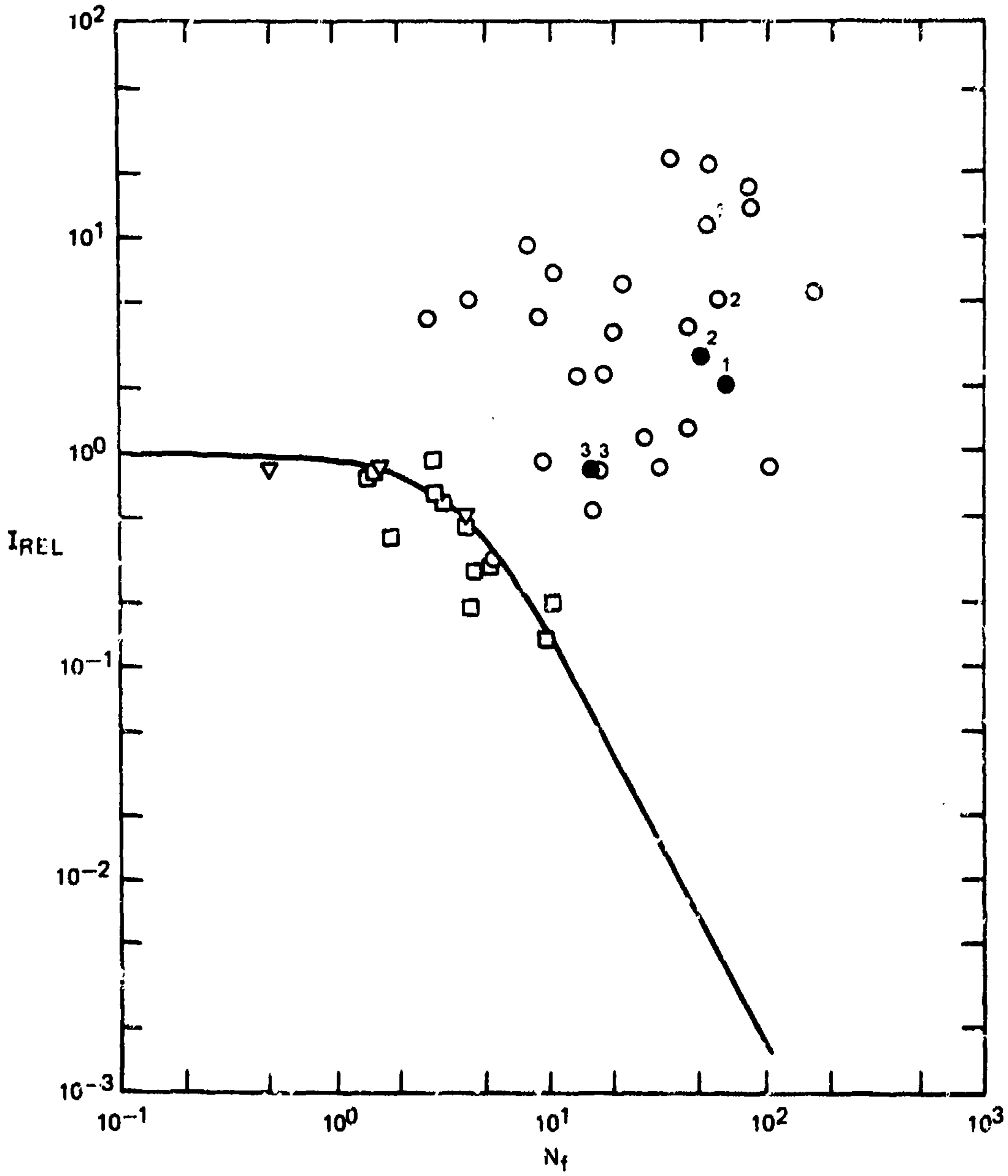

☐ GAS ABSORPTION BLOOMING

▽ SATURATED AIR BLOOMING

○ FOG ABSORPTION BLOOMING

— THEORY FOR GAS ABSORPTION

● THEORY FOR FOG (SATURABLE) ABSORPTION

FIG. B-27

MEASURED FOG INDUCED THERMAL DISTORTION

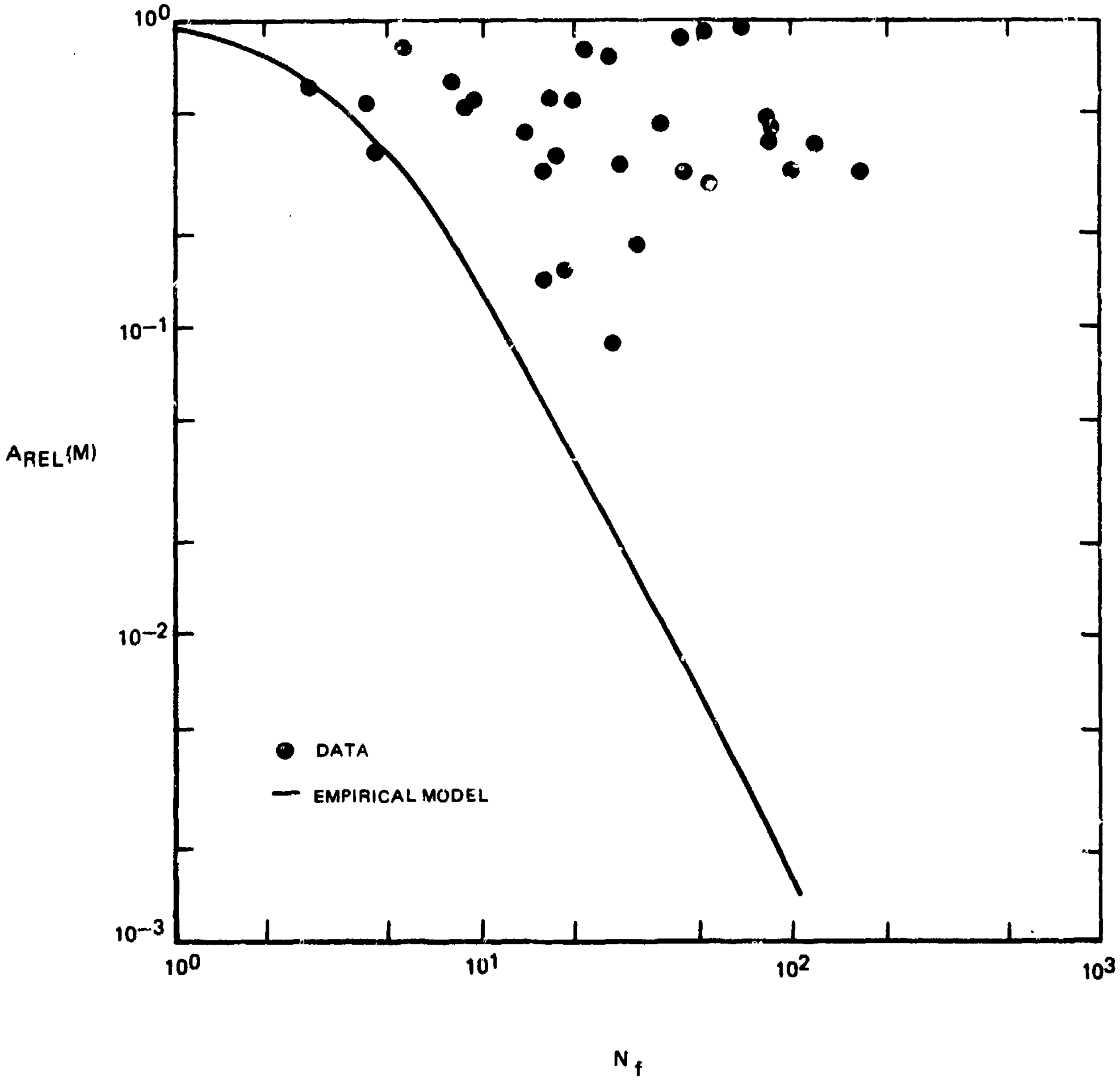

HIGH POWER BEAM TRANSMISSION THROUGH FOG

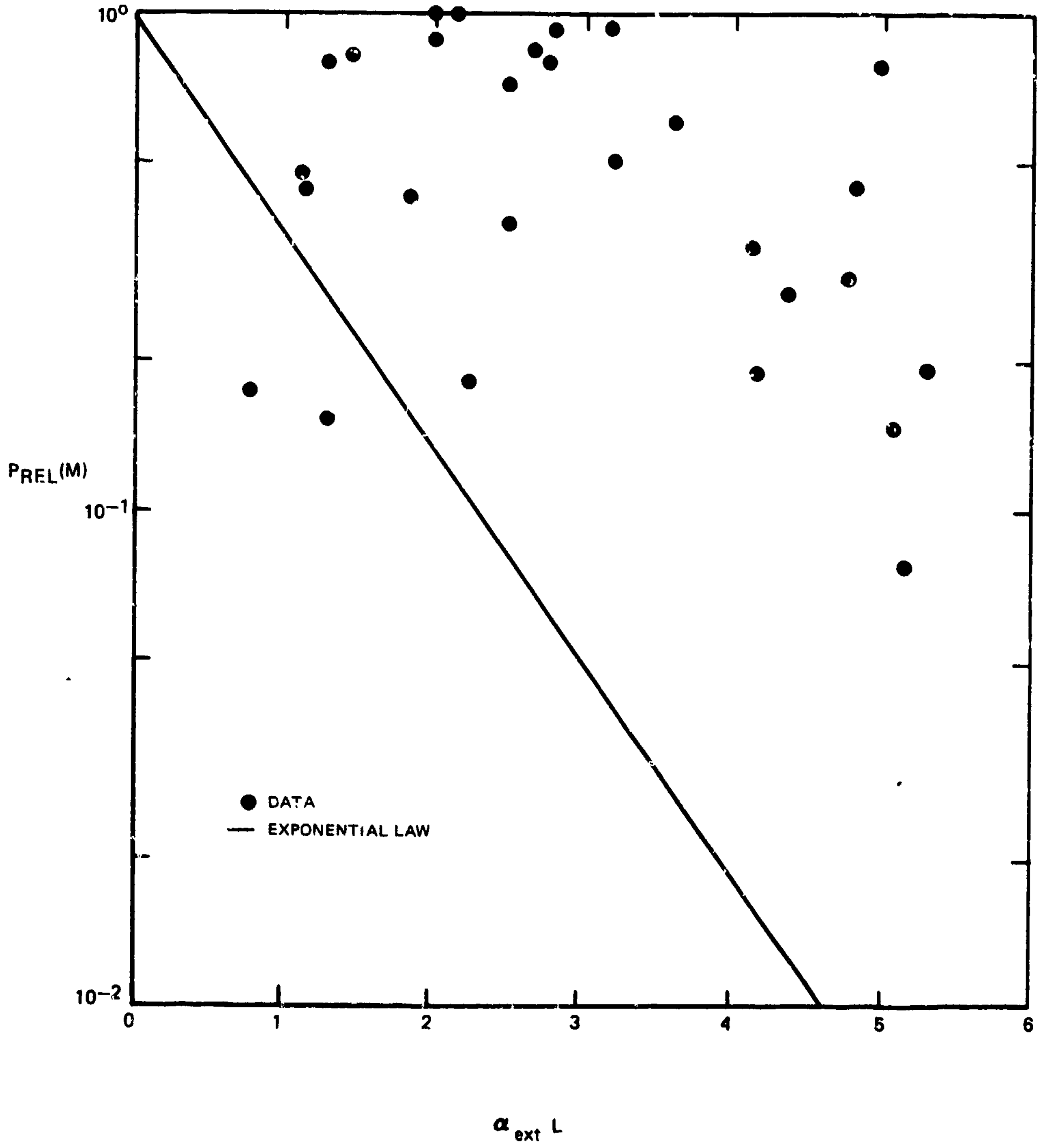

77-07-35-2

FOG INDUCED THERMAL DISTORTION WITH SPECTROPHONE CORRECTION

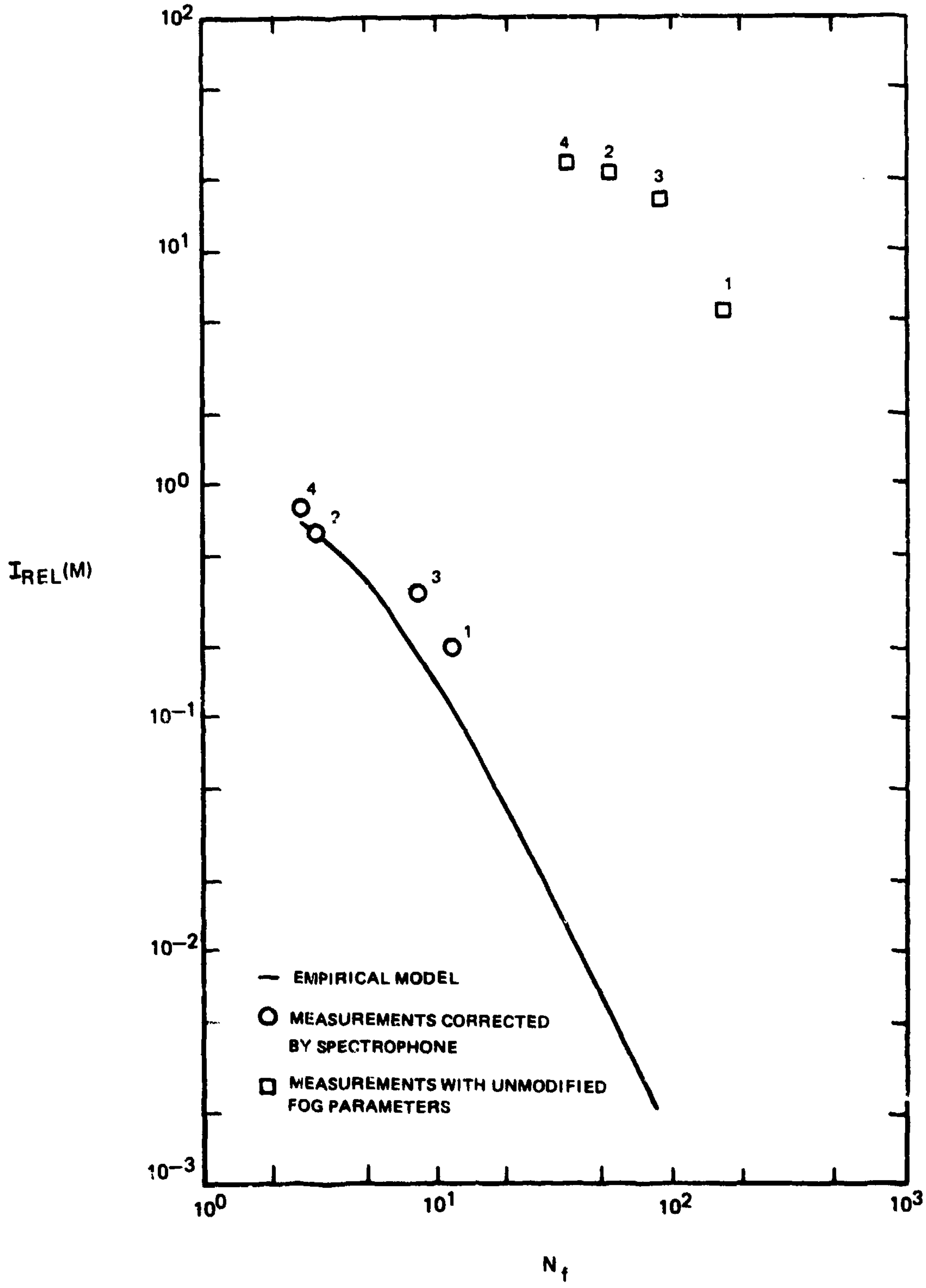

FOG INDUCED THERMAL DISTORTION MEASUREMENTS COMPARED WITH CODE

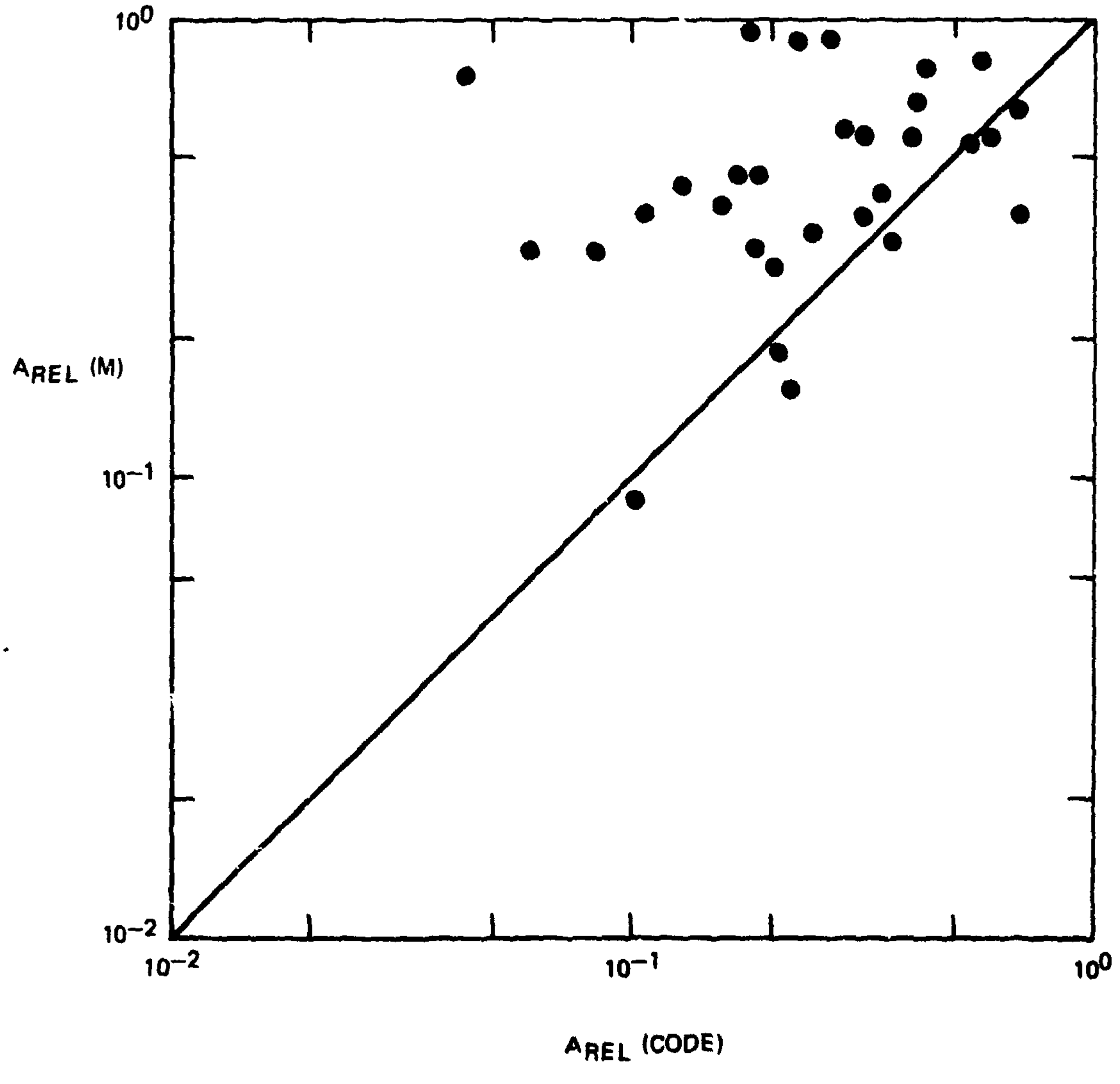

FIG. B-31

TRANSMISSION THROUGH FOG
MEASUREMENTS COMPARED WITH CODE

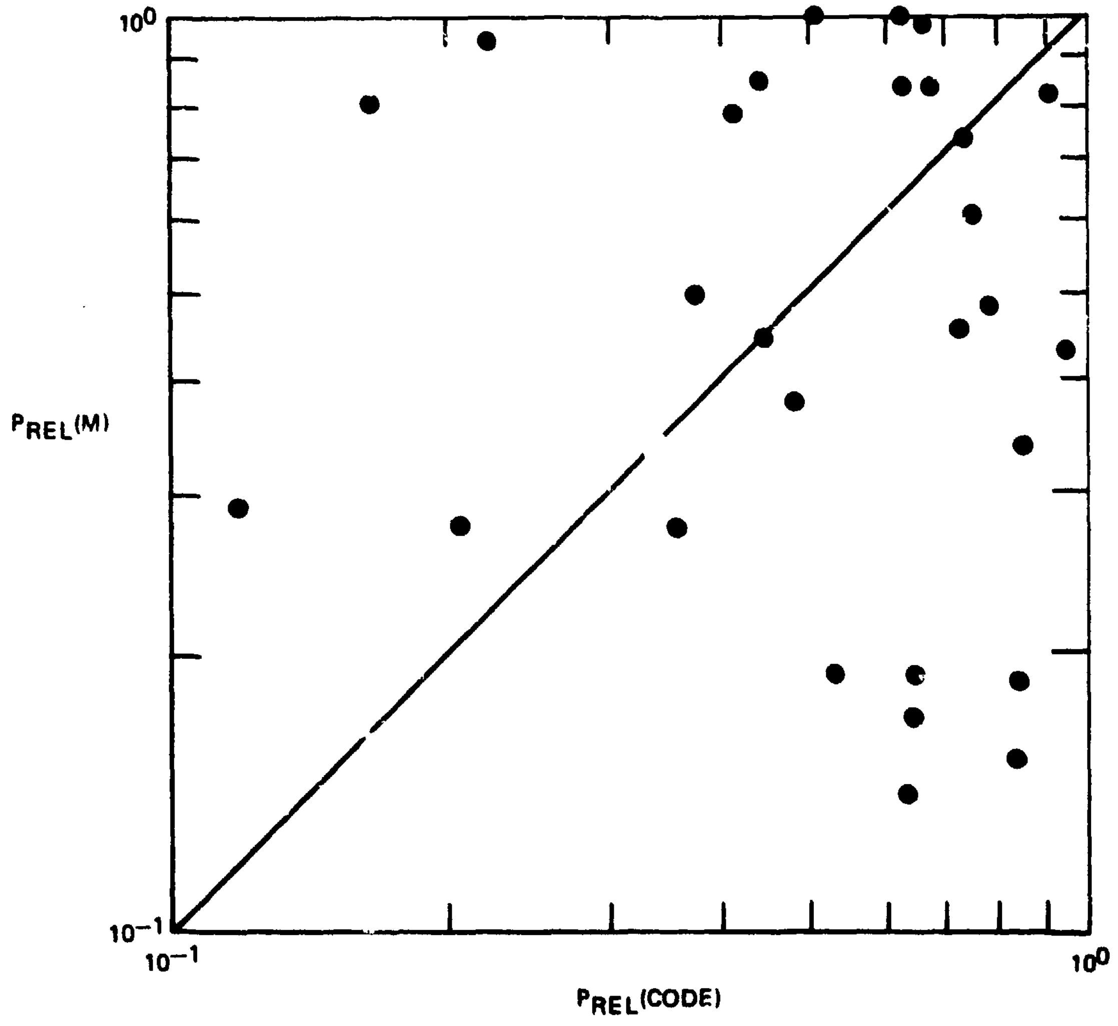

77-07-35-1